

ATOMIC LAYER DEPOSITION OF GaN AND TaN

By

OH HYUN KIM

A DISSERTATION PRESENTED TO THE GRADUATE SCHOOL
OF THE UNIVERSITY OF FLORIDA IN PARTIAL FULFILLMENT
OF THE REQUIREMENTS FOR THE DEGREE OF
DOCTOR OF PHILOSOPHY

UNIVERSITY OF FLORIDA

2009

© 2009 Oh Hyun Km

To my parents, Ukdong Kim and Kyungja Ko

ACKNOWLEDGMENTS

I thank the chair of my advisory committee, Dr. Timothy J. Anderson, for his support, education, and excellent guidance during my Ph.D. program in University of Florida. He taught me how to solve scientific and engineering black-box problem as a PhD. He also inspired me to utilize creative thinking when I faced dead-ends in my research. My advisory committee members, Dr. Lisa McElwee-White, Dr. Valentin Craciun, and Dr. Fan Ren gave me valuable advice on chemistry, material science, and device fabrication, respectively. My fellow Ph.D. student, Dojun Kim was an excellent collaborator and mentor. Our discussions helped my research in many ways. I also learned how to manage a research project from him. I appreciate the love from his family, which made me feel at home. I also thank my colleagues, Jürgen Koller, Jooyoung Lee, Vaibhav Chaudhari, David Wood, Christopher O'Donohue, and Joseph Revelli, for their help. My best friend, J. Patrick McKinney, gave me exceptional friendship as my second family. I am grateful to my fiancée, Hojung Kim. She supported me with love and care during my Ph.D. course. And, her solid trust in me allowed me to concentrate on my work. I am thankful to my two lovely sisters, Ansoon Kim and Sookheun Kim, for their care in many ways. Also, they were my role models, and excellent mentors. Last but the most, I would like to give my sincerest thanks to my parents, Ukdong Kim and Kyoungja Ko. Without them, I would not have had the chance to pursue the Ph.D. Their unconditional love and support is at the root of this accomplishment.

TABLE OF CONTENTS

	<u>page</u>
ACKNOWLEDGMENTS	4
LIST OF TABLES	8
LIST OF FIGURES	9
ABSTRACT.....	12
CHAPTER	
1 INTRODUCTION	14
1.1 Problem Statement for Atomic Layer Deposition of GaN.....	14
1.1.1 Challenges for Solid State Lighting	14
1.1.2 Hypothesis.....	15
1.2 Problem Statement for Atomic Layer Deposition of TaN	16
1.2.1 Diffusion Barrier for Cu Metallization	16
1.2.2 Limitation of PVD	17
1.2.3 Hypothesis.....	18
2 LITERATURE REVIEW	23
2.1 Development of GaN	23
2.2 Application of GaN in LED	25
2.3 Atomic Layer Deposition of GaN.....	27
2.4 Doping of GaN.....	29
2.4.1 <i>n</i> -type Doping of GaN	29
2.4.2 <i>p</i> -type Doping of GaN	30
2.5 Challenges in Interconnects	33
2.5.1 RC Delay in Interconnects	33
2.5.2 Electro-migration in Interconnects	34
2.5.3 Diffusion of Cu into Si.....	35
2.6 TaN as Diffusion Barrier	36
2.6.1 CVD of TaN.....	36
2.6.2 ALD of TaN.....	39
2.7 Cu Metallization.....	42
2.7.1 Processing of Cu Interconnect	42
2.7.2 Microstructure of Cu Thin Film for Various Deposition Methods.....	43
2.8 Barrier Failure Mechanism	44
3 EXPERIMENTAL SETUP	53
3.1 GaN ALD Reactor Design and Setup.....	53
3.2 Chemical Equilibrium Analysis for Growth Temperature.....	55

4	ATOMIC LAYER DEPOSITION OF GaN USING GaCl ₃ and NH ₃	61
4.1	Introduction.....	61
4.2	Experimental Procedures	63
4.3	Results and Discussion	64
4.3.1	Confirmation of Self-saturation ALD Growth.....	64
4.3.2	Process Temperature Window	65
4.3.3	Growth Characteristic of GaN ALD.....	66
4.3.4	Film Microstructure	68
4.3.5	Chemical Bonding State	69
4.4	Conclusions.....	70
5	COMPUTATIONAL STUDY FOR ATOMIC LAYER DEPOSITION OF GaN USING GaCl ₃ AND NH ₃	78
5.1	Introduction.....	78
5.2	Computational Details	79
5.3	Results and Discussion	80
5.3.1	Chemisorption of GaCl ₃	80
5.3.2	Chemisorption of NH ₃	82
5.4	Conclusions.....	83
6	<i>p</i> -TYPE DOPING OF GaN USING Cp ₂ Mg AS A DOPANT	88
6.1	Introduction.....	88
6.2	Experimental Details.....	89
6.3	Results and Discussion	90
6.3.1	Film Microstructure	90
6.3.2	Film Resistivity.....	90
6.3.3	Hole Properties.....	91
6.3.4	Optical Properties.....	92
6.4	Conclusions.....	94
7	EFFECT OF AIR EXPOSURE ON Cu DIFFUSION BARRIER PROPERTIES OF TaN THIN FILMS GROWN BY ATOMIC LAYER DEPOSITION.....	99
7.1	Introduction.....	99
7.2	Experimental Details.....	101
7.3	Results and Discussion	103
7.3.1	ALD of TaN Thin Films	103
7.3.1.1	Film Growth.....	103
7.3.1.2	Barrier Tests.....	104
7.3.2	<i>in-situ</i> (IN) Set vs. <i>ex-situ</i> (EX) Set	105
7.3.2.1	Microstructure of IN and EX Sets	105
7.3.2.2	Barrier Tests.....	105
7.4	Conclusions.....	108
8	FUTURE WORK AND SUGGESTIONS.....	116

8.1 Concerns of ALD-GaN for Device Application	116
8.2 ALD Doping of GaN	116
8.3 Device Fabrication of Nanorod-based LED	117
8.4 Control of TaO _x N _y for Better Diffusion Barrier Properties	118
LIST OF REFERENCES	120
BIOGRAPHICAL SKETCH	129

LIST OF TABLES

<u>Table</u>	<u>page</u>
2-1	Acceptor binding energies for C, Mg, Be, Zn and Cd in various III-V semiconductors. Taken from Ref [76]47
2-2	Microstructure of Cu films. Taken from Ref [112].47
3-1	Considered species in Ga-Cl system. Taken from Sub94 database.57
5-1	Standard enthalpy at 298 K (ΔH°_{298}) and Gibbs energy difference at 298K, 1 atm (ΔG°_{298}) and 923 K, 0.013 atm ($\Delta G^\circ_{923\text{ K}, 0.013\text{ atm}}$) for chemisorption of GaCl ₃85
5-2	Standard enthalpy at 298 K (ΔH°_{298}) and Gibbs energy difference at 298K, 1 atm (ΔG°_{298}) and 923 K, 0.013 atm ($\Delta G^\circ_{923\text{ K}, 0.013\text{ atm}}$) for chemisorption of NH ₃85
7-1	Barrier failure temperatures determined by different barrier testing methods for Cu/TaN/Si stacks of vacuum transferred and air exposed TaN.109

LIST OF FIGURES

<u>Figure</u>	<u>page</u>
1-1 Schematic of novel design LED using nanorod.....	21
1-2 Schematic of planar LED structure.....	21
1-3 SEM images of Cu/Si stacks with and without using TaN diffusion barrier (A) Cu/Si stack after annealing at 500 °C, 30 min under N ₂ , (B) Cu/TaN/Si stack after annealing at 500 °C, 30 min under N ₂	22
2-1 Experimental configuration of a typical m-i-n GaN LED. Taken from Ref. [46].	48
2-2 The structure of the high-brightness green-light-emitting diode with 20 Å thick In _{0.43} Ga _{0.57} N quantum well as active layer. Taken from Ref. [53].	48
2-3 Top view of a blue LED fabricated by Nichia without plastic capsule. Taken from Ref [7].	49
2-4 Effect of feature size scaling on total capacitance. Taken from Ref [80].	49
2-5 Damaged Al interconnect line showing the formation of hillock and void due to electro-migration. Taken from Ref [81].	50
2-6 Electro-migration lifetime for aluminum interconnects at different current densities. Taken from Ref [82].	50
2-7 Band diagram of Cu impurity in silicon. A) <i>p</i> -type Si, B) <i>n</i> -type Si. [77]	51
2-8 Hole-fill evolution for electroplated Cu with super-filling additives. Taken from Ref [100].	51
2-9 Evolution of hole-filling with different deposition conditions varying degrees of conformality. Taken from Ref [101].	52
3-1 Schematic of overall GaN ALD system.....	58
3-2 Schematic of GaN ALD reactor chamber.	58
3-3 Control program of GaN ALD process.....	59
3-4 (A) Equilibrium mole fractions of gas species in the Ga-Cl-Inert system as a function of temperature at P=1 atm. (B) Molar ratio of GaCl ₃ to Ga ₂ Cl ₆ in the Ga-Cl-Inert system as a function of temperature at P=1 atm.	60
4-1 Dependence of ALD GaN growth rate on GaCl ₃ exposure time. A) T _{growth} = 550 °C. B) T _{growth} = 650 °C. These films are grown on Si(100) with NH ₃ exposure time of 10 s.	72

4-2	Dependence of the growth rate on temperature. Exposure times were set as GaCl ₃ = 7 s, NH ₃ = 10 s, and N ₂ purge = 30 s.	73
4-3	Dependence of film thickness (XRR) on cycle number. Growth conditions were set as GaCl ₃ exposure time = 9 s, NH ₃ exposure time = 10 s, and N ₂ purge time = 30 s at T _{growth} = 650 °C. A) 5 cycles. B) 10 cycles. C) 15 cycles. D) 150 cycles.	73
4-4	Surface morphology of the GaN films deposited with 9 s of GaCl ₃ exposure time at 650 °C. A) 5 cycles. B) 10 cycles. C) 15 cycles. D) 150 cycles.	74
4-5	GIXD patterns for GaN films grown on Si(100) at 650 °C. A) ALD-GaN films. B) CVD-GaN films.	75
4-6	Surface morphology of the 60 nm-thick GaN films deposited at 650 °C under A) ALD growth condition B) CVD growth condition.	76
4-7	XPS spectra of GaN film grown by ALD at various GaCl ₃ exposure times. A) gallium 2p. B) nitrogen 1s. C) oxygen 1s. D) chlorine 2p.	77
5-1	Cluster model used in the calculation to represent GaN-GaNH ₂ * surface.	86
5-2	PES (ΔH°_{298}) and Gibbs energy surface at 298 K, 1atm (ΔG°_{298}) and 923 K, 0.013 atm ($\Delta G^{\circ}_{923\text{ K}, 0.013\text{ atm}}$) for the chemisorption of GaCl ₃ , representing first-half reaction. The unit is kcal/mol.	87
5-3	PES (ΔH°_{298}) and Gibbs energy surface at 298 K, 1atm (ΔG°_{298}) and 923 K, 0.013 atm ($\Delta G^{\circ}_{923\text{ K}, 0.013\text{ atm}}$) for the chemisorption of NH ₃ , representing second-half reaction. The unit is kcal/mol.	87
6-1	Crystallinity of Mg-doped GaN films as a function of Mg incorporation.	96
6-2	Resistivities of Mg-doped GaN films grown as a function of Mg incorporation.	96
6-3	Hole mobilities of Mg-doped GaN films as a function of Mg incorporation.	97
6-4	Hole concentrations of Mg-doped GaN films as a function of Mg incorporation.	97
6-5	PL spectra of Mg-doped GaN films as a function of Mg incorporation. A) undoped, B) Cp ₂ Mg: 5 sccm, C) Cp ₂ Mg: 10 sccm, D) Cp ₂ Mg: 15 sccm, E) Cp ₂ Mg: 20 sccm, and F) Cp ₂ Mg: 25 sccm.	98
7-1	A) Growth rate of ALD-TaN as a function of TBTDDET exposure time, which is deposited at 250 °C, and 10 s of purge and NH ₃ exposure time. B) Thickness of ALD-TaN films as a function of growth temperature deposited with 9 s of TBTDDET exposure time and 10 s of purge and NH ₃ exposure time. Taken from Ref [165].	110

7-2	A) XRD patterns of Cu/TaN/Si annealed at 500 °C for 30 min. B) Cross-sectional TEM image of Cu/TaN/Si structure. TaN was grown by ALD for 15 cycles at 9 s of TBTDET exposure time at 300 °C. Taken from Ref [165].	111
7-3	SEM images of Si surface after annealing Cu/TaN/Si at 500 °C for 30 min followed by the removal of Cu and TaN, and Secco etching for A) 10 cycles (16 Å) TaN film. B) 15 cycles (38 Å) TaN film. Taken from Ref [165].	112
7-4	Cross-sectional TEM image of as-grown Cu/TaN/Si structure of A) vacuum transferred TaN. B) air exposed TaN.	112
7-5	XRD patterns of annealed Cu/TaN/Si structure of A) vacuum transferred TaN. B) air exposed TaN at elevated annealing temperatures for 30 min.	113
7-6	Sheet resistances of the Cu/TaN/Si structures for vacuum transferred and air exposed TaN as a function of the annealing temperature.	114
7-7	SEM image of etch-pits observed on Si surface of Cu/TaN/Si for vacuum transferred TaN at annealing temperature of A) 585 °C, B) 600 °C, C) 615 °C, D) 630 °C, and E) 650 °C. Si surface of Cu/TaN/Si for air exposed TaN at annealing temperature of F) 585 °C, G) 600 °C, H) 615 °C, I) 630 °C, and J) 650 °C.	114
7-8	A) Barrier failure temperatures as a function of TaN barrier thickness. B) Plot of $\ln(L^2/T^2)$ vs $1/kT$ for Cu/TaN/Si stacks of vacuum transferred and air exposed TaN.	115

Abstract of Dissertation Presented to the Graduate School
of the University of Florida in Partial Fulfillment of the
Requirements for the Degree of Doctor of Philosophy

ATOMIC LAYER DEPOSITION OF GaN AND TaN

By

Oh Hyun Kim

December 2009

Chair: Timothy J. Anderson
Major: Chemical Engineering

Atomic Layer Deposition of GaN for LED applications and TaN for diffusion barrier applications in Cu metallization were demonstrated in this work.

GaN films were grown on Si(100) by ALD using GaCl₃ and NH₃ as the precursors. ALD process windows for self-saturation limit were identified. In this limit, both the (0002) and (10 $\bar{1}$ 1) orientations of GaN were evident, which was attributed to competition between vertical and lateral growth. Also, Cl incorporation was not detected in ALD-GaN grown within the ALD window.

To better understand the lack of detectable Cl incorporation in ALD-GaN, chemisorptions of GaCl₃ and NH₃ onto surface active sites were simulated using computational chemistry. Relatively high energy barrier for GaCl₃ adsorption decreased the extent of molecular trapping of a Cl complex on the growing surface. Furthermore, a low energy barrier for desorption of HCl facilitates cleavage of Cl from the growing surface.

The ability of growing *p*-type doped GaN is important for LED application. Mg-doped GaN films were grown on sapphire substrate by HVPE using GaCl₃, NH₃, and bis-cyclopentadienyl magnesium (Cp₂Mg). A systematic study of the growth temperature, Cp₂Mg

flow rate, and N/Ga ratio produced the highest hole concentration of $3.2 \times 10^{17} \text{ cm}^{-3}$. At this growth condition, the PL emission at 3.12 eV was obtained with 0.14 eV of FWHM.

TaN films were grown on Si(100) by ALD using *tert*-butylimido tris(dimethylamido) tantalum (TBTDET) and NH_3 . This material is commonly used as a barrier material in Cu metallization schemes. The effect of air exposure on TaN diffusion barriers prior to Cu deposition was studied by comparing Cu/TaN/Si stacks grown with and without air exposure as a function of annealing temperature. Interestingly, it was found that the barrier failure temperature of air exposed films is higher than those vacuum transferred. The TaO_xN_y interfacial layer appears to have a beneficial role in preventing Cu transport.

CHAPTER 1 INTRODUCTION

1.1 Problem Statement for Atomic Layer Deposition of GaN

1.1.1 Challenges for Solid State Lighting

Incandescent and fuel-based lamps typically convert the less than 5% of the input energy into the visible light. Fluorescent lamps have higher conversion efficiency, generally 20%. Solid state lighting, however, has the potential to surpass the luminous efficiency limitations of other forms of lighting, which leads to significant energy savings. It also presents many advantages over traditional light sources including longer life time, improved robustness, smaller size, and fast switching. There are, however, some issues in achieving higher efficiency.

A key issue limiting higher efficiency in solid state lighting is the lack of a suitable substrate. The most commercialized solid-state lighting is $\text{In}_x\text{Ga}_{1-x}\text{N}$ multi quantum well (MQW) structure. $\text{In}_x\text{Ga}_{1-x}\text{N}$ LEDs are currently deposited on the lattice-mismatched substrate, sapphire or SiC, which resulting threading dislocation densities in the range of 5×10^8 to 5×10^9 cm^{-2} . Cathodoluminescence studies show that threading dislocations in GaN film are non-radiative defects, thus limiting the conversion efficiency [1, 2]. Therefore, a more closely lattice-mismatched substrate is required to reduce threading dislocation density.

Another important issue in current solid-state lighting is the decrease in quantum efficiency with increasing device current. Auger recombination was reported to play a role in this phenomenon [3, 4]. Another report, however, associates the reduced efficiency with the escape of electrons from MQW region caused by polarization field. It is additionally explained by the decreased mobility of the heavy-mass hole in the MQW region [5, 6].

This review leads to the observation that the most important issues in advancing solid state lighting are identifying suitable substrate and increasing the quantum efficiency.

1.1.2 Hypothesis

The broad application of GaN-based LEDs for solid state lighting has been limited due to their high cost that in part is a result of their low efficiency. Cost can be lowered by increasing the integrated emission per area, which can be achieved by increasing the quantum efficiency and the active area. It is proposed to use nano-rod structure to significantly increase the active surface area relative to current planar structure. As shown in Fig. 1-1, the envisioned double-heterojunction (DH) LED structure is proposed using the array of nano-rods. InGaN active layer deposited on vertically aligned *n*-type GaN nano-rods needs to be followed by the growth of *p*-type GaN on InGaN active layer to complete the DH structure. In this structure, the emission will occur predominantly from the top side of each nano-rod through a transparent *p*-contact unlike the conventional planar structure in Fig. 1-2. This design has the potential to give much higher emission flux per unit substrate area, the value of which depends on the nano-rod aspect ratio (AR) and density.

There are, however, several challenges to realize this LED structure. First of all, the active layer needs to be deposited on high AR *n*-type GaN nano-rods at high density and uniformity, particularly along the wall of nano-rod. Deposition of smooth and uniform $\text{Ga}_x\text{In}_{1-x}\text{N}$ active layer on *n*-type GaN is essential to achieve high external quantum efficiency [7]. Secondly, it is necessary to control the *p*-type doping level of GaN. The doping level is known to be directly related to the performance of LED, especially output wavelength [8]. In this LED design, each nano-rod and the deposited layer are an emission unit and uniformity among the nano-rods must also be controlled.

Given the goal of demonstrating device structure, the present work is focused on developing a process for the deposition of GaN and $\text{Ga}_x\text{In}_{1-x}\text{N}$ on GaN nano-rod to achieve the required control. Atomic layer deposition (ALD) was used to deposit a conformal active layer

along the wall of nano-rod. ALD takes the advantage of the binding energy difference between chemisorption and physisorption, which can yield self-saturation surface adsorption. Unlike chemical vapor deposition (CVD) and physical vapor deposition (PVD), ALD is layer-by-layer deposition technique. This characteristic of ALD results in conformal films and precise thickness. Films grown by ALD are well known to yield precise control of thickness. In addition, the growth temperature can be decreased in ALD once surface reaction times are longer. Lower growth temperature decreases the N vacancy concentration, which is known to limit *p*-type doping level of GaN [8].

1.2 Problem Statement for Atomic Layer Deposition of TaN

1.2.1 Diffusion Barrier for Cu Metallization

Transport of Cu into Si and low- κ dielectrics lead to detrimental effects on device feature. To prevent diffusion of Cu into Si and dielectric films, a thin film is first deposited that acts as a diffusion barrier between Cu and the Si or dielectric material. There are several requirements to produce effective diffusion barriers for Cu metallization. The diffusion barrier must prevent the diffusion of Cu during independent device processing steps that can be at elevated temperature. Secondly, the diffusion barrier must show good adhesion to Cu, dielectric, and etch-stop layers. Good adhesion is essential to maintain device integrity during chemical mechanical polishing (CMP) processing, which is currently used with dual-damascene process. In addition, the diffusion barrier is required to have low electrical resistivity ($< 400 \mu\Omega\text{-cm}$) as well as good mechanical stability. Besides these material requirements, there are certain process constraints for deposition of the diffusion barrier film. Current minimum feature size dictate the growth of ultra-thin films with thickness in the range of few nano-meter. It is also necessary for the deposition process to achieve excellent conformality and step-coverage. Additionally, low deposition temperature is preferable to decrease the thermal budget.

Figure 1-3 shows the integrity of Cu and Si stack with and without using a TaN diffusion barrier. TaN was used as the diffusion barrier. As shown in Fig. 1-3B, significant Cu incorporated into Si without diffusion barrier in place. With using barrier, there is no inter-diffusion of Cu into Si (Fig. 1-3A). Currently, TaN/Ta bilayer is employed as diffusion barrier/adhesion promoter in the IC industry. TaN shows good diffusion barrier properties and good adhesion to SiO₂ but not to Cu. Ta, on other hand, shows good adhesion to Cu and TaN film. Ta also promotes the growth of Cu(111) during PVD-Cu seed layer deposition. It is well known that Cu(111) has higher electro-migration resistance as compared to other crystal orientations.

1.2.2 Limitation of PVD

Scaling of the diffusion barrier film is an important challenge given the shrinking dimensions of interconnects lines. Based on the International Technology Roadmap of Semiconductors (ITRS), the thickness of diffusion barrier needs to be scaled from 33 Å by 2010 to 19 Å by 2015 [9]. The scaling of barrier film is required with two reasons. First, the relative volume of the barrier film occupying the line or via increases as Cu line and via dimensions shrink, which results in the decreased available volume for Cu. This could increase both the *RC* delay and the current density in Cu lines and vias. Secondly, the thinner the barrier is, the lower is the overall electrical resistance between via and Cu line. To meet the constraints of future scaling, the ITRS calls for an improved deposition method.

PVD is currently employed to deposit diffusion barrier film in the industry. It is, however, believed for PVD to be incapable of depositing ultra-thin films with good conformality and step coverage. The PVD process is a line-of-sight process and the directional nature of the deposition process results in poor sidewall coverage inside the trenches and vias. To solve this sidewall coverage problem, ionized PVD (I-PVD) is introduced. I-PVD employs high density plasma to

ionize the metal ions during deposition. These ions are then perpendicularly directed to the wafer surface via magnets to obtain better sidewall coverage [10]. While I-PVD leads to improved sidewall coverage of diffusion barrier film, future generations of diffusion barrier films require deposition techniques that have a significantly better step coverage than I-PVD.

1.2.3 Hypothesis

Since PVD has a serious limitations in achieving conformal coverage on high aspect ratio contacts and via holes, chemical vapor deposition (CVD) has received recent attention as a deposition method for TaN. If the deposition is performed in the surface reaction limited regime and the temperature is controlled, the deposition rate should be uniform at all surfaces. There were two different approaches to CVD of TaN depending on the metal precursor. One approach is to use a Ta halides such as TaCl₅ or TaBr₅ [11, 12]. TaN-CVD using a halide source, however, requires a high deposition temperature to obtain low film resistivity and a high deposition temperature is not preferable for back end of line (BEOL) processing. In addition, Cl or Br incorporation in the diffusion barrier film is known to reduce the adhesion strength and enhance electro-migration [13, 14]. These are major concerns for long term device reliability. The other approach for TaN-CVD is using metalorganic (MO) Ta sources. The growth temperature can be significantly lowered by using MO sources compared to halide sources. Also, halide incorporation in the film is not an issue.

Although the ITRS road map calls for CVD of barriers, ALD will likely emerge as the dominant growth method for diffusion barrier deposition in the longer term. ALD shows superior conformality and accurate thickness control compared to other deposition methods. As the barrier thickness decreases, standard CVD will approach its usability limit due to difficulties in deposition rate and the thickness control. The highly conformal, ultra thin barriers by ALD

will be required to minimize the impact of barrier films on the resistance per unit length in Cu interconnects [15].

There have been reports on TaN-ALD using halide source (TaCl_5 , TaBr_5) and NH_3 [16, 17]. The deposited films were mostly polycrystalline Ta_3N_5 . Unfortunately, the grain boundaries in polycrystalline film are fast diffusion pathways for Cu. High resistivity ($> 10^4 \mu\Omega\text{-cm}$) in these films was also an issue. As an alternate approach, the MO source such as *penta*-kis(dimethylamido) tantalum (PDMAT) [18] and *tert*-butylimido-tris(diethylamido) tantalum (TBTDET) have been used as a precursor for TaN-ALD [19, 20]. A fcc NaCl-type nanocrystalline structure of TaN was obtained by using PDMAT as the Ta source [18]. Thermal ALD TaN films deposited with TBTDET showed the lower material density and higher resistivity than plasma-enhanced (PE) ALD TaN. Low resistivity of PE-ALD TaN was attributed to formation of a Ta-C bonds [17].

In this study, TaN thin films were grown with ALD for conformal and ultra-thin diffusion barrier films. TBTDET was used as a Ta source due to no halide incorporation. To meet the target barrier thickness in the ITRS road map, the effective minimum thickness of ALD-TaN barrier to block Cu diffusion was determined by annealing of various ultra-thin ALD-TaN films at 500°C , 30 min under N_2 . In addition to the thin film growth study of ALD-TaN using TBTDET, the effect of air exposure on the diffusion barrier quality was also investigated. Several factors including impurities, thickness, stress, and defects have been suggested to affect the barrier performance [21-24]. Generally, O, C, and H are the main impurities in ultra thin films deposited by ALD because they are prepared from using MO precursors. These impurities are known to change the structure and properties of TaN thin films [17, 25, 26]. There is a report of oxygen positively influencing the performance of TiN, presumably by oxygen stuffing in

diffusion pathway [27]. To understand the effect of air exposure on the diffusion barrier property, specifically thermal stability, Cu/TaN/Si stacks were prepared with and without exposure to air after deposition of the TaN/Si. Both of stacks were annealed at the same temperature, and compared in different categories of thermal stability test.

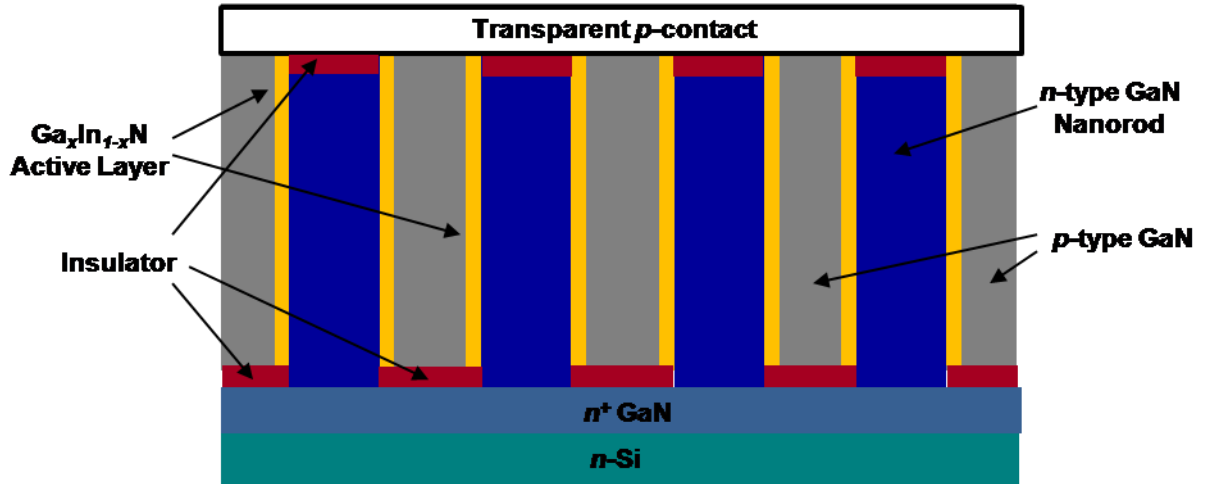


Figure 1-1. Schematic of novel design LED using nanorod.

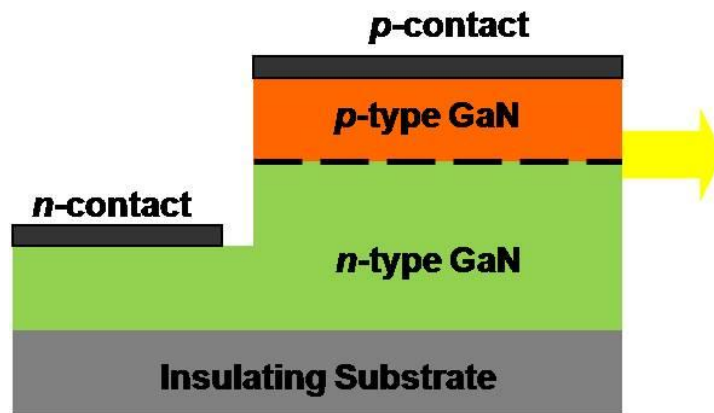


Figure 1-2. Schematic of planar LED structure.

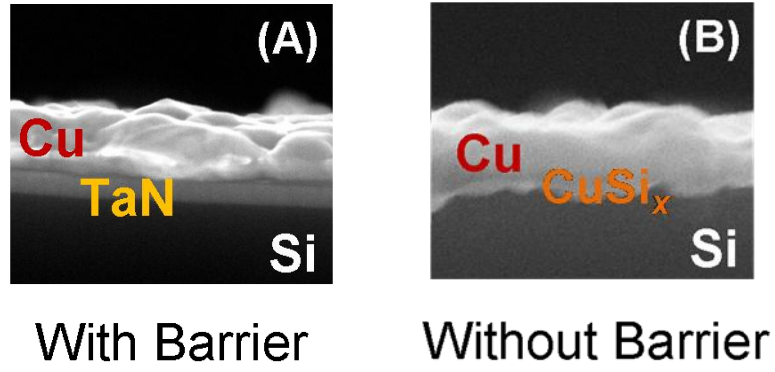


Figure 1-3. SEM images of Cu/Si stacks with and without using TaN diffusion barrier (A) Cu/Si stack after annealing at 500 °C, 30 min under N_2 , (B) Cu/TaN/Si stack after annealing at 500 °C, 30 min under N_2 .

CHAPTER 2 LITERATURE REVIEW

2.1 Development of GaN

GaN was first synthesized in 1928 and it was proclaimed that “Gallic nitride is an exceedingly stable compound” [28]. GaN has been an attractive material for high temperature operating device by its chemical stability at elevated temperatures combined with its wide band gap. GaN crystals were first grown in 1938 by flowing NH_3 through gallium at high temperatures [29]. The photoluminescence of GaN grown by the same method was measured for the first time in 1959 [30]. The first GaN film was deposited on sapphire substrate by CVD in 1969 [31].

Due to its large background n -type carrier concentration, the lack of suitable substrate, and difficulty of p -type doping, however, little attention was paid to GaN for use as a semiconductor. GaN regained interest largely due to its potential as a blue light emitter. Previous reports claimed to obtain high quality GaN with room temperature background carrier concentration as low as $n \sim 4 \times 10^{16} \text{ cm}^{-3}$. Improvement in the structural quality of GaN was reported in 1983 by using low temperature (LT) grown AlN buffer layer [32]. Others reported improved surface morphology as well as electrical and optical properties of GaN using LT-AlN buffer layer in 1986 [33]. To fabricate GaN based devices, electronic properties such as carrier concentration and mobility must be controlled. The doping of wide band gap materials is known to be difficult in part due to the high probability of forming native defects. Intrinsic GaN grows unintentionally in n -type with a direct wide (3.4 eV) bandgap. The long held belief is that the native n -type nature of GaN is due to the formation of N-vacancies which exhibit donor behavior.

High conductivity p -type GaN was not achieved until 1989. It was observed that p -type conductivity drastically improved after low energy electron beam irradiation (LEEBI). The first

UV-LED was fabricated by utilizing LEEBI treated Mg doped *p*-type GaN and intrinsic *n*-type GaN in 1989 [34]. Nakamura later established that a simple annealing in an inert or vacuum environment will improve *p*-type conductivity similar to the LEEBI treatment [35]. The reason for the improvement in *p*-type conductivity caused by LEEBI or annealing was not clear then, but it was later discovered that an Mg-H neutral species prevents Mg activation [36]. GaN-based Field Effect Transistors (FET) and Heterojunction Bipolar Transistors (HBT) were also fabricated in the early 1990s, enabled by improvements in crystal quality and conductivity [37]. The threading dislocation density of these transistors, however, was about 10^9 to 10^{10} cm⁻², or about 10⁶ times higher than typical semiconductors. Although devices could be fabricated with the high density of dislocations, their long-term reliability was questioned. In 1994, a significant reduction of the dislocation density was achieved by adopting lateral epitaxial overgrowth that used either a SiO₂ or Si₃N₄ mask [38]. Because threading dislocations tend to form parallel to the growth axis, vertical blocking of the threading dislocations improved crystal quality drastically (from 10^9 - 10^{10} to 10^4 - 10^5 cm⁻²). GaN-based devices began to be fabricated more routinely beginning in 1994. It is worth mentioning that Nakamura's two-flow reactor design significantly improved crystal quality [39]. In this process, inert or hydrogen gas is injected vertically onto the substrate to modulate local concentrations of precursors by reducing the boundary layer thickness. Following these improvements, Nakamura reported an InGaN based 1 cd LED in 1994, a 10 cd LED in 1995, a laser diode in 1996, and continuous wave (CW) lasing at room temperature in 1997 [39-43]. Nichia Corporation reported an estimated 10,000 hr lifetime of blue laser diodes in 1998 [44]. Research related to GaN has continued as a result of the major breakthroughs made during the 80s and 90s. The lack of a suitable substrate material continues to create problems and the growth of large (> 2") diameter freestanding GaN has not been easily

achieved due to cracking and bowing problems. Also, the heat generated from LED devices due to the low thermal conductivity of the sapphire substrate is still problematic. Undoubtedly, the integration of GaN technology with Si would be another important step for GaN-based device development. Furthermore the use of 12” diameter Si wafer would improve device throughput and lower unit device fabrication cost.

2.2 Application of GaN in LED

After the first GaN-based LED was reported in 1971, there were many efforts to fabricate similar structures [45]. These devices, however, were not conventional *p-n* junction LEDs due to the difficulty of *p*-type doping of GaN. Rather, these were metal-insulator-*n*-type semiconductor (MIN) structures, where heavily compensated insulating GaN was grown on uncompensated *n*-type GaN. As shown in Fig. 2-1, a side contact to the *n*-type GaN was fabricated due to the difficulty of chemical etching of GaN [46]. In this MIN structure light emission was caused by the impact of hot electrons with ionized luminescence centers in the compensated GaN region [47]. A blue-green GaN numeric display was demonstrated by selective deposition of metallic electrodes with MIN electroluminescent diode [48].

As mentioned earlier, the first *p-n* junction GaN based LED was fabricated by utilizing LEEBI treated, Mg doped, *p*-type GaN and intrinsic *n*-type GaN [49]. 3 μm thick undoped *n*-type GaN was deposited using trimethylgallium (TMG) and NH_3 on an AlN buffer layer. 0.5 μm thick *p*-type GaN was deposited on the *n*-type GaN followed by LEEBI treatment. The LED showed near-band-edge UV emission (~ 370 nm) of photo-electroluminescence (PL) spectrum.

The blue *p-n* junction LED was developed by co-flow metal-organic chemical vapor deposition (MOCVD) using TMG, NH_3 , SiH_4 , and Cp_2Mg [50]. The peak wavelength and FWHM from PL were 430 nm and 55 nm, respectively. The output power was 42 μW and the external quantum efficiency was 0.18%. To improve the output power and quantum efficiency, a

Si:In_{0.2}Ga_{0.8}N active layer was grown between *n*- and *p*-type GaN [51]. The output power was improved to 125 μ W, and the external quantum efficiency was 0.22%. A highly efficient blue LED with 5.4% quantum efficiency was fabricated by an InGaN/AlGaN double-heterostructure where Zn and Si were co-doped into the active layer [52]. The output was as high as 3 mW, and the peak wave length was 450 nm. The violet emission from In_{*x*}Ga_{1-*x*}N (*x*<2) band-to-band recombination was insufficient for display applications. Thus, Zn and Si were incorporated to form donor and acceptor levels 20-30 meV below the conduction band, and 0.4-0.5 eV above the valence band, respectively. This enhanced the radiative recombination, and reduced the energy difference between electron and hole states.

Green and yellow LEDs were fabricated by utilizing single quantum well (SQW) structures with an increased indium fraction in the InGaN active layer. The active layer was deposited between 50 nm thick Si-doped In_{0.05}Ga_{0.95}N and 100 nm thick Mg-doped Al_{0.1}Ga_{0.9}N layer as shown in Fig. 2-2. The peak wavelength of blue, green, and yellow LEDs were 450, 525 and 590 nm respectively. The output power and external quantum efficiency were 4 mW and 7.3% for blue LEDs, 1.5 mW and 2.1% for green LEDs, and 0.5 mW and 1.2% for yellow LEDs. The conventional green GaP LED shows a peak wavelength of 555 nm with an output of 0.04 mW, and the green AlInGaP LED shows a peak wavelength of 570 nm with output of 0.4 mW [53]. Thus, InGaN SQW LEDs have much higher output power than conventional green LEDs.

The white LED was introduced by Nakamura et al., and is now being commercialized by Nichia. It is composed of a blue LED which is packaged with yttrium aluminum garnet (YAG) phosphor to convert blue light into white as shown in Fig. 2-3 [7]. This white LED shows an external quantum efficiency of 3.5%, and 1 mW output. White LEDs are an attractive alternative

to the conventional light bulb due to their longer lifetime and better conversion efficiency of electric power to visible light.

LEDs have many potential applications from light bulbs to display panels. LED flat displays consisting of thousands of LED are suitable for indoor and outdoor applications due to the high output intensity of the LED [54]. The commercial Toshiba module is 128 mm × 256 mm, and contains 2048 units of LED. The more modern 1.28 m × 2.56 m panel contains 204,800 LED units. The indoor application model from Sharp contains 614,400 LED units in a single panel. The market for LED using GaN and other III-V compounds continues to grow. After 10.8% growth in 2008, the LED market is expected to grow 2.9% in 2009 due to its application in LCD TV backlight unit, even though the overall semiconductor market is set to decline 9.4% [55]. The number of applications of GaN based LEDs is expected to keep growing, and more research in this field is required.

2.3 Atomic Layer Deposition of GaN

Though ALD of GaN has the potential to be used in many optoelectronic applications, very little work has been reported on ALD of GaN. The first report on ALD of GaN, by Khan et al., employed triethylgallium (TEG) as a Ga source and NH₃ as a N source [56]. GaN film was deposited on a thin AlN buffer layer on a sapphire substrate which was grown at 550 °C using triethylaluminum (TEA) and NH₃. The growth temperatures ranged from 450 to 900 °C. The self-saturation limit for the exposure time of TEG was found at the growth temperature of 900 °C. Single crystal GaN was grown at 450 °C, which is well below 700 °C, required for conventional MO-CVD. The band-edge photoluminescence (PL) intensity and line width of ALD film grown at 900 °C were as good as MO-CVD grown film at 1040 °C. Even though good optical quality GaN was grown at lower temperatures, the ALD characteristics such as process temperature window were not investigated. Moreover, the self-saturation limit was

found at a relatively high temperature (900 °C), which is believed to be out of the process temperature window.

Karam et al. reported ALD-GaN using Trimethylgallium (TMG) as a Ga source and NH₃ as a N source [57]. This work employed unique rotating susceptor ALD reactor. Similar to previous GaN reports, GaN is deposited on a thin AlN buffer layer on a sapphire substrate. Single crystal GaN was grown at 550 °C, and the PL spectra of this GaN film showed a strong emission peak of 3.42 eV. Though good optical and structural quality films were grown at relatively low temperature, ALD characteristics were not investigated.

It is known that the relatively unstable MO sources show a narrow process temperature window in ALD of most materials. To resolve this issue, Ga chloride sources such as GaCl and GaCl₃ have been used with NH₃ for the ALD growth of GaN. The ALD growth of GaN using GaCl as Ga source was reported by Koukitu et al. [58]. The ALD-GaN film was deposited on GaN buffer layer, which is grown on a GaAs substrate by MO vapor phase epitaxy (MOVPE). GaCl was obtained by the reaction of metallic Ga and HCl at 780 °C. ALD characteristics such as self-saturation limit and process temperature window were investigated in this study. The self-saturation limit for GaCl exposure time was found over 400 °C of growth temperature. Within the bounds of the self-saturation limit, ALD-GaN is shown to have a cubic structure with [001] direction perpendicular to GaAs(001) substrate.

Tsuchiya et al. reported ALD of GaN using GaCl₃ as Ga source due to its relatively high vapor pressure for [59]. A thin GaAs buffer layer grown on GaAs was used as a substrate. They failed to find the self-saturation limit of GaCl₃ exposure time. From X-ray diffraction (XRD) measurements, it was shown that single crystal GaN was grown on GaAs(111). From reflection high-energy electron diffraction (RHEED), GaN was found to have the hexagonal structure,

specifically, wurtzite structure. ALD of GaN using chloride Ga sources such as GaCl and GaCl₃ showed ALD characteristics, and fairly good structural quality. However, Cl incorporation in the film, which is deleterious to device performance, was not considered, even though this is one of the most important issues with using halide metal sources.

2.4 Doping of GaN

2.4.1 *n*-type Doping of GaN

There have been many reports of achieving *n*-type doping of GaN by introducing group IV elements such as Si and O. The *n*-type doping of GaN using SiH₄ as a dopant was reported by various groups [60, 61]. The *n*-type GaN was grown by MOCVD using TMG as a Ga source, NH₃ as a N source and SiH₄ as an *n*-type dopant. A GaN buffer layer deposited on *c*-sapphire was used as a substrate. The carrier concentration determined by room temperature Hall measurement was found to increase up to $2 \times 10^{19} \text{ cm}^{-3}$ by increasing the flow rate of SiH₄, whereas the mobility of the carrier decreased from 600 to $100 \text{ cm}^2 \text{ V}^{-1} \text{ s}^{-1}$ under the same increase. The activation energy of *n*-GaN from SiH₄ was reported between 12 and 17 meV [62]. The ratio of free electron to incorporated Si atoms was in the range of 0.5 ± 0.1 .

Si₂H₆ was employed as an alternative *n*-type dopant due to its higher reactivity [63]. The *n*-type GaN layer was grown by MOCVD using TMG as a Ga source and NH₃ as a N source. The carrier concentration was increased up to $4 \times 10^{19} \text{ cm}^{-3}$ with increasing Si concentration. From the room temperature Hall measurement, the efficiency of incorporation of carriers is kept constant with the slope of 1 for carrier concentrations from 1×10^{17} to $4 \times 10^{19} \text{ cm}^{-3}$. The carrier mobility decreases from 450 to $100 \text{ cm}^2 \text{ V}^{-1} \text{ s}^{-1}$ as carrier concentration increases. The resultant carrier concentration at a given Si concentration was found to be independent of growth temperature in the range of 980-1040 °C.

Oxygen is of particular interest as a possible alternative *n*-type dopant due to its position next to N in the periodic table and its suspected role as a background impurity in as-grown GaN. Several groups have shown O to act as a donor for GaN [64-67]. To employ O as an *n*-type dopant, O¹⁶ ions were implanted to MOCVD grown GaN. The resulting carrier concentration was $\sim 1 \times 10^{17} \text{ cm}^{-3}$, and the mobility was $100 \text{ cm}^2 \text{ V}^{-1} \text{ s}^{-1}$. The activation energy was $\sim 29 \text{ meV}$, and the activation efficiency was poor.

2.4.2 *p*-type Doping of GaN

There have been many efforts aimed at *p*-type doping of GaN by introducing group II and IV elements. The most investigated dopant for *p*-type GaN is Mg. Most of reports on Mg doping in GaN employed MOCVD of GaN on buffer layered sapphire with the co-flow of a Mg source. However, it is known that one of the biggest roadblocks to achieve *p*-type doping of GaN is the compensation of electrons by Mg or Mg containing complexes. To overcome this compensation issue, there have been many efforts to activate Mg acceptors. As mentioned in Chapter 2.1, Amano et al. showed the first *p*-type conductivity by activating Mg-doped GaN with LEEBI. After LEEBI activation, the hole concentration was increased to $2 \times 10^{16} \text{ cm}^{-3}$, and the mobility was $8 \text{ cm}^2 \text{ V}^{-1} \text{ s}^{-1}$. Also, the high resistivity due to compensation was dramatically decreased down to $\sim 35 \text{ } \Omega\text{-cm}$. Nakamura et al. confirmed the work of Amano et al. using the same activation method. Hole concentrations as high as $3 \times 10^8 \text{ cm}^{-3}$ and mobilities as large as $15 \text{ cm}^2 \text{ V}^{-1} \text{ s}^{-1}$ were obtained after LEEBI treatment even though the initial hole concentration was $2 \times 10^{15} \text{ cm}^{-3}$.

Nakamura et al. and Götz et al. demonstrated that the activation of Mg acceptors can also be achieved by post-growth thermal annealing in the temperature range of 600-775 °C [35, 68]. The *p*-type GaN grown by co-flow MOCVD was annealed by rapid thermal annealing (RTA) for

5 min. After thermal annealing, the hole concentration was increased up to $2.3 \times 10^{18} \text{ cm}^{-3}$. And the mobility and resistivity were decreased to $10 \text{ cm}^2 \text{ V}^{-1} \text{ s}^{-1}$ and $2 \text{ } \Omega\text{-cm}$, respectively.

Brandt et al. investigated the effect of post-growth annealing with hydrogenation using H-plasma above $500 \text{ }^\circ\text{C}$ [69]. The hole concentration of *p*-GaN activated by post-growth annealing was reduced by one order of magnitude after the hydrogenation process. Based on this observation, it was suggested that H plays a crucial role in passivating the Mg acceptor, and the H-passivation is mitigated by thermal annealing. For this reason, Neugebauer et al. theoretically investigated Mg-H complexes and concluded that H does not form a bond to Mg atom, but prefers the anti-bonding site of one of the N neighbors [70]. Thus, the Mg-H complex has a modified H-N bond, and the dissociation barrier for this bond was estimated to be 1.5 eV. This H-N bond compensates the electrons, and this compensation can be reduced by breaking Mg-H or H-N bond with a thermal annealing process.

It was reported by Myoung et al. that molecular beam epitaxy (MBE)-grown GaN doped with Mg is *p*-type without a thermal activation process [71]. At room temperature, Mg-doped GaN grown by MBE showed the free hole concentration above 10^{18} cm^{-3} with a mobility of $\sim 10 \text{ cm}^2 \text{ V}^{-1} \text{ s}^{-1}$ without post-growth thermal annealing. This is consistent with results of previous reports on compensation by H complexes. H is absent during MBE processes, and this prevents the formation of H complexes in the *p*-GaN film. Thus, the relatively high hole concentration of *p*-GaN was obtained without thermal annealing activation. Previously mentioned *p*-GaN activated by either LEEBI or thermal annealing showed a binding energy of the Mg acceptor in the range of 230-260 meV. This binding energy was found to be temperature dependent.

Though Mg has been a reasonable *p*-type dopant for GaN, there is still the question of whether any other acceptors with smaller binding energies exist, and whether they are suitable

dopants that can be incorporated at high concentration. Zn, Cd, and Be also belong to group II, like Mg, and can substitute for Ga in GaN as a *p*-type dopant. Bergman et al. reported the *p*-type doping of GaN using Zn and Cd as dopants, and showed the identity of the active recombination centers from transient luminescent spectra and time resolved luminescence measurements [72]. The dominating recombination centers created by Zn and Cd doping in GaN were identified as substitutional acceptors, Zn_{Ga} and Cd_{Ga}. The binding energies of Zn and Cd acceptors were measured as 0.34 and 0.55 eV, respectively. These results indicate that the acceptor levels by Zn and Cd incorporation in GaN are deeper than Mg acceptor level, and therefore less efficient in creating free holes at room temperature. Neugebauer and Van de Walle reported a comprehensive investigation of acceptor impurities in GaN based on first principle total energy calculations [73]. From this calculation, none of the candidates (Li, Na, K, Be, Zn and Ca) exhibited better characteristics than Mg. Only Be is expected to be a potential alternative dopant, though it may have solubility limitations and compensation issues by Be interstitial donors.

Brandt et al. reported the growth of *p*-type GaN by GaN-MBE with co-doping of Be and O [74]. Be is supplied by evaporation from an effusion cell, and O is supplied by H₂O in the background pressure. A concentration of $5 \times 10^{20} \text{ cm}^{-3}$ Be and O atoms was incorporated into GaN film at 650 °C. Hall measurements showed *p*-type conductivity with a hole concentration of 10^{18} cm^{-3} and a hole mobility of $150 \text{ cm}^2 \text{ V}^{-1} \text{ s}^{-1}$. Zopler et al. achieved *p*-type doping of GaN by co-implanting Ca with P at concentrations of 10^{19} cm^{-3} [75]. The measured binding energy of holes was 169 meV for Ca. The measured hole mobility was $7 \text{ cm}^2 \text{ V}^{-1} \text{ s}^{-1}$. These properties showed that Ca can be used as a *p*-dopant for GaN. The possible acceptors for various III-V materials are summarized in Table 2.1 with binding energies [76].

2.5 Challenges in Interconnects

2.5.1 RC Delay in Interconnects

There have been demands on increased transmission speed as the individual feature sizes of devices in integrated circuits (IC) shrinks. One of the biggest roadblocks to achieving maximum signal transmission in emerging chip and system architecture is to minimize the resistance times capacitance (RC) time delay. RC delay has replaced intrinsic device delay as the speed limiter in sub-quarter-micron device nodes, primarily due to the higher RC time constant in the narrower, more closely spaced interconnect lines. The time delay in an interconnect circuit depends on two factors; the resistance of the conductor and the capacitance of the dielectric material. For a MOS circuit, the RC delay is defined in terms of the circuit response [77].

$$V_{out}(t) = V_{out}(\max) \left[1 - \exp\left(\frac{-t}{RC}\right) \right] \quad (2-1)$$

where the he output voltage of the circuit at time t is $V_{out}(t)$, maximum output voltage is $V_{out}(\max)$, the resistance of the metal line is R , and the total capacitance of the circuit is C . The resistance of the interconnect line is defined in terms of its length L , width W , thickness T_m , and resistivity ρ .

$$R = \rho \frac{L}{WT_m} \quad (2-2)$$

The capacitance between the silicon substrate and the metal line (metal to ground), C (metal-ground), is given by Equation 2-3.

$$C(\text{metal} - \text{ground}) = \epsilon_0 \frac{WL}{T_d} \quad (2-3)$$

where ε and T_d are the dielectric constant of the dielectric material and thickness of the dielectric line, respectively, and ε_0 is the permittivity of free space. The capacitance between two metal lines ($C(\text{metal-metal})$) separated by distance D is given by Equation 2-4 [78].

$$C(\text{metal} - \text{metal}) = \varepsilon_0 \frac{T_m L}{D} \quad (2-4)$$

The total capacitance, C , can then be calculated from Equations 2-3 and 2-4.

$$C = K(C(\text{metal} - \text{ground}) + C(\text{metal} - \text{metal})) = K\varepsilon_0 L \left(\frac{W}{T_d} + \frac{T_m}{D} \right) \quad (2-5)$$

K is a constant that depends on the fringing field effect. The RC delay is calculated from Equations 2-2 and 2-5.

$$RC = \frac{K\varepsilon_0 \rho L^2}{WT_m} \left(\frac{W}{T_d} + \frac{T_m}{D} \right) \quad (2-6)$$

As the critical device dimension shrinks, $C(\text{metal-metal})$ dominates the overall capacitance C [79]. The RC delay can then be written as Equation 2-7.

$$RC = \frac{K\varepsilon_0 \rho L^2}{WD} \quad (2-7)$$

For local interconnects the shrinking of the transistor leads to a corresponding decrease in L , W and D . Therefore, the actual delay in the local interconnect does not increase with device scaling. However, the chip area increases with each successive technology node. This leads to an increase in the length of global interconnects and a corresponding increase in the RC time delay as shown in Fig. 2-4 [80].

2.5.2 Electro-migration in Interconnects

Electro-migration is the phenomenon caused by the movement of metal atoms to the direction of electron flow in high current density interconnects. Metal atoms in interconnects are

known to have higher mobility under higher operating temperature which is popular in current microprocessors. When high energy electrons transfer their momentum to these mobile metal atoms, there is a movement of metal atoms in the direction of electron flow. This atom movement leads to formation of voids at the cathode and hillocks at the anode as shown in Fig. 2-5 [81].

Electro-migration, which causes failure of the circuit, is one of the most important concerns for the reliability of interconnects. As the interconnect dimensions shrink down, the current density in interconnects increases. Thus, the scaling of interconnects requires higher electro-migration resistance in interconnect materials. For Al-based metallization, electro-migration becomes a major concern. Figure 2-6 shows that the mean time to failure for Al interconnects dramatically decreases if the current density in the interconnect exceeds 3 MA/cm^2 [82].

2.5.3 Diffusion of Cu into Si

To solve primary challenges in metallization such as *RC* delay and electro-migration, Cu has been used as a substitute for Al. The resistivity of pure Cu ranges from 1.7 to $2.0 \mu\Omega\text{-cm}$, which is much lower than Al. This lowered resistivity attributes to the decrease of *RC* delay. Also, Cu is known to have higher resistance to electro-migration. For these reasons, Cu is currently used as interconnect material in semiconductor industries. However, there are some issues with the use of Cu as a interconnect material. The primary issue is the diffusion of Cu into Si.

Cu is known to diffuse extremely fast in Si. The diffusion coefficient of Cu in Si at 500°C is $2.0 \times 10^{-5} \text{ cm}^2/\text{sec}$ [83]. Furthermore, Cu is mobile in Si even after annealing. And, Cu can travel significant distances within Si waferd even at room temperature. The interaction of Cu with Si depends on the doping of the Si substrate. In *n*-type Si, Cu forms neutral or negatively

charged precipitates. There is no barrier or electrostatic repulsion between Cu precipitates and interstitial Cu since interstitial Cu is positively charged in Si. Thus, Cu easily forms Cu_xSi precipitates in *n*-type silicon. This Cu_xSi can act as recombination centers for minority carriers and significantly lower minority carrier lifetimes [83]. In *p*-type Si, Cu forms positively charged precipitates [84]. There is electrostatic repulsion between the positively charged Cu precipitates and positively charged interstitial Cu, which acts as a barrier in nucleation and precipitation of copper in *p*-type Si. If there is no native oxide on the surface of *p*-type Si wafer, Cu out-diffuses from the bulk to the surface. Since segregated Cu on the surface can be easily etched by a H_2O_2 and HF mixture, it is inferred that the Cu does not form Cu_3Si precipitates. For *n*-type Si, out-diffusion occurs only if Si is heated to 400 °C.

The primary reason why Cu is extremely undesirable in Si is that it forms deep level traps in the band gap of Si as shown in Fig. 2-7. If Cu exists in the triplet state, it forms three acceptor levels in the Si band gap at 0.24, 0.37 and 0.52 eV [77]. Since Cu diffuses extremely fast in Si, detrimental effects of Cu can spread throughout the device. Cu is also detrimental if it diffuses into the dielectric film. Cu in dielectrics decreases the breakdown voltage of the dielectric and also increases the parasitic capacitance. Thus, benefits from low- κ dielectric film are negated.

2.6 TaN as Diffusion Barrier

2.6.1 CVD of TaN

TaN diffusion barriers have been deposited by CVD to avoid the side wall deposition problems of PVD. In CVD growth of TaN, both halide and metal organic Ta sources have been employed. Halide sources such as TaCl_5 , TaF_5 , and TaBr_5 have been investigated as CVD precursors for TaN. CVD-TaN films using TaCl_5 and NH_3 were grown at the low deposition temperature of 350 °C [11]. However, the film was not suitable for diffusion barrier applications because of its high resistivity ($> 10,000 \mu\Omega\text{-cm}$) and high Cl contamination ($\sim 4.5 \text{ at. } \%$).

Moreover, Cl contamination is difficult to reduce since the Ta-Cl bond is very strong. CVD-TaN films using TaF₅ and NH₃ were reported to have relatively low resistivity of 1650 μΩ-cm at the growth temperature of 350 °C [11]. However, the film has considerable F contamination (~4.0 at. %) and poor step coverage. The poor step coverage can be explained by considering the high growth rate of deposition. Because a high growth temperature is required to obtain suitable diffusion barrier properties, thermal CVD using TaCl₅ or TaF₅ has not been investigated further.

TaBr₅ has been studied as a precursor for CVD of TaN using H₂ and NH₃ as co-reactants. It is believed that halogen contamination is lowered by smaller diffusivity of TaBr₅ into the film due to larger atom size of Br than Cl and F. Moreover, lower deposition temperature is required for the reaction of TaBr₅ and NH₃ due to lower bonding energy of Ta-Br in TaBr₅. Chen *et al.* reported CVD deposition of TaN films at growth temperatures of 350 to 500 °C using TaBr₅, H₂ and NH₃ [12]. The films were N-rich with N:Ta ratios varying from 1.75:1 to 1.87:1 for growth temperatures between 350 and 500 °C. The N-rich film deposited with TaBr₅ indicates that the film is possibly Ta₃N₅ instead of TaN. The Br content in the film decreased with increased deposition temperature. The Br content was highest (~5 at. %) at the growth condition of 350 °C, while it was below the detection limit of AES for deposition at the growth temperature of 500 °C. Film resistivity also showed a strong dependence on deposition temperature with the lowest resistivity of 5040 μΩ-cm at 500 °C. To evaluate the diffusion barrier performance of TaN films, Kaloyeros et al. employed extensive barrier tests on TaN films deposited at 425 °C [85]. The Cu/TaN/Si stack was annealed between 450 and 650 °C to determine the barrier failure temperature. From post-anneal XRD measurement, it was confirmed that TaN barrier film successfully prevented bulk diffusion of Cu up to 650 °C annealing temperature.

The other approach for TaN-CVD is to employ metal organic Ta sources such as Ta(NMe₂)₅ (pentakis(dimethylamido)tantalum, PDMAT), Ta(NEt₂)₅ (pentakis(diethylamido)tantalum, PDEAT) and (NEt₂)₃Ta=NBu (tertbutylimidotris(diethylamido)tantalum, TBTDET). For these metal organic Ta sources, detrimental halide residues are not an issue. There was, however, high C incorporation in MOCVD TaN films which lead to high electronic resistivity up to $\sim 10^6 \mu\Omega\text{-cm}$ in the case of the amorphous C phase.

TaN from PDEAT showed high electronic resistivity up to $6 \times 10^5 \mu\Omega\text{-cm}$ with high C content (~ 30 at. %) under single source deposition [86]. The addition of NH₃ as an additional nitrogen source, however, decreases the electronic resistivity down to $7000 \mu\Omega\text{-cm}$ while lowering C content from 30 to 1 at. %. To obtain a reasonable range of resistivity ($< 1000 \mu\Omega\text{-cm}$), the growth temperature should be higher than 600 °C. Also, TaN from PDEAT and NH₃ exhibited better Cu diffusion barrier performance compared to single source deposition using only PDEAT. However, the step coverage of the film decreased from 80% to 56% with addition of NH₃, which is ascribed to switching the growth condition to the mass-transfer limited regime. TaN deposited with PDMAT showed the insulating Ta₃N₅ phase resulting in high resistivity ($> 10^6 \mu\Omega\text{-cm}$) [87]. The film also had the high C incorporation even with addition of NH₃.

TaN using TBTDET as Ta source showed a relatively low resistivity ($920 \mu\Omega\text{-cm}$) at 650 °C [88]. The deposition rate was almost independent of the growth temperature (450 to 650 °C), indicating growth in the mass transfer-controlled regime. From XPS measurement, TaN film has 10 at. % of C incorporation. A comparison study of diffusion barrier performance between PVD TaN and CVD TaN from TBTDET showed the barrier failure temperature of 650 °C for PVD and 600 °C for CVD. This exhibits that the PVD TaN possesses better diffusion barrier properties than CVD TaN due to its higher film density.

2.6.2 ALD of TaN

ALD is a self-limiting growth method consisting of alternative dosing of chemical species to control the target material in layer-by-layer manner while CVD delivers all required reactants to the reactor simultaneously. Each precursor is exposed to the substrate sequentially, which results in uniform layer adsorption of precursor on the substrate by chemisorptions. The most important characteristic of ALD is obtained from this step, which is self-saturation. The self-saturation limits further adsorption of precursors by passivating the available adsorption sites after the saturation coverage. Due to this self-saturation nature, ALD films show much better conformality and uniformity than CVD films. These characteristics of ALD films are essential for diffusion barrier films to minimize the barrier's impact on resistance per unit length in Cu interconnect. Also, relatively lower growth temperatures make ALD a preferred deposition method for diffusion barriers [26].

For ALD of TaN, two types of Ta precursors such as metal halide and metal organic were employed. TaCl₅ is the most commonly used Ta halide precursor. The first report on ALD of TaN employed TaCl₅ as a Ta source with NH₃ as a N source [89, 90]. The film growth rate was 0.22 - 0.24 Å/cycle and the temperature window was in the range of 300 - 500 °C. The films deposited with the TaCl₅ and NH₃ were N-rich and polycrystalline. From XRD measurements, the films deposited at 400 °C were tetragonal Ta₃N₅ phase. The Cl incorporation in the film was less than 5 at. %. Cl impurity level in the film decreased with increased deposition temperature. The resistivity of the film varied from 0.5×10^6 to $200 \times 10^6 \mu\Omega\text{-cm}$. The high resistivity of the film came from the presence of the non-conducting Ta₃N₅ phase.

There has been a report of plasma assisted ALD (PAALD) of TaN films using TaCl₅ and H₂ + N₂ plasma [91]. N content in the film varied as Ta₂N, TaN, and Ta₃N₅ with the partial pressure of N₂ in the plasma. The ALD process window was not found over the entire growth

temperature range. The resistivity of TaN films was much lower compared to thermal ALD films, varying between 350 and 400 $\mu\Omega\text{-cm}$. Cl content in the film was less than 3 at. %, and H incorporation was as high as 11 at. %. Similar to thermal ALD of TaN using TaCl₅, PAALD also showed a decrease in Cl level with the increase of deposition temperature. Overall, PAALD showed good electronic quality films, suitable for diffusion barrier applications. However, resulting films were not in the amorphous phase, and the Cl incorporation issue was not completely solved.

To solve the halogen incorporation issue of halide precursor, metal organic precursors such as TBTDET and PDMAT have been used in ALD of TaN. As mentioned in the previous section, CVD-TaN films using these metal organic precursors showed high C impurities and high resistivity. The ALD process is expected to lower C impurity levels at even lower deposition temperatures.

TBTDET was reported to be employed as a Ta source with NH₃ as a N source for thermal ALD of TaN [92]. Deposited TaN films were in amorphous phase between 150 and 300 °C of growth temperature. The films deposited were Ta-rich and the N/Ta ratio was 0.73. As expected, C impurity levels of deposited films were less than 5 at. %. The resistivity of the film was very high ($> 10^6 \mu\Omega\text{-cm}$ at 260 °C) despite high Ta content in the film. The resistivity of the film decreased down to 15000 $\mu\Omega\text{-cm}$ when the deposition temperature was increased to 450 °C. Choi et al. reported the temperature window between 200 and 250 °C for the ALD process using TBTDET and NH₃ [93].

PAALD of TaN films using TBTDET with H radical has been reported [94]. The H radical was used as a reducing agent for TBTDET. Unlike thermal ALD, TBTDET was employed as a single source precursor. N atoms attached to Ta by single bonds were removed by H radicals,

while double bonded N atoms to Ta remain, leading to stoichiometric TaN. Resulting TaN films were Ta-rich with N/Ta ratio of 0.6. The C impurity level, however, was very high as 20 at. %. The films were polycrystalline and had low resistivity of $1000 \mu\Omega\text{-cm}$. Overall, the plasma processing improved the electronic properties of the films. The deposited film, however, was in the polycrystalline phase which is not preferred for an effective diffusion barrier. Also, diffusion barrier performance of ALD TaN from TBTDET was not investigated.

PDMAT was another metal organic Ta source for TaN ALD. Thermal ALD of TaN has been reported using PDMAT and NH_3 [95-98]. The ALD temperature window was found between 225 and 300 °C with a constant growth rate of 0.3 \AA/cycle . The composition and microstructure of deposited films showed strong dependence on substrate. The films deposited on Si, SiO_2 and Cu were N-rich with N/Ta ratio of 2 at 275 °C growth temperature. However, the films deposited on Ta were Ta-rich with N/Ta ratio of 0.5. The C level in the film was as low as 2 at. %. The films deposited were in nanocrystalline phase with average grain size of 4 nm. The diffusion barrier performance was evaluated in the scope of thermal stability. Cu diffusion was prevented at 750 °C of annealing temperature for 30 min by 10 nm thick TaN diffusion barrier. Even though ALD-TaN film from PDMAT showed suitable diffusion barrier properties, the electronic resistivity of the film was too high to be measured by standard four point probe.

To solve the high resistivity issue, PAALD of TaN using PDMAT has been investigated. Kim et al. investigated the effect of plasma on the deposition of TaN_x film [99]. The ALD temperature window was found between 225 and 300 °C of growth temperature. The deposited film is Ta-rich, with N/Ta ratio in the range 0.7 to 0.8. The C impurity level in the film varied from 2 to 14 at. % with N_2 flow rate. The resistivity of the film was as low as $350 \mu\Omega\text{-cm}$ at 250 °C of deposition temperature. Diffusion barrier testing showed that Cu diffusion was

prevented at 750 °C of annealing temperature for 30 min by 3 nm thick TaN diffusion barrier. Overall, PAALD of TaN from PDMAT provides improved diffusion barrier properties in the scope of electronic resistivity as well as minimum thickness to prevent Cu diffusion.

To summarize, both halide and metal-organic Ta precursors have been used to deposit ALD-TaN films. The biggest challenge for halide Ta precursors was the incorporation of detrimental halogen atoms in the film at lower growth temperatures. Moreover, deposited film was in the insulating Ta₃N₅ phase instead of the conducting TaN phase. The use of metal organic Ta precursors could solve halogen incorporation issues. However, other challenges such as the C incorporation and high film resistivity by Ta₃N₅ phase were brought up at low growth temperature. Thus, plasma processing was introduced to obtain low resistivity TaN film with a favorable N/Ta ratio.

2.7 Cu Metallization

2.7.1 Processing of Cu Interconnect

As mentioned earlier, Cu has been employed as an interconnect material to solve *RC* delay and electro-migration problems. The most prevailing process for Cu interconnect integrity is dual-damascene processing. The notation of dual-damascene is used to describe a patterning process of metallization. For Al metallization, Al is deposited first, followed by patterning with lithography and etching steps. The SiO₂ dielectric was then deposited into the Al pattern. On other hand, for Cu metallization, the scheme of process is reversed. The dielectric film is deposited first, and then the lines and vias for the metals are patterned into dielectric using lithography and etching steps, followed by the deposition of Cu into lines and vias. Overburdens are then removed by planarization processes such as CMP.

Several key process elements have been developed to apply dual-damascene process to Cu metallization successfully. To remove overburden Cu effectively, the CMP process has been

developed with high polishing rates, no corrosion, and high selectivity. In addition, the lithography and reactive ion etching processes have been optimized for the dual-damascene patterning at required scales. Most of all, a proper Cu electroplating process contributes to the improved reliability of Cu interconnects from dual-damascene processing. Cu electroplating has the super-filling behavior by utilizing inhibitor additives [100]. The super-filling behavior is shown in Fig. 2-8.

This super-filling behavior leads to void-free and seam-free deposit of Cu into lines and vias. As shown in Fig. 2-9, void and seam are present for sub-conformal and conformal deposition, respectively. These voids and seams are fast diffusion pathways for Cu electro-migration. Thus, the fast diffusion pathways for Cu electro-migration can be eliminated by super-filling.

This super-filling behavior can be explained by activity and kinetics of a plating inhibitor at the top surface [101]. The inhibitor has relatively low activities in the hole bottom and bottom side walls which enhances the filling of hole bottom and bottom side walls. On the other hand, the inhibitor is active at the top surface, resulting in suppressed deposition rate at the top surface. This behavior of inhibitor leaves the hole open for filling until the hole is completely filled, which results in super-filling of hole.

2.7.2 Microstructure of Cu Thin Film for Various Deposition Methods

The microstructure of Cu thin films has attracted much interest recently because the micro-structural attributes such as grain size, grain size distribution, and crystallographic texture influence mechanical and physical properties of films. In particular, these micro-structural attributes are directly related to the anisotropic property variations in Cu. Also, the grain orientation of Cu is considered to influence the reliability of Cu. For example, the elastic modulus of Cu in (111) direction is 2.9 times larger than (100) direction [102]. Additionally, the

reaction rates for oxide and silicide formation of Cu, detrimental to device performance, are faster along (100) grain surfaces than along (111) grain surfaces [103, 104]. Also, Cu(111) grains generate (511) planes by twinning. The formation of twins is known to have beneficial effects for Cu thin film because twin boundaries are low diffusion pathways for electro-migration.

Table 2-2 shows the grain size, ratio of (111)/(100), and percent (111) versus (100) twins for Cu films grown by different deposition methods: PVD, CVD, and electroplating. Clearly, the grain size and twin volume fractions are shown to be considerably higher for the electroplated Cu films. It is known that twins are developed during grain growth, and are prevalent in large electroplated Cu grains. In contrast, PVD and CVD films show much fewer twins. This is believed to be originated from the small grain sizes of PVD films and the effect of grain boundaries in these films to relieve strain. As strain energy increases in a growing grain, twins are formed to relieve the pressure.

In summary, (111) orientation of Cu is preferred for better reliability due to low reaction rate for oxide and silicide formation. Also, the twinning effect is beneficial for Cu thin film due to lower diffusion pathways for electro-migration. It is demonstrated that PVD Cu has the most (111) orientation which is preferred for better reliability of Cu interconnect. It is also shown that electroplated Cu has the most twinning of (111) orientation for better electro-migration resistance.

2.8 Barrier Failure Mechanism

To identify a viable diffusion barrier for Cu metallization, the fundamental understanding of diffusion failure mechanism must be established. The dominating mass transport phenomenon in Cu/barrier integrity is the inter-diffusion phenomena of Cu. It is well known that the placement of chemically different atoms in proximity leads to atomic migration to lower the

overall free energy and establish equilibrium. This atomic migration is typically driven by concentration gradients, and accelerated by thermal energy [105].

Atomic migration results in a diffusion flux, with the net flow of atoms characterized by a diffusion coefficient, D . This is so called Fick's law, and written in Equation 2-8 where C is the atomic concentration, J the atomic flux per unit area per second, and x is the distance [106].

$$J = -D \frac{\partial C}{\partial x} \quad (2-8)$$

The temperature dependence of the diffusion coefficient D is in the form of an Arrhenius relationship as shown in Equation 2-9 where D_o is the diffusion coefficient at 0 K, Q is the activation energy for diffusion, κ is Boltzmann's constant, and T is the temperature in Kelvin [107]. Diffusion parameters such as D_o and Q are strongly dependent on the thermodynamic and kinetic properties of the defects responsible for diffusion.

$$D = D_o \exp\left(\frac{-Q}{\kappa T}\right) \quad (2-9)$$

In the case of the Cu/barrier integrity, three mechanisms typically dominate diffusion barrier failure: (a) diffusion of Cu through bulk defects in the barrier, (b) diffusion of Cu along grain boundaries in the barrier, and (c) loss of barrier integrity due to a metallurgical or chemical reaction with the Cu and/or substrate [108, 109]. For the failure by Cu diffusion through bulk defects of barrier, two types of bulk defects contribute to the diffusion; vacancies and dislocations. Diffusion through vacancies, dislocations, and grain boundaries has significantly different rates [110]. The lattice diffusion rates are proportional to the absolute melting temperature, T_m , of host material as shown in Equation 2-10 where A is proportionality constant dependent on many factors such as lattice structure and type of material.

$$D \approx AT_m \quad (2-10)$$

It is found that diffusion due to atom-vacancy exchange has the smallest A , thus corresponding to the slowest diffusion. Dissociated dislocations demonstrate intermediate A corresponding to intermediate diffusion rates. Diffusion along grain boundaries exhibits the largest A , and thus has the highest diffusion rate. Although Equation 2-10 is an empirical relationship, the reasonable guideline can be deduced in the selection of appropriate diffusion barrier materials, which is high melting temperature materials. Also, the dependency of diffusion rates on the type of diffusion pathway demonstrates that the formation of grain boundaries in diffusion barrier needs to be prevented.

Based on the discussion above, the microstructure of diffusion barrier plays the critical role in the barrier performance. In general, there are four different types of film microstructure: (a) single crystal, (b) polycrystalline, (c) nano-crystalline (i.e. polycrystalline with grain size below 5 nm), and (d) amorphous [111]. Among these microstructures, the polycrystalline barrier tends to show the poorest barrier performance due to grain boundaries throughout entire film thickness, providing an effective Cu diffusion pathway. On the other hand, a single-crystal barrier is the most ideal for a diffusion barrier due to the lack of diffusion pathways such as grain boundaries, dislocations, and vacancies. It is, however, unlikely to deposit single-crystal diffusion barrier due to the constraints on materials and processes such as lattice mismatch between barrier and substrate, and thermal budget limitation. Therefore, the diffusion barrier in amorphous phase is the most efficient for barrier applications due to fewer grain boundaries than poly or nano-crystalline as a result of large grain size.

Table 2-1. Acceptor binding energies for C, Mg, Be, Zn and Cd in various III-V semiconductors.
Taken from Ref [76]

Binding Energy (meV)	GaAs	InP	GaP	GaN
C	27	41.3	54	230
Be	28	41	55	250
Mg	28.8	48	59.9	250
Zn	30.7	46.4	69.7	340
Cd	34.4	57	102.2	550

Table 2-2. Microstructure of Cu films. Taken from Ref [112].

	PVD Cu	CVD Cu	Electroplated Cu
Grain size (μm)	0.4	0.9	3.8
(111)/(100) ratio	59/2	13/16	4/1
(111) twins	11%	15%	26%
Randomness	(111) textured	Random	Weak (111)

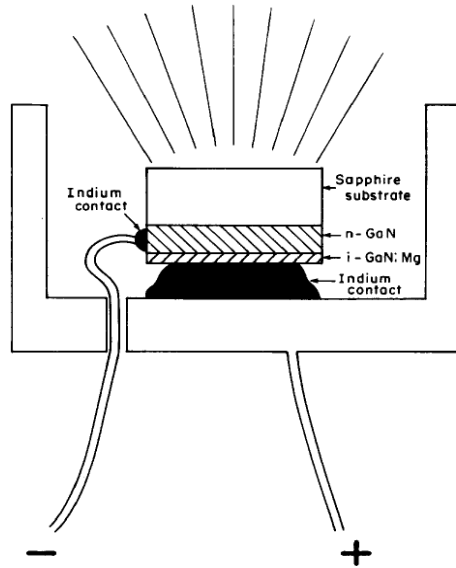


Figure 2-1. Experimental configuration of a typical m-i-n GaN LED. Taken from Ref. [46].

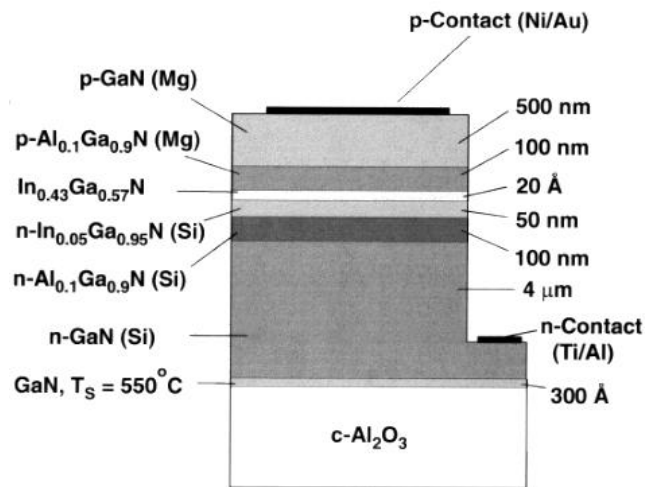


Figure 2-2. The structure of the high-brightness green-light-emitting diode with 20 Å thick $\text{In}_{0.43}\text{Ga}_{0.57}\text{N}$ quantum well as active layer. Taken from Ref. [53].

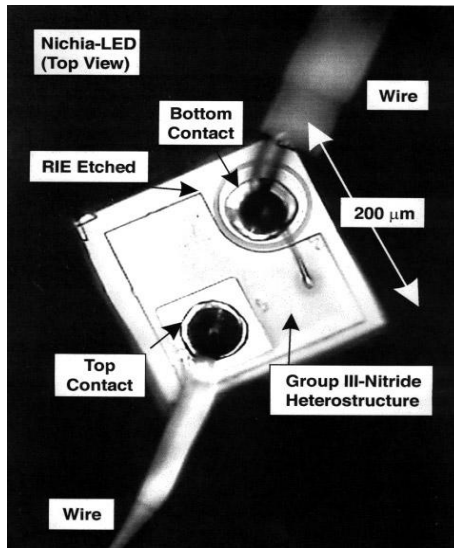


Figure 2-3. Top view of a blue LED fabricated by Nichia without plastic capsule. Taken from Ref [7].

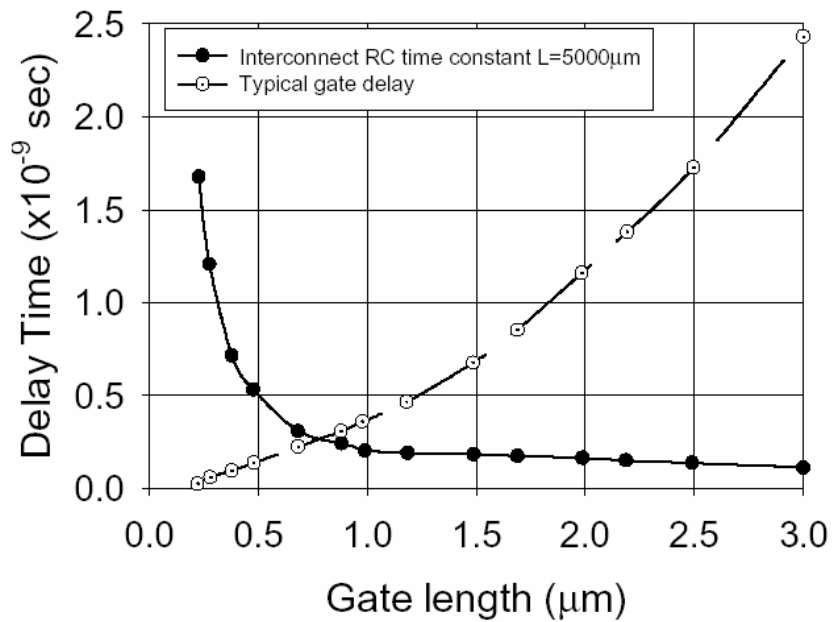


Figure 2-4. Effect of feature size scaling on total capacitance. Taken from Ref [80].

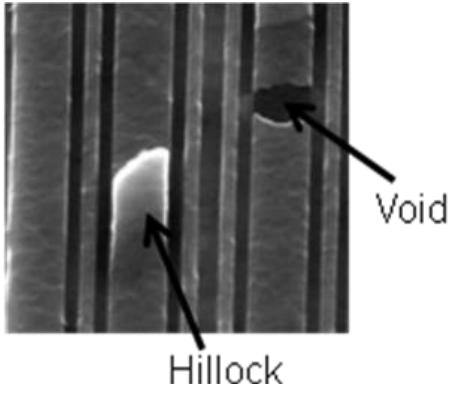


Figure 2-5. Damaged Al interconnect line showing the formation of hillock and void due to electro-migration. Taken from Ref [81].

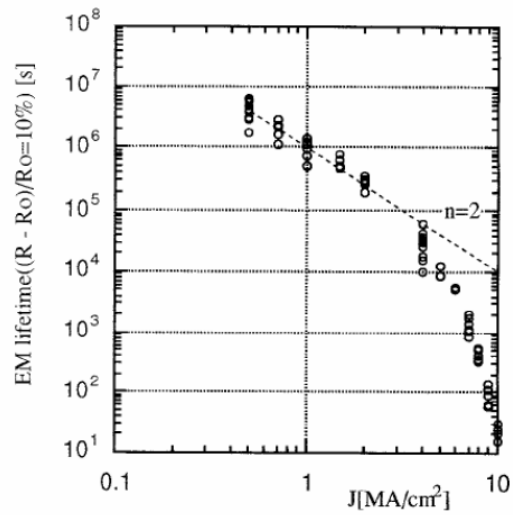


Figure 2-6. Electro-migration lifetime for aluminum interconnects at different current densities. Taken from Ref [82].

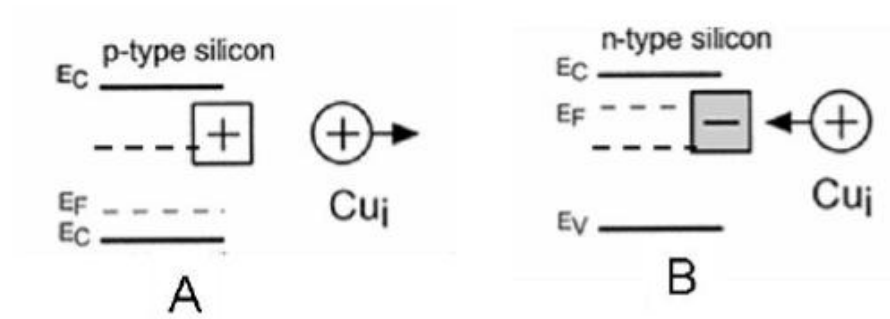


Figure 2-7. Band diagram of Cu impurity in silicon. A) *p*-type Si, B) *n*-type Si. [77]

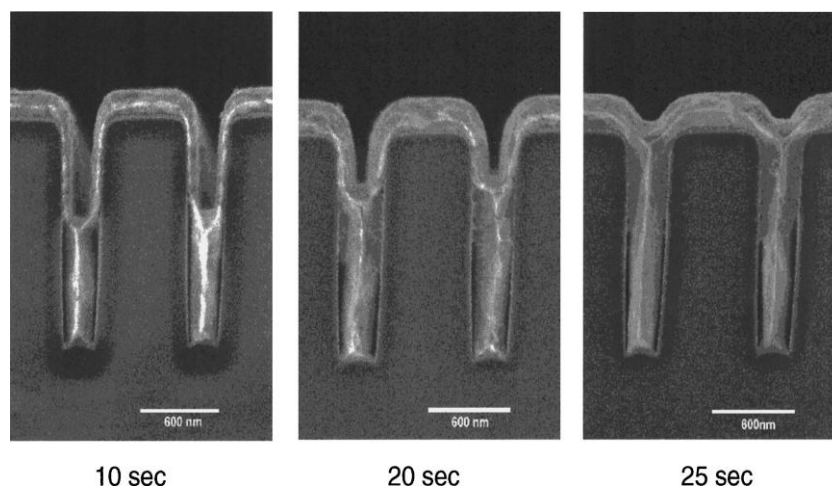


Figure 2-8. Hole-fill evolution for electroplated Cu with super-filling additives. Taken from Ref [100].

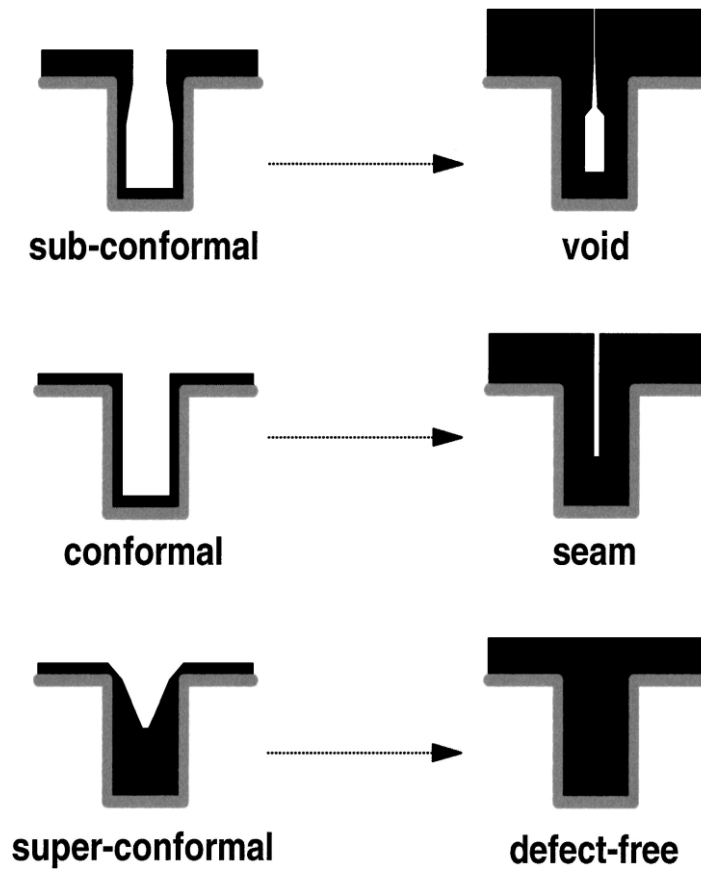


Figure 2-9. Evolution of hole-filling with different deposition conditions varying degrees of conformality. Taken from Ref [101].

CHAPTER 3 EXPERIMENTAL SETUP

3.1 GaN ALD Reactor Design and Setup

Figure 3-1 shows the overall process flow diagram (PFD) of the GaN ALD system. The bubbler, containing GaCl₃, is immersed in a constant temperature bath and heated to a pre-determined temperature. The heat bath temperature is set to a temperature to provide a sufficient vapor pressure (> 0.1 Torr for ALD) to ensure reasonable adsorption time. The N₂ carrier gas flow rate is adjusted to ensure saturation of the carrier gas with GaCl₃ for reproducible delivery rate. GaCl₃ was delivered to the reactor or the bypass line depending on the position of the pneumatic valves located upstream of the reactor. The gas lines between the bubbler outlet and the reactor entrance are heated ~10 °C higher than the bubbler temperature to prevent condensation of the precursor during delivery. The N₂ stream serves not only as a carrier gas but also as a sweeping (purging) gas in the purge step of ALD process. Cylinders of N₂ and NH₃ are contained inside a gas cabinet. All carrier, purge N₂, and NH₃ gases are metered to the reactor or bypass line by mass flow controllers (UNIT 8100) paired with a flow control-knob (FM304V).

Figure 3-2 shows the schematic of GaN ALD reactor used in this study. The reactor body is made of quartz glass. The graphite susceptor and RF coil are located in the growth zone. Each reactant and purge gas is delivered to the reactor through one of the multiple concentric quartz tubes. The substrate, Si or sapphire, is placed on quartz tray. The substrate with quartz tray is loaded into the reactor using magnetic robotic arm that is operated and controlled by an Intelligent Motion System-LI2. The main purpose of magnetic robotic arm is to load or unload the sample through the load-lock system. Load-lock system is commonly used to minimize impurities. Once the substrate is loaded into the reactor, it is placed on the graphite susceptor. A

RF generator (LEPEL T) heats up the graphite susceptor to indirectly heat the substrate to the desired temperature.

In ALD it is important to control the flow sequence of the reactants and purge gases. The gas manifold is equipped with three separate switching mode pneumatic valves (Swagelok SS4BYV35-C). Each pneumatic valve controls the on and off action of the gas flow into the reactor or the bypass line, resulting in the sequential flow of reactants and purge gas. Sequential exposure of each reactant and purge gas is managed by the control program encoded with National Instrument LabVIEW software.

A screen shot of the control program for GaN ALD process is shown in Fig. 3-3. The panel shows a typical cycle of GaN ALD process consisted with four steps. Each column with three of bright and dark circular bullets represents each cycle and the row corresponds to a particular pneumatic valve. The first step is the reactant 1 (GaCl_3) pulse (R1), where only GaCl_3 is dosed into the reactor, while purge N_2 and NH_3 are bypassed to vent. The second step is N_2 purge (P), where N_2 purge gas is dosed into the reactor, and GaCl_3 and NH_3 are bypassed to vent. In the third step, reactant 2 (NH_3) is pulsed to the reactor (R2), whereas GaCl_3 and N_2 purge gas are bypassed to the vent. After NH_3 pulse step, another N_2 purge step follows, which has exactly same configuration as second step (P). The duration time of each step and total number of cycles are controlled by the values in the pulse time and total cycle tabs, respectively. The signals from this program control the on and off actions of solenoid valves via data acquisition card (NI PCI-6514) and switching mode power supply (WRB24SX-U). Then, the solenoid valves control the flow of compressed air to the actuators of pneumatic valves, which control the direction of the gas either to the reactor or vent.

3.2 Chemical Equilibrium Analysis for Growth Temperature

The Ga source used in this study, GaCl₃, is a liquid at room temperature. There are several reactants, however, that can occur including disproportionation between GaCl₃ and GaCl. As a preliminary study, the equilibrium concentration was calculated as a function of temperature. To investigate dominant gas species in growth zone, a chemical equilibrium analysis was performed.

The gas species in the growth zone were investigated for GaCl₃ exposure step of GaN ALD process. For the thermodynamic analysis, the constant Ga/Cl molar ratio of 1/3 was applied to the Ga-Cl-Inert (N₂) system. Species that were included in a complex equilibrium analysis of subsystem in the Ga-Cl-Inert system are listed in Table 3-1. For Ga containing gas species, Ga, Ga₂, GaCl, GaCl₂, Ga₂Cl₂, Ga₂Cl₄, Ga₂Cl₆, and GaCl₃ were considered. For gas phase of Cl species, Cl and Cl₂ were considered. The condensed phases were liquid and solid phases of GaCl₃ and Ga. Most data for well-identified species in the Ga-Cl system were obtained from the Thermo-Calc SUB94 database. They have passed the self consistency test as well as 2nd and 3rd law verifications with experimental data.

The base conditions of molar flow rates in the source zone for GaN growth by ALD were as follows. Temperature was varied through the range 300 to 1500 K. The inlet mole fraction of Ga is set to 0.025, Cl for 0.075, and He for 0.900. He ambient gas was used instead of N₂ ambient gas to eliminate the formation of GaN during the calculation although N₂ carrier gas was employed in this study. An inert species in the gas phase primarily contributes to the system entropy.

Figure 3-4A shows the calculated equilibrium mole fractions of gas phase species in the Ga-Cl-Inert system as a function of growth zone temperature. The Cl/Ga atomic ratio was fixed to 3 and the temperature was varied in the range 300 to 1500 K. Mole fraction of gas was kept to 1 in overall temperature range. Thus, there was no condensed phase evident from the calculation

under this condition. A single Ga containing gas species in the growth zone was predicted to exist in the gas phase over most of temperature. GaCl_3 presents predominantly in the gas phase over most of temperature. Figure 3-4B shows the ratio of GaCl_3 to Ga_2Cl_6 increases as temperature increases. From this result, the presence of GaCl_3 becomes more dominant at higher temperature. It is most often desirable to operate under condition where self-limiting adsorption occupies all surface sites. Thus, GaCl_3 would be more suitable than Ga_2Cl_6 . Then, the higher growth temperature is preferred.

Table 3-1. Considered species in Ga-Cl system. Taken from Sub94 database.

Ga containing species (Gas phase)	Ga, Ga ₂ , GaCl, GaCl ₂ , Ga ₂ Cl ₂ , Ga ₂ Cl ₄ , Ga ₂ Cl ₆ , GaCl ₃
Cl species (Gas phase)	Cl, Cl ₂
Condensed phase	GaCl ₃ (l), Ga(l), GaCl ₃ (s), Ga(s)

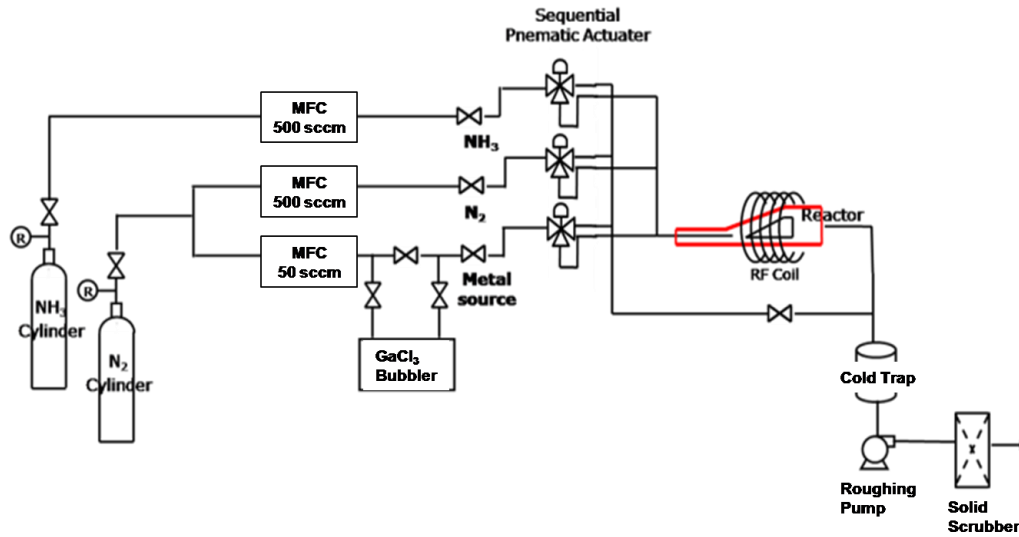


Figure 3-1. Schematic of overall GaN ALD system.

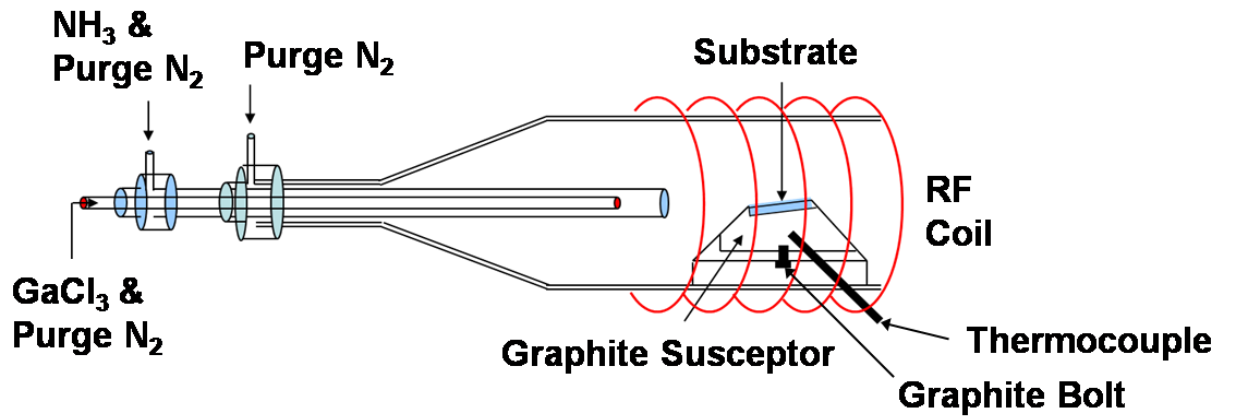


Figure 3-2. Schematic of GaN ALD reactor chamber.

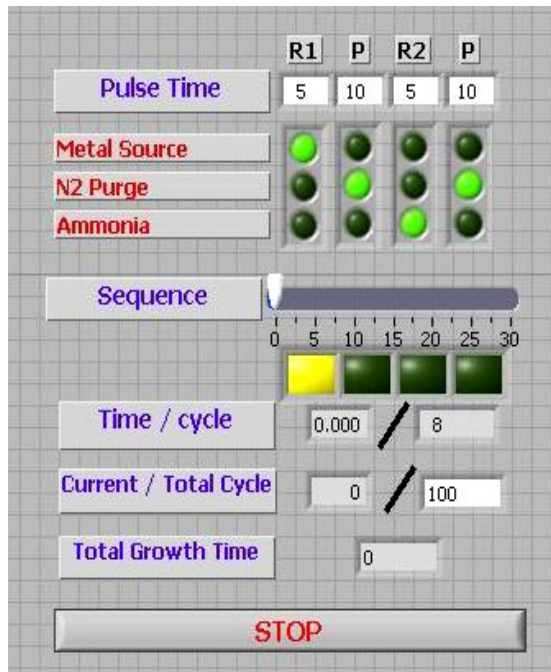


Figure 3-3. Control program of GaN ALD process.

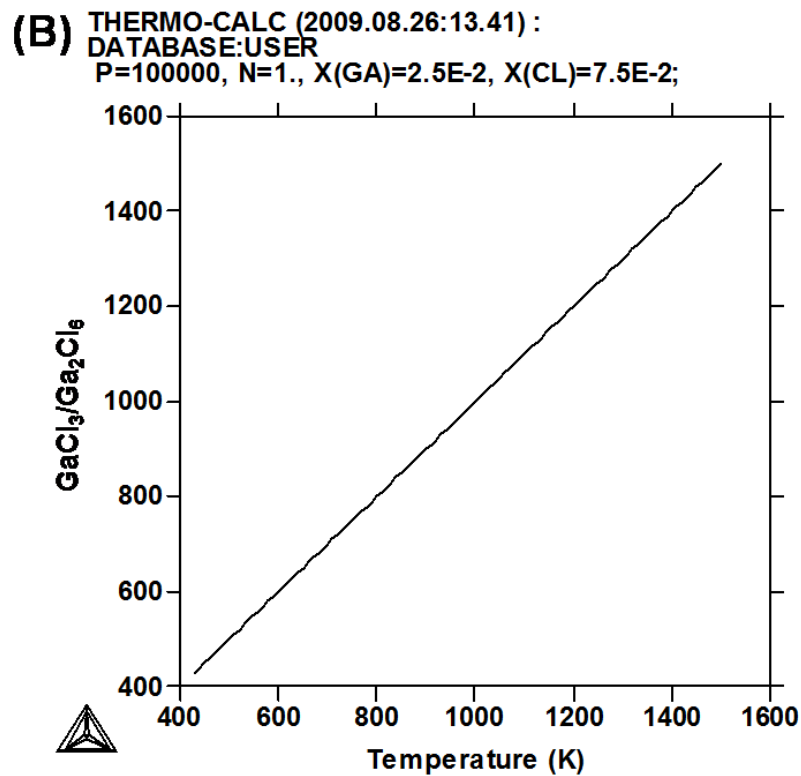
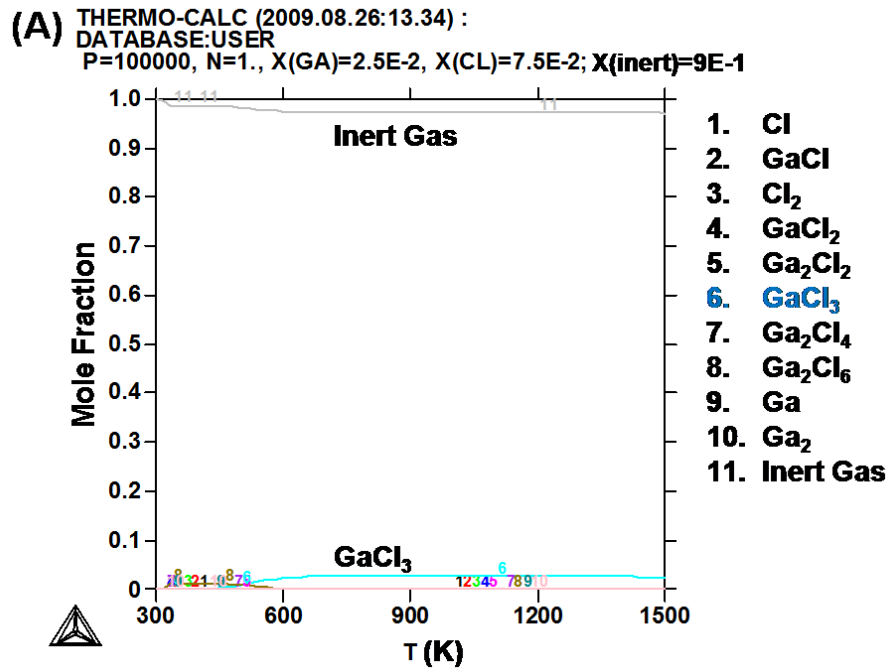


Figure 3-4. (A) Equilibrium mole fractions of gas species in the Ga-Cl-Inert system as a function of temperature at P=1 atm. (B) Molar ratio of GaCl₃ to Ga₂Cl₆ in the Ga-Cl-Inert system as a function of temperature at P=1 atm.

CHAPTER 4
ATOMIC LAYER DEPOSITION OF GaN USING GaCl₃ and NH₃

4.1 Introduction

The group III nitrides have found wide application in both electronic and optoelectronic devices. In particular, solid solutions of the direct band-gap nitrides can access the entire visible range of the spectrum as well as the near UV [113]. Furthermore, the relatively high thermal stability of GaN and AlN has made these nitrides useful in power electronics. Sapphire is commonly used as substrate for growth of GaN, but the low cost, high crystalline quality, and large area of Si make it an attractive substrate choice. In practice, the nitrides are typically deposited by metal organic chemical vapor deposition (MOCVD), and for GaN layers, a deposition temperature in the range 900 to 1100 °C is needed to produce device quality material. Although the rate of NH₃ cracking is greater at higher temperature, the nitrogen partial pressure in equilibrium with the compound is also higher, which leads to a high concentration of nitrogen vacancies in the GaN film. This higher vacancy concentration is reported to be the reason for the high background-carrier concentration in MOCVD grown GaN [114]. Thus, a lower growth temperature is preferred to reduce the background-carrier concentration [57].

In contrast, the thermal stability of InN is considerably less than that of GaN and AlN, and thus growth is typically limited to a temperature below 800 °C. Also, a lower growth temperature is preferred for growth of In_xGa_{1-x}N. Lowering the growth temperature in MOCVD, however, does present difficulties. At lower growth temperature the surface mobility of adsorbed species is reduced, which produces films with poorer structural quality and hence optical properties. As example, it has been reported that In_xGa_{1-x}N grown at 500 °C shows ~1000 times weaker photoluminescence than material grown at 800 °C [115]. Another issue at lower growth temperature is a decreased extent of NH₃ thermal decomposition. Thus both poor

mobility of surface species and the low availability of reactive nitrogen make growth at low temperature challenging.

Atomic layer deposition (ALD) is a potential solution to these growth issues. Since sequential delivery of the reactants in a self-limiting adsorption mode affords increased residence time, both the extent of species surface transport and chemical reaction are increased. This allows for improved structural quality as well as increased levels of reactive nitrogen. Thus ALD films of acceptable quality can often be grown at lower temperature than by CVD. As example, ALD growth of device quality GaAs, GaP, and InGaP has been demonstrated at a temperature as low as ~ 200 °C [116]. Of course, ALD gives control of the film thickness at the atomic layer and shows improved reproducibility of alloy composition [117]. Potential drawbacks of ALD are the lower growth rate and the fact that impurities can more effectively compete for adsorption sites, and thus increase background concentration of impurities.

Unfortunately, very little work has been reported on ALD of GaN. Early studies of ALD growth of GaN used a Ga metal-organic source (trimethylgallium (TMG) and triethylgallium (TEG)) and NH_3 [37, 57, 118]. Films were grown on sapphire or AlN, and a region of self-limiting adsorption was shown with Ga source exposure time. The growth temperature window, however, was not investigated in these studies. The relatively unstable MO sources show a narrow process temperature window for most materials. To resolve this issue, Ga chloride sources (GaCl and GaCl_3) have been used with NH_3 in ALD growth mode on GaAs or GaN/GaAs [59, 119]. In these studies the self-limiting adsorption region was evident with GaCl exposure time, and a temperature window was found when using GaCl . Films showed either hexagonal or cubic GaN(0002) preferred orientation. The self-limiting adsorption windows, however, were not established for use of GaCl_3 . Also, Cl incorporation in the film, which is

deleterious to device performance, was not considered. This study conclusively demonstrates ALD of GaN on Si(100) for the first time using GaCl₃ and NH₃ sources. It is suggested that GaCl₃ is a superior source because of its thermal stability in an H₂-free adsorption step, which increases the width of the temperature window. GaCl₃ is also sufficiently volatile (1 mm Hg at 48 °C) to allow easy delivery. The microstructure, Cl content, and chemical bonding states were examined for films grown within the ALD process window.

4.2 Experimental Procedures

In this study, one ALD cycle consisted of four steps of sequential gas supplies: (1) GaCl₃/N₂ carrier, (2) N₂ purge, (3) NH₃/N₂ carrier, and (4) N₂ purge. The ALD growth mechanism of GaN using GaCl₃ and NH₃ is anticipated to be similar to that of TiN using TiCl₄ and NH₃ [117]. During the first step, input GaCl₃ adsorbs on the surface active sites to form GaCl_x ($x < 3$). Any remaining GaCl₃ or physisorbed by-products are purged from the reactor in the second step. Next NH₃ reacts with adsorbed GaCl_x to form chemisorbed GaNH_{3-x} and x HCl as a physisorbed by-product. The remaining NH₃ and physisorbed HCl are finally purged upon exposure to the N₂ carrier in the last step.

ALD of GaN on Si(100) was performed in a custom horizontal quartz reactor equipped with a load-lock system as described in Chapter 3. Pneumatically actuated valves, controlled with a LabVIEW-based algorithm were sequenced to deliver each reactant and purge gas to the reactor or bypass line. The Si(100) surface was degreased (trichloroethylene, acetone, and methanol), followed by a buffered oxide etch (2 min). GaCl₃ (99.999%, Sigma Aldrich) was contained in a bubbler maintained at 70 °C and delivered to the reactor in N₂ (99.999%, Praxair) carrier gas. NH₃ (99.9999%, Matheson Tri-Gas) was used as the reactive nitrogen source and N₂ as the purge gas. GaN films were deposited in the temperature range 375 to 750 °C at a nominal

growth pressure of 1 Torr. One ALD cycle consisted of sequential GaCl₃ supply (50 sccm N₂), N₂ purge (30 s, 500 sccm), NH₃ supply (500 sccm), and N₂ purge (30 s, 500 sccm).

The film thickness was measured by cross-sectional scanning electron microscopy (SEM) and X-ray reflectometry (XRR) using a JEOL JSM-6335F SEM and a Philips MRD X'Pert system, respectively. Grazing incident angle X-ray diffraction (GIXD) using a Philips MRD X'Pert system operating with Cu *K*α radiation (40kV and 40mA) was used to characterize the film microstructure. GIXD was performed from 30 to 40° 2θ at 1° tilt. Atomic force microscopy (AFM) (Digital Instruments Dimension 3100) was used to examine the film surface morphology. To investigate chemical bonding states, X-ray photoelectron spectroscopy (XPS) measurements were performed with a PerkinElmer PHI ESCA system. Monochromatic Mg *K*α ionizing radiation (1254 eV) was used with the X-ray source operating at 300 W (15 kV and 20 mA). To remove surface contamination, as-grown films were sputtered with Ar⁺ ions for 10 min prior to XPS measurement.

4.3 Results and Discussion

4.3.1 Confirmation of Self-saturation ALD Growth

To verify that growth occurred in ALD mode, a set of experiments was performed to identify a growth window in temperature and GaCl₃ exposure time that produced self-limiting growth. To this end, a series of films was grown (150 cycles) in which the exposure time was varied in the range 2 to 17 s at a fixed NH₃ exposure time of 10 s and N₂ purge time of 30 s. Figures 4-1 A and B show the growth rate (film thickness per cycle) as a function of GaCl₃ exposure time at growth temperature of 550 and 650 °C, respectively. The results in Fig. 4-1A suggest that the growth rate at 550 °C remains constant at 2.0 +/- 0.4 Å/cycle in the range 4 to 11 s of GaCl₃ exposure time. The measurements at the higher growth temperature, 650 °C, show a similar growth plateau at 2.1 +/- 0.5 Å/cycle, but as expected, a narrower exposure time window

(GaCl₃ exposure time in the range 5 to 9 s) as shown in Fig. 4-1B. The constant thickness/cycle regime versus reactant exposure is a feature of ALD and indicates that GaCl₃ is incorporated by self-limiting adsorption.

The deposition rate in the saturation growth regime was 1.6 to 2.6 Å/cycle. As subsequently presented, the microstructure of ALD-GaN in this process window is a mixture of (0002) and (10 $\bar{1}$ 1) oriented GaN. Thus, the thickness of 1 ML of ALD-GaN is calculated as 5.58 Å. Therefore, the deposition rate in the saturation growth regime is 29 to 47% of 1 ML/cycle. It is commonly reported that the saturation coverage of the metal-containing precursor for most metal nitride ALD reactions is less than a single monolayer [120]. An often cited reason is that steric hindrance of adsorbed metal precursors prevents monolayer coverage [117].

The results in Fig. 4-1 show that the growth rate linearly increases with GaCl₃ exposure time for exposure time greater than the window upper limit. The rate of increase is greater at 550 °C than 650 °C. An increase in growth rate with exposure time is usually ascribed to continued chemisorption beyond the saturation limit at longer time. The lower increase in growth rate at higher temperature suggests that an additional second reaction occurs, which may be desorption of a surface Ga species to more volatile GaCl by the reaction with residual HCl. The results of these experiments also show the commonly observed decrease in growth rate at metal exposure times less than that required for operation in the plateau region and are attributed to insufficient exposure time to reach saturation. It is noted that the rate of change in the growth rate at short exposure time was similar for both growth temperatures.

4.3.2 Process Temperature Window

To further substantiate that growth occurs in ALD mode using this chemistry, a second set of experiments was performed to establish the extent of the temperature range yielding

saturation-limited growth. In these experiments depositions were made at the self-saturation growth condition: GaCl₃ (7 s, 50 sccm), N₂ purge (30 s, 500 sccm), and NH₃ (10 s, 500 sccm) while varying the growth temperature in the range 375 - 750 °C for runs of 150 cycles. As shown in Fig. 4-2, the growth rate increased with increasing growth temperature below 500 °C, but then remained constant (2.1 +/- 0.2 Å/cycle) above this temperature, which is consistent with operating in the ALD process temperature window. Since precursor adsorption onto a surface active site and reaction between adsorbed precursor and surface species are thermally activated processes, the growth temperature is expected to be an important factor [117]. At temperature below the window limit, there is insufficient thermal energy available to promote chemisorption at full coverage in the available exposure time. Within the ALD growth temperature window, there is sufficient thermal energy to reach the saturation condition but insufficient for additional reactions to occur (e.g., precursor decomposition and desorption) that preclude saturation. An important feature of using a metal halide precursor is its high thermal stability, and thus the growth rate remains constant even at a relatively high growth temperature. It is noted that GaCl₃ does not react with N₂ in the temperature range of this study and also will not disproportionate since there is no reducing species available (e.g., H₂). Thus this Ga source seems well suited for ALD growth of GaN.

4.3.3 Growth Characteristic of GaN ALD

Since the first layer to deposit requires adsorption on a Si or SiO_x/Si surface, its growth characteristics are expected to be different from those layers subsequently grown on the GaN surface. Furthermore, GaN is not well lattice matched to Si so that residual strain may persist for additional layers to further modify the growth characteristics of layers in the near Si/GaN interfacial region. Kinetic modeling and experimental results during the initial stages and the following stabilized stage have been reported [121-123]. To better understand the early stages of

growth, a series of films was grown at identical conditions except with variable cycle number. The dependency of film thickness on the number of cycles was then examined by XRR. The ALD growth conditions were GaCl₃ exposure time of 7 s at 650 °C with the other steps at the base conditions, while the cycle number was varied in the range 5 to 200.

The results are shown in Fig. 4-3 and indicate that the growth rate of ALD-GaN gradually increased toward a constant value of 2.1 Å/cycle below 15 cycles, and this transition period is termed the transient stage. The growth rate becomes constant (2.1 +/- 0.2 Å/cycle) above 15 cycles, exhibiting a linear dependency of film thickness on the cycle number. This is expected to occur because the adsorption characteristics of GaCl₃ on bare Si or SiO_x/Si are different than those on N terminated GaN. During the first few cycles, self-limiting adsorption likely does not occur. However, once the surface is fully covered and presumably a few layers thick, relaxed GaN becomes the growth surface, which allows self-limiting adsorption at this specific growth temperature.

During the transient stage, it is possible that the adsorption of reactants and preferential growth on as-deposited film compete, leading to three dimensional (3D) growth. For example, studies on ALD of high- κ materials have reported 3D growth during the transient stage [124]. To probe this possibility for ALD-GaN, AFM images of the surface of films deposited in the transient stage were taken. Figure 4-4 depicts the surface morphology of ALD-GaN films grown for 5, 10, and 15 cycles. Figures 4-4 A and B show that the surface roughness, R_q (root-mean-square roughness) is relatively high for films grown with 5 and 10 cycles ($R_q=0.84$ nm for 5 cycles, $R_q=0.72$ nm for 10 cycles), consistent with 3D growth. The surface of the sample grown for 15 cycles (Fig. 4-4 C), however, is substantially smoother ($R_q=0.55$ nm). Note that the linear region begins at 15 cycles and is considered the point at which complete coverage of GaN on Si

substrate is obtained. This conclusion is supported by noting that the surface roughness of the sample grown for 150 cycles (Fig. 4-4 D) is close to that of 15 cycles. ($R_q=0.58$ nm)

4.3.4 Film Microstructure

Given the differences in reaction time and delivery sequence, differences in microstructure between ALD and CVD films might be expected. To explore this possibility, GIXD patterns of GaN film deposited in ALD mode were compared to those deposited outside the ALD process window at higher deposition rate and those deposited in CVD mode. GIXD patterns for ALD GaN films in Fig. 4-5 A reveals the change in the crystalline orientation for two different GaCl_3 exposure times. The lower GIXD pattern in Fig. 4-5 A shows the result for the film grown in ALD mode with GaCl_3 exposure time of 7 s, while the upper GIXD pattern shows the result for a film grown in CVD-like mode using an exposure time of 25 s. The GIXD patterns of both films indicate that their diffraction patterns are well matched with $h\text{-GaN}(0002)$ and $h\text{-GaN}(10\bar{1}1)$ planes, peak positions of 34.633° and 36.994° 2θ , respectively (JCPDS 02-1078). It is observed, however, that the $h\text{-GaN}(10\bar{1}1)$ and $h\text{-GaN}(0002)$ peak intensities are similar for ALD film, while the $h\text{-GaN}(0002)$ peak is dominant for the CVD-like film. The dominance of the $h\text{-GaN}(0002)$ peak becomes more significant in the GIXD pattern of films grown in full CVD mode (Fig. 4-5B). The significant presence of the $h\text{-GaN}(10\bar{1}1)$ reflection in the self-saturation region is believed to be a result of the lower growth rate. As shown in Fig. 4-1, the growth rate of the ALD film is $\sim 1/3$ of that grown in the CVD-like region. When the growth rate is low, the step spacing is small and the growth mode is two dimensional (2D) step-flow. The tendency for 2D step-flow growth is stronger for strained films as is the case here. In 2D step-flow growth mode, the lateral growth orientation is preferred with the suppression of 3D growth. [125] Thus, the formation of the $(10\bar{1}1)$ plane is found in ALD films. As shown in Fig. 4-6, comparison of

the surface morphologies of ALD and CVD is consistent with ALD-GaN growth in 2D step-flow mode and CVD-GaN in 3D growth mode.

4.3.5 Chemical Bonding State

It is of interest to examine the composition of the film as well as the bonding states of the elements. XPS was used to determine the bonding states for a set of films grown in ALD mode as well as in the undersaturated and CVD-like regimes. Films were prepared using GaCl₃ exposure times in the range 2 to 25 s and at base conditions for the other flow rates and exposure times at 650 °C and 1 Torr.

Figure 4-7 shows the evolution of XPS spectra for Ga 2*p*, N 1*s*, O 1*s*, and Cl 2*p* with varying GaCl₃ exposure time. Figure 4-7A shows the Ga 2*p* spectra, which were deconvoluted using a Gaussian-Lorentzian function with background subtraction. The major Ga 2*p* peak is at a binding energy (BE) of 1117.9 eV, which is close to the reported value for GaN [126]. The Ga 2*p* spectra differ by the presence of a low energy shoulder, which has a BE of 1116.9 eV that is attributed to Ga₂O₃. For GaCl₃ exposure times shorter than the minimum one for self-saturation (<9 s), the presence of Ga₂O₃ in the film is evident from the Ga 2*p* peak at the lower BE of 1116.9 eV, which shows a maximum area of 15%. As GaCl₃ exposure time increases, the Ga 2*p* BE shifted from lower BE (mixture of Ga₂O₃ and GaN) to higher BE (GaN only). The presence of Ga₂O₃ in the film in the self-saturation region is in agreement with the O 1*s* spectra (Fig. 4-7C), showing a BE of 530.8 eV, which corresponds to Ga₂O₃. As GaCl₃ exposure time increases, the O 1*s* peak intensity decreases and becomes negligible at 25 s of GaCl₃ exposure time.

The results represented in these Ga 2*p* and O 1*s* spectra suggest that the Ga₂O₃ is present in film grown in the ALD self-saturation region, but disappears for films deposited in the CVD-like

region. This trend is opposite that for the Cl. Figure 4-7D shows the XPS spectra of Cl 2*p*, which increases with GaCl₃ exposure time. For GaCl₃ exposure times to 9 s (self-saturation region), the Cl content is below the detection limit of XPS measurement (~1 at. %). As the GaCl₃ exposure time increases, the Cl 2*p* peak intensity increases to an estimated 1.1 at. % for the 25 s GaCl₃ exposure time. As previously mentioned, it is reported that the oligomer (Cl₂GaNH₂)_{*n*} with *n*=1-3 is generated from gas phase reaction of GaCl₃ and NH₃ at 650 °C [127]. It is possible that this adduct forms at long exposure times from the reaction of the NH₃ with a small amount of residual GaCl₃ remaining in the reactor (e.g., adsorbed on the wall). Thus a small amount of the oligomer adsorbs on the surface and is not fully eliminated by the ammonia flow. To test this possibility, a full CVD film was grown, i.e., all reactants flowing simultaneously. Since the oligomer should be produced under these conditions, high levels of Cl should be evident in the CVD film. The full CVD XPS results shown in Fig. 4-7D indicate relatively high Cl content (1.6 at. %) consistent with the long GaCl₃ exposure time result. It is known that Cl incorporation can lead to bandgap narrowing and contact material corrosion in optoelectronic semiconductors [128]. Thus, it is necessary to minimize Cl contamination. It has been shown that Cl levels can be lowered by including H₂ in the purge steps [129, 130]. The observed Cl contamination, however, is significant only if the GaCl₃ exposure time was longer than self-saturation limit (above ~10 s), presumably as a result of adduct formation between GaCl₃ and NH₃ in the gas phase and on the surface. Thus, as long as GaCl₃ is below the self-saturation limit, the Cl impurity is negligible within the limits of detection by XPS (~1 at. %) as shown in Fig. 4-7.

4.4 Conclusions

ALD of GaN was demonstrated on Si(100) using GaCl₃ and NH₃. The growth rate of GaN film was observed to be constant at 2.0 to 2.1 +/- 0.5 Å/cycle (29 to 47% of 1 ML of *h*-

GaN/cycle) in the ALD self-saturation limit. The ALD process window was found for GaCl₃ exposure time to be between 4 and 11 s at T_{growth}=550 °C, and 5 and 9 s at T_{growth}=650 °C. The high stability of GaCl₃ yielded a relatively wide ALD temperature window in the range 500 to at least 750 °C for the specific switching schedule examined. The GIXD results indicated that ALD film contained two different orientations, GaN(10 $\bar{1}$ 1) and GaN(0002), in contrast to only GaN (0002) for a CVD-like film. For most device applications, this is not acceptable and thus Si surface pretreatments for buffer layers should be explored to permit single crystal growth. The XPS results showed that ALD-GaN films contained Ga₂O₃ than CVD-GaN films. The Cl content correlated inversely with the oxygen level. When GaCl₃ exposure time is less than that required to give self-saturation growth, films were chlorine free. Films deposited in CVD-like region showed 1.1 at. % Cl as did full CVD films.

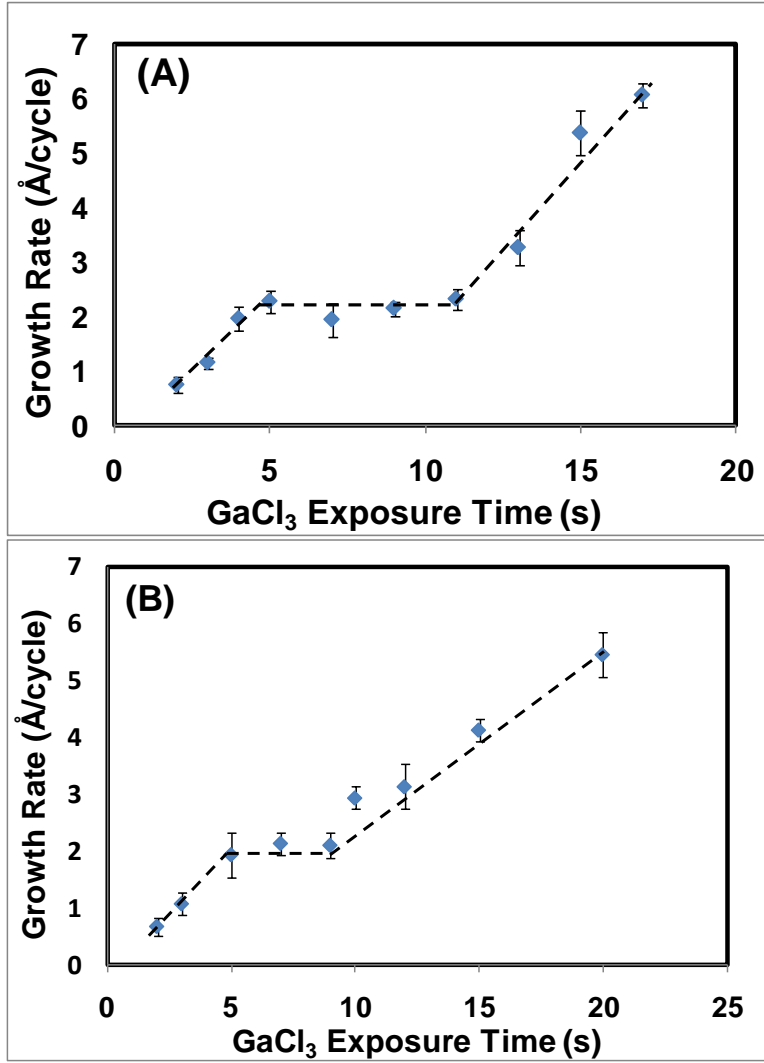


Figure 4-1. Dependence of ALD GaN growth rate on GaCl₃ exposure time. A) T_{growth} = 550 °C. B) T_{growth} = 650 °C. These films are grown on Si(100) with NH₃ exposure time of 10 s.

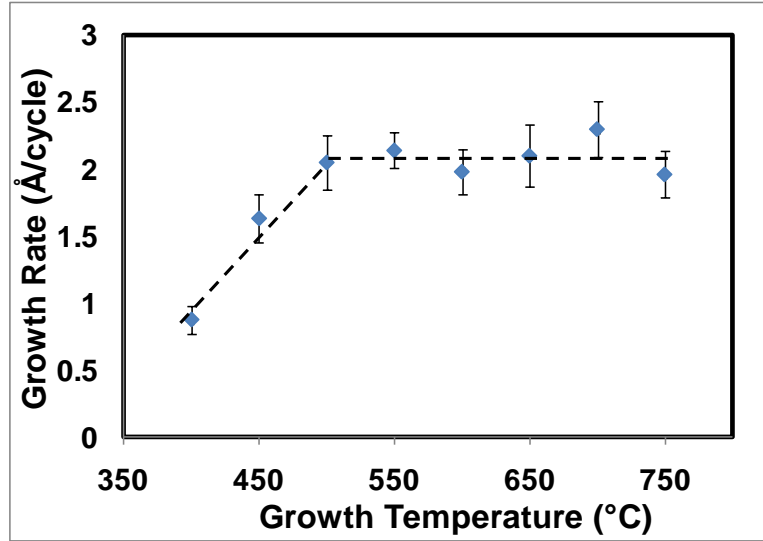


Figure 4-2. Dependence of the growth rate on temperature. Exposure times were set as GaCl₃ = 7 s, NH₃ = 10 s, and N₂ purge = 30 s.

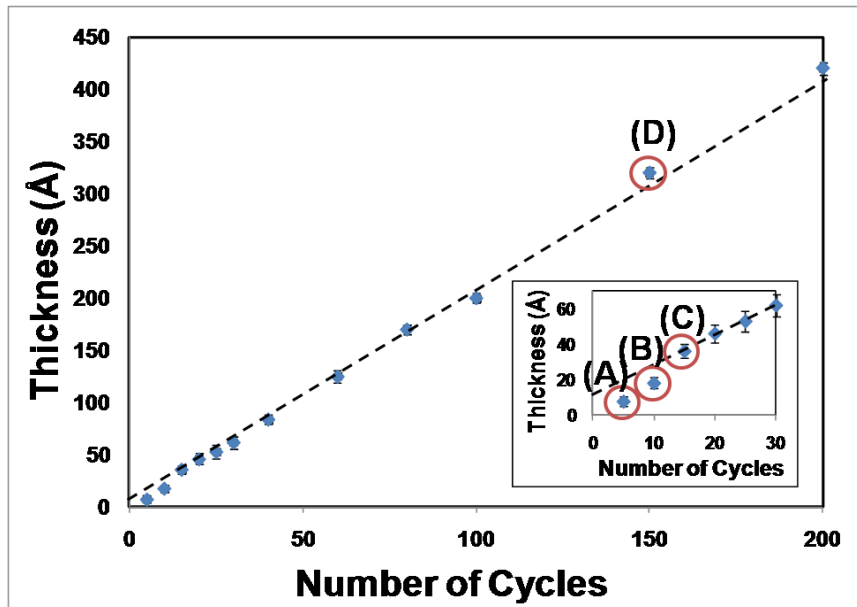


Figure 4-3. Dependence of film thickness (XRR) on cycle number. Growth conditions were set as GaCl₃ exposure time = 9 s, NH₃ exposure time = 10 s, and N₂ purge time = 30 s at T_{growth} = 650 °C. A) 5 cycles. B) 10 cycles. C) 15 cycles. D) 150 cycles.

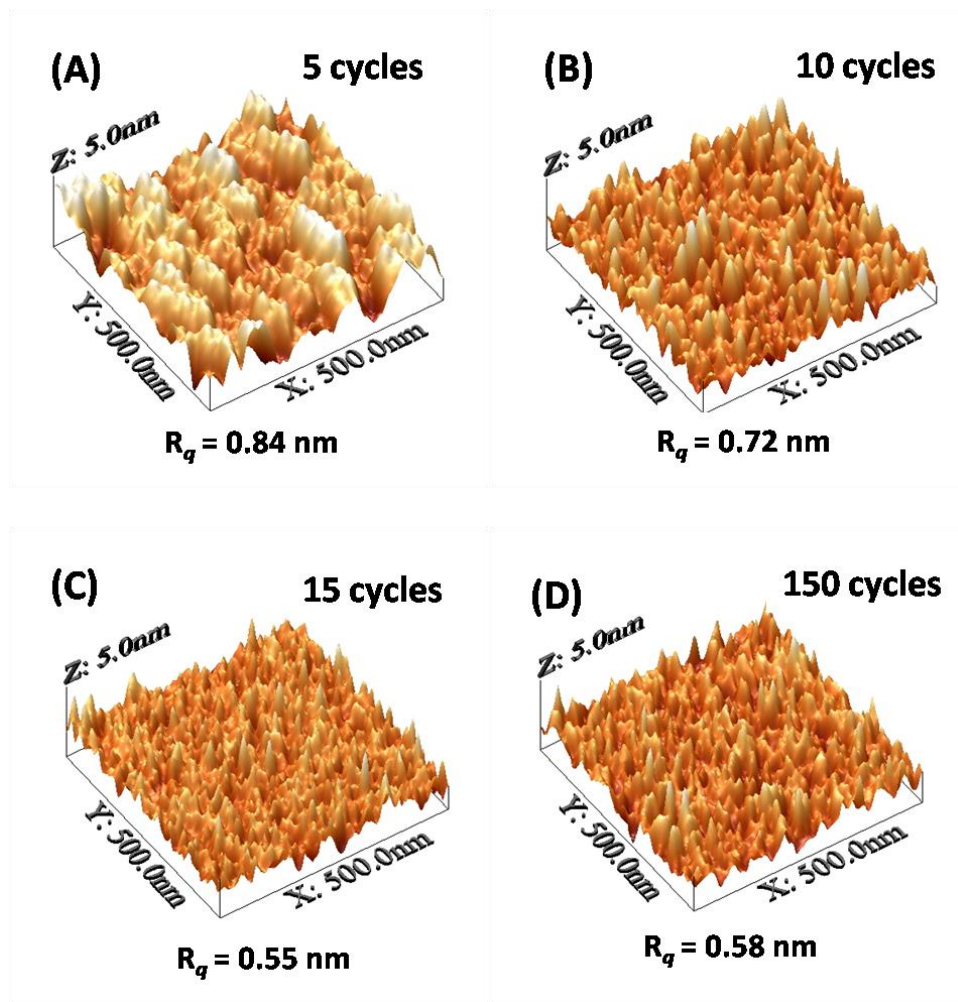


Figure 4-4. Surface morphology of the GaN films deposited with 9 s of GaCl₃ exposure time at 650 °C. A) 5 cycles. B) 10 cycles. C) 15 cycles. D) 150 cycles.

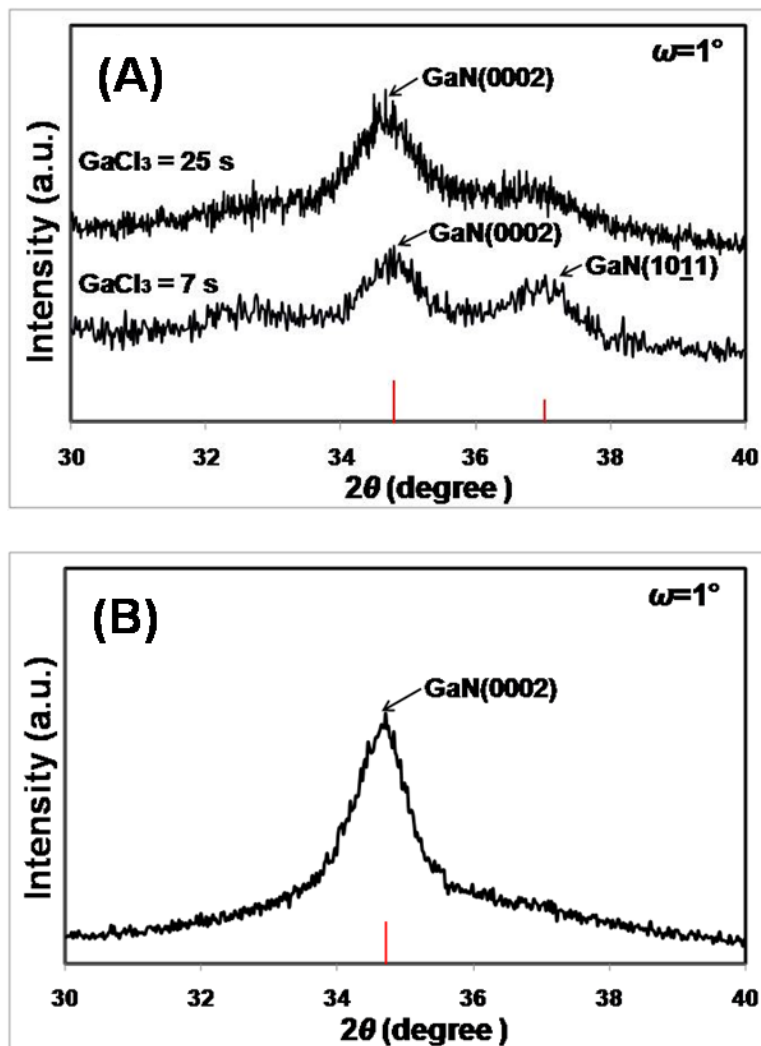


Figure 4-5. GIXD patterns for GaN films grown on Si(100) at 650 °C. A) ALD-GaN films. B) CVD-GaN films.

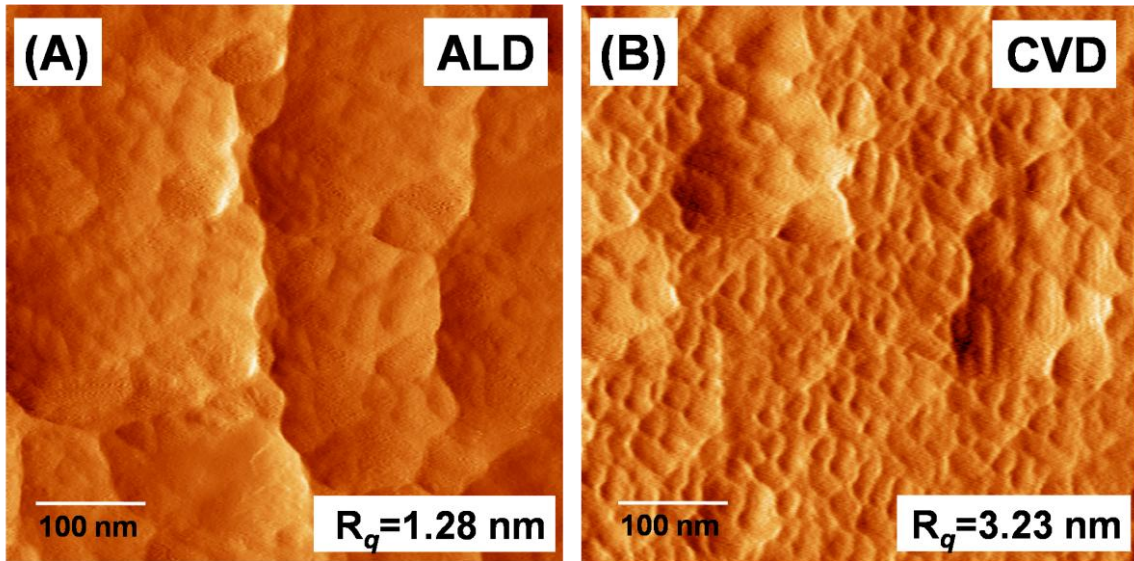


Figure 4-6. Surface morphology of the 60 nm-thick GaN films deposited at 650 °C under A) ALD growth condition B) CVD growth condition.

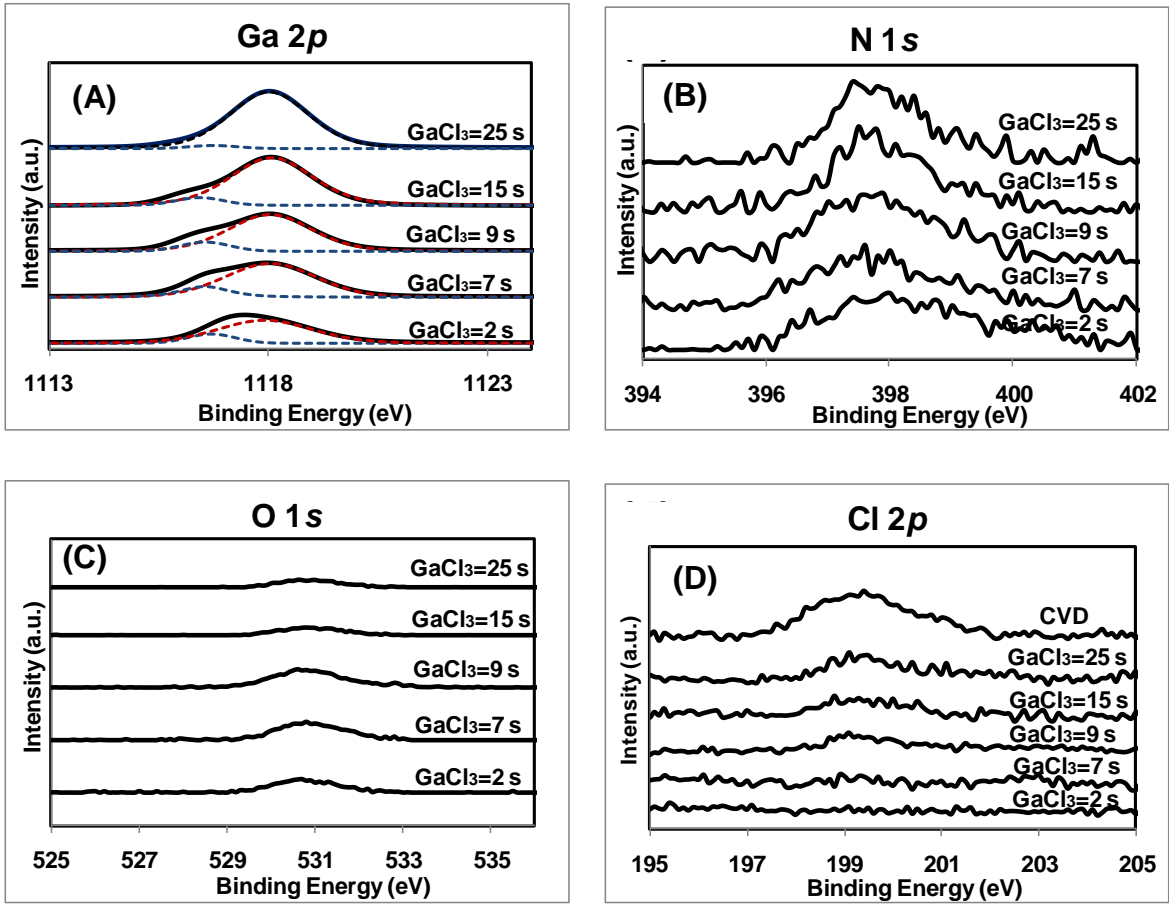


Figure 4-7. XPS spectra of GaN film grown by ALD at various GaCl_3 exposure times. A) gallium $2p$. B) nitrogen $1s$. C) oxygen $1s$. D) chlorine $2p$.

CHAPTER 5
COMPUTATIONAL STUDY FOR ATOMIC LAYER DEPOSITION OF GaN USING GaCl₃
AND NH₃

5.1 Introduction

GaN has gained of a considerable interest to its potential applications to optoelectronic devices operating in the visible and near UV ranges of the spectrum [113]. Metalorganic chemical vapor deposition (MOCVD), hydride vapor phase epitaxy (HVPE), and molecular beam epitaxy (MBE) are typical techniques used for deposition of GaN [31, 131, 132]. In these deposition techniques, a high growth temperature generally in the range of 900 to 1100 °C is necessary to obtain device quality material. At high temperature, however, the nitrogen vacancy concentration increases, which is known to increase the background-carrier concentration [114]. Thus, a lower growth temperature is desired to decrease the background-carrier concentration. However, the structural quality is generally poorer. ALD is a promising deposition technique to address this growth issue. The self-limiting nature of the surface reaction in ALD leads to increased surface reaction residence time to increase surface transport and chemical reaction [133]. This improves the structural quality of ALD films, and allows lower growth temperature, and typically required to obtain acceptable quality [117].

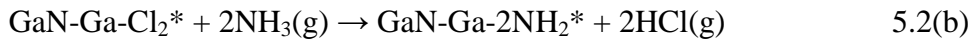
The previous chapter reported the growth of GaN thin films at low temperature by ALD using GaCl₃ and NH₃ [134]. It was known that in the self-saturation limit, Cl-free GaN was grown in the temperature range 550 to 650 °C. Unlike Cl-free ALD-GaN film, relatively high Cl content (1.6 at. %) was obtained in the CVD film, i.e., all reactants flowing simultaneously. The reason for higher Cl incorporation in the CVD-GaN film was suggested by the formation of the oligomer (Cl₂GaNH₂)_n with $n=1$ to 3 from gas phase reaction of GaCl₃ and NH₃ [127]. Since GaCl₃ and NH₃ are not directly mixed in ALD, there is no Cl incorporation in the ALD-GaN

film. Cl incorporation in the film can lead to contact material corrosion and bandgap lowering [128]. Thus, it is very important to better understand Cl incorporation in ALD-GaN film as well as high Cl levels in CVD-GaN film.

This study aims to establish fundamental description of self-limiting surface reactions during ALD processes and to provide insight into Cl incorporation in the film. Atomistic mechanisms were investigated for the reactions of GaCl₃ and NH₃ with appropriate surface active sites. The associated thermochemistry was also studied to estimate the energy barrier along reaction pathways.

5.2 Computational Details

Surface reactions in ALD of GaN using GaCl₃ and NH₃ were described into two half-reactions: the reaction between GaCl₃ and the growing surface during the GaCl₃ supply step, and the reaction between NH₃ and growing surface during the NH₃ supply step. The growing surface was treated as ending with the surface active site: -NH₂ at the initiation of the GaCl₃ supply step, -Cl at the beginning of the NH₃ supply step. The two half-reactions are described as:



Surface active sites are denoted by asterisks. Reaction 5.1(a) was modeled as a cluster consisting of GaN-Ga-NH₂ as depicted in Fig. 5-1. To reduce the computational budget, the tetrahedron formed by the adsorbed Ga species and growing (GaN)₃ was truncated with H atoms. To simulate the growing surface, atoms other than surface active sites were treated using the freeze option in the calculation.

The B3LYP density functional theory (DFT) method using Gaussian 03 split basis sets was employed for all calculations associated with reaction mechanisms of 5.1(a) and (b) [135, 136]. The LanL2DZ basis set was used for Ga atom, and 6-311G(d) was used for H, N, and Cl [137].

Molecular geometries were optimized by energy minimization to stationary points in the potential energy surface (PES). Transition states were optimized using the Berny algorithm. Natural bonding orbital (NBO) analysis was used to determine the weakest bond for each molecule. Frequency calculations were performed to calculate the zero-point energies and thermal corrections for reactants, intermediates, and products at growth temperature and pressure.

5.3 Results and Discussion

5.3.1 Chemisorption of GaCl₃

The proposed mechanism for the first-half reaction 5.1(a), the chemisorption of GaCl₃(g), is shown in Fig. 5-2 along with reaction energetics (Gibbs energy and enthalpy) at both standard ($T=273$ K, $P=1$ atm) and reported growth conditions ($T_{growth}=923$ K, $P_{growth}=0.013$ atm) [134]. The resulting changes in enthalpy and Gibbs energy at standard and growth condition are summarized in Table 5-1. As shown in Fig. 5-2, GaCl₃(g) is molecularly adsorbed on a Ga-NH₂* surface active site by electron lone-pair donation from a surface NH₂ group to an empty *p*-orbital of a Ga atom in GaCl₃(g) to form the dative bond. The Ga atom in GaCl₃(g) is in an electron-deficient state due to the strong electro-negativity of Cl. The electron-deficient Ga atom in GaCl₃(g) precursor is preferred to accept lone-pair electron from surface NH₂ group, and this makes the dative bond formation easier. The resulting adsorption energy is relatively low as -2.1 kcal/mol, and the Gibbs energy change is +21.8 kcal/mol at the growth condition.

The next step involves the production of physisorbed HCl(a) on the surface resulting from the recombination of Cl atom in GaCl₃(g) precursor with one of H atoms in the surface NH₂ group. The proposed transition state between chemisorbed GaCl₃(a) and physisorbed HCl(a) is shown in Fig. 5-2. The formation of physisorbed HCl(a) is activated with respect to the chemisorbed GaCl₃(g) state with an energy of 3.6 kcal/mol and the Gibbs energy of 9.1 kcal/mol

at the reported growth condition. The Gibbs energy change for the transition state to the chemisorbed $\text{GaCl}_3(\text{a})$ state is almost independent of temperature because those two states are entropically similar due to no gas species involved. The entropy of the physisorbed $\text{HCl}(\text{a})$ state is higher than chemisorbed $\text{GaCl}_3(\text{a})$ and transition state, which explains the Gibbs energy stabilization with increased temperature .

In the final step, the physisorbed $\text{HCl}(\text{a})$ is removed from the surface during the N_2 purge step in ALD process, to yield the Ga-NH-Ga-Cl_2^* surface group and $\text{HCl}(\text{g})$. As shown in Fig. 5-2, The Gibbs energy of desorbed $\text{HCl}(\text{g})$ state is lower than the physisorbed $\text{HCl}(\text{a})$ state since there is an increase of entropy by the formation of gaseous HCl . Thus, the Gibbs energy change is negative and becomes more stable with increasing temperature. After the reaction, the as grown GaN surface is saturated by a monolayer of Ga atoms, and the surface is converted from $-\text{NH}_2$ terminated to $-\text{Cl}$ terminated surface. This $-\text{Cl}$ terminated surface becomes the initial surface for the second half-reaction, 5.1 (b).

The GaCl_3 precursor has a planar structure after geometry optimization as shown in the upper-half part of Fig. 5-2. This implies that one Ga $4s$ and two Ga $4p$ orbitals form $3 sp^2$ hybrid orbitals bonded to $-\text{Cl}$ ligands. After this orbital hybridization, Ga has one empty $4p$ orbital to form the dative bond by lone-pair electron donation from NH_2 surface group. A similar dative bond formation by lone-pair electron donation is reported in the ALD of Al_2O_3 from AlCl_3 and H_2O [138].

If the energy state of the adsorbed $\text{GaCl}_3(\text{a})$ complex is lower than dissociated products, a significant fraction of the precursor molecule will be molecularly trapped in the adsorbed complex resulting in incorporation of Cl atoms in the film. As shown in Fig. 5-2, however, the energy state of $\text{GaCl}_3(\text{a})$ dative-bonded complex is higher than dissociated products (Gibbs

energy difference). Thus, there is a thermodynamic driving force for most of adsorbed precursor molecules to directly dissociate to products instead of molecularly trapped in the adsorbed complex state. This products low Cl incorporation in ALD is consistent with the XPS results given in Chapter 4 [134].

5.3.2 Chemisorption of NH₃

The proposed mechanism of reaction 5.1(b), the chemisorptions of NH₃(g), is schematically shown in Fig. 5-3 with computed reaction energetics. The changes in enthalpy and Gibbs energy are listed in Table 5-2 at standard and growth condition. In this reaction, the Ga-Cl₂* surface species is produced from reaction 5.1(a). The chlorine terminated species is exposed to NH₃(g), molecularly adsorbs on the Ga-Cl₂* surface site by dative bond formation between the N and surface Ga, similar to that in the first-half reaction. The electron lone-pair of N in NH₃(g) precursor is donated to the empty 4*p*-orbital of the Ga atom in chemisorbed species, Ga-Cl₂*. As listed in Table 5-2, the adsorption enthalpy of NH₃ onto a Ga-Cl₂* surface site is -4.2 kcal/mol, and the Gibbs energy change is +14.2 kcal/mol at the growth condition.

The transfer of first H atom in NH₃(a) to a Cl in the Ga-Cl₂* surface group to yield physisorbed HCl(a) is shown in Fig. 5-3 along with the transition state between the NH₃(a) adsorption state and HCl(a) physisorption state. Similar to the energetics of transition state in reaction 5.1(a), the formation of HCl(a) is activated with respect to the chemisorbed NH₃(a) state, showing an activation energy of 3.8 kcal/mol.

The physisorbed HCl(a) is removed from the surface during N₂ purge step, and results in Ga-ClNH₂* surface group and desorbed HCl(g). The Gibbs energy in this step is stabilized at increased temperature due to increased entropy. The remaining Cl atom in Ga-ClNH₂* surface group is to be removed from the surface as HCl(g) by the similar reaction with NH₃(g). After second-half reaction, The Cl terminated Ga surface is now saturated with -NH₂. The resulting

Ga-NH₂* surface is the initial surface for the next cycle of ALD, i.e., GaCl₃(g) precursor exposure. After completion of reactions 5.1(a) and (b), the surface is saturated with a fractioned molecular layer of GaN, and maintains the same surface active site, NH₂*.

As shown in Table 5-2, the enthalpy for the chemisorption of NH₃(g) is -4.2 kcal/mol, which is lower value than the chemisorption of GaCl₃(g). The lower enthalpy for the NH₃ chemisorption leads to the higher probability for surface Cl atom to be desorbed as HCl(g), resulting in lower Cl incorporation in the film. In addition, the stabilized Gibbs energy of HCl(g) desorption state at increased temperature drives lower the Cl incorporation at growth temperature.

5.4 Conclusions

In this study, a detailed atomistic reaction mechanism was proposed for ALD of GaN using GaCl₃ and NH₃. The chemisorption processes of GaCl₃ and NH₃ onto the growing surface were investigated by considering the adsorption and desorption states along with the intermediated transition state. GaCl₃ and NH₃ were molecularly adsorbed on the growing surface by electron lone-pair donation from N to Ga. The surface active sites were converted from -NH₂ terminated to -Cl terminated after GaCl₃ chemisorption, and from -Cl to -NH₂ terminated after NH₃ chemisorption. HCl was the desorbed product in both chemisorptions process. The PES of both chemisorption processes were presented with Gibbs energies at standard and growth condition. The PES of GaCl₃ chemisorption shows no molecular trapping of Cl incorporating adsorbed complex due to the higher energetic level of GaCl₃ adsorption state. This results in lowered Cl incorporation in the growing surface. Furthermore, PES of NH₃ chemisorption exhibits a negative energy barrier (-4.2 kcal/mol). NH₃ chemisorption leads to desorption of Cl atoms from the growing surface as HCl products. Thus, Cl incorporation in the film can be much lowered by

the negative energy barrier for NH_3 chemisorption. These results provide a rationale for Cl-free, ALD, GaN films grown.

Table 5-1. Standard enthalpy at 298 K (ΔH°_{298}) and Gibbs energy difference at 298K, 1 atm (ΔG°_{298}) and 923 K, 0.013 atm ($\Delta G^{\circ}_{923\text{ K}, 0.013\text{ atm}}$) for chemisorption of GaCl₃.

	GaCl₃(a) Chemisorption State	Transition State	HCl(a) Physisorption State	HCl(g) Desorption State
ΔH°_{298} (kcal/mol)	-2.1	+1.9	+1.2	-1.6
ΔG°_{298} (kcal/mol)	+13.2	+19.6	+10.4	-3.5
$\Delta G^{\circ}_{923\text{ K}, 0.013\text{ atm}}$ (kcal/mol)	+21.8	+30.9	+11.3	-8.7

Table 5-2. Standard enthalpy at 298 K (ΔH°_{298}) and Gibbs energy difference at 298K, 1 atm (ΔG°_{298}) and 923 K, 0.013 atm ($\Delta G^{\circ}_{923\text{ K}, 0.013\text{ atm}}$) for chemisorption of NH₃.

	NH₃(a) Chemisorption State	Transition State	HCl(a) Physisorption State	HCl(g) Desorption State
ΔH°_{298} (kcal/mol)	-4.2	-0.4	-2.0	-6.4
ΔG°_{298} (kcal/mol)	+5.1	+9.6	+3.2	-6.2
$\Delta G^{\circ}_{923\text{ K}, 0.013\text{ atm}}$ (kcal/mol)	+14.2	+21.5	+11.9	-6.3

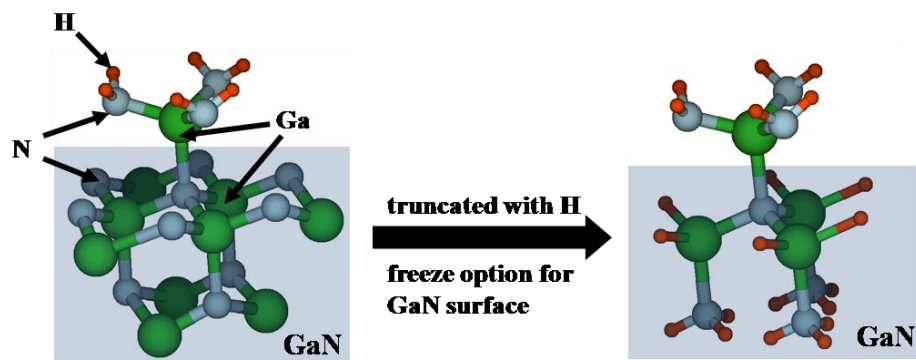


Figure 5-1. Cluster model used in the calculation to represent GaN-GaNH₂* surface.

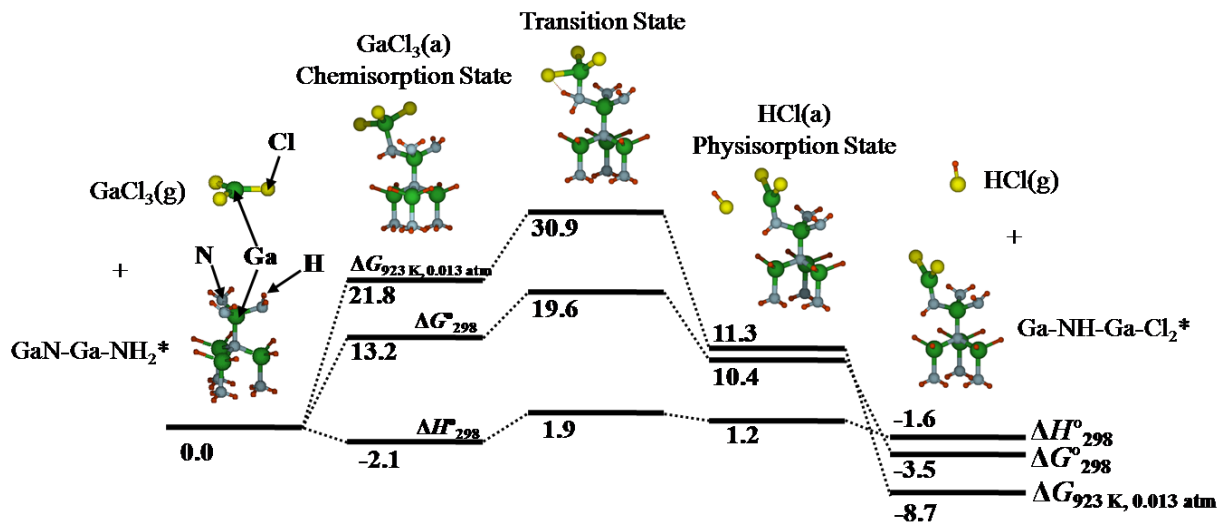


Figure 5-2. PES (ΔH°_{298}) and Gibbs energy surface at 298 K, 1atm (ΔG°_{298}) and 923 K, 0.013 atm ($\Delta G^{\circ}_{923 \text{ K}, 0.013 \text{ atm}}$) for the chemisorption of GaCl₃, representing first-half reaction. The unit is kcal/mol.

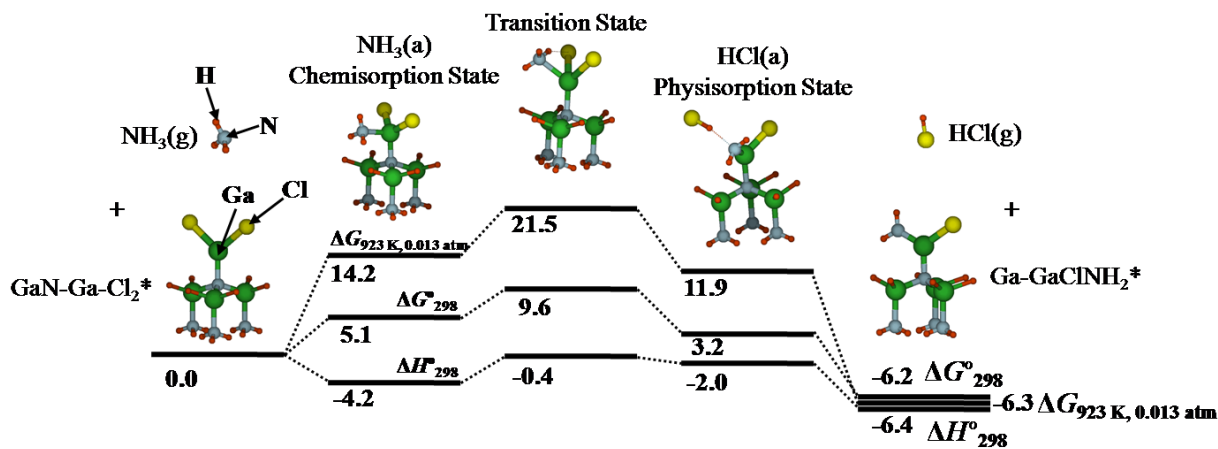


Figure 5-3. PES (ΔH°_{298}) and Gibbs energy surface at 298 K, 1atm (ΔG°_{298}) and 923 K, 0.013 atm ($\Delta G^{\circ}_{923 \text{ K}, 0.013 \text{ atm}}$) for the chemisorption of NH₃, representing second-half reaction. The unit is kcal/mol.

CHAPTER 6
p-TYPE DOPING OF GaN USING Cp₂Mg AS A DOPANT

6.1 Introduction

There has been many efforts to develop group III-nitride based optoelectronic devices for blue light-emitting and laser diode applications over past decades since they cover the wide band gap energy range 2.0 to 6.2 eV at room temperature [113]. One of difficult challenges to develop III-nitride devices was to achieve low-resistivity, *p*-type GaN. To activate dopant, post-growth N₂ ambient annealing or LEEBI treatment was employed [34, 35].

Mg is the most widely used *p*-type dopant by both MOCVD and HVPE. For MOCVD growth, TMG and NH₃ were employed as Ga and N source, respectively. The commonly used Mg precursor in *p*-type doping of GaN for MOCVD is bis-cyclopentadienyl magnesium (Cp₂Mg). MOCVD of Mg-doped GaN is known to be very sensitive to the growth parameters, including TMG and Cp₂Mg flow rates, N/Ga ratio, growth rate, growth pressure, and carrier gas selection. Many groups have reported the optimization of growth parameters to achieve high hole concentration and low resistivity. The best result to date shows a hole concentration as low 10¹⁸ cm⁻³, and the resistivity below 1 Ω-cm [139-142].

HVPE of Mg-doped GaN was performed to reduce C contamination in the film [143]. GaCl and NH₃ were employed as Ga and N source, respectively. Mg was supplied with HCl, and films were grown with AlN buffer layer. The highest measured hole concentration was 1.5 × 10¹⁸ cm⁻³ at the room temperature. The structural quality, however, was not investigated in this study.

In this study, *p*-type GaN was grown using Cp₂Mg as the dopant precursor. HVPE was employed in the growth of Mg-doped GaN. For the first time, GaCl₃ was used as the Ga source with NH₃ for *p*-type GaN HVPE. GaCl₃ allows easy delivery due to its high vapor pressure (1

mm Hg at 48 °C). The structural quality, electrical properties, and optical characteristics were determined on the Mg-doped GaN films grown as a function of Mg source incorporation. The results could be explained by introducing the effect of impurities and compensating .

6.2 Experimental Details

The GaN films were deposited on c-plane sapphire substrates using a custom horizontal HVPE system. Sapphire substrates were degreased by trichloroethylene, acetone, and methanol. GaCl₃ (99.999%, Rohm and Haas) was used as Ga source, contained in a bubbler maintained at 75 °C. Cp₂Mg (99.999%, Epichem) was used as Mg dopant source, contained in a bubbler maintained at 25 °C. These metal precursors were delivered to the reactor by N₂ (99.999%, Airgas South) carrier gas. NH₃ (99.9999%, Matheson Tri-Gas) was used as N source. Sapphire substrates were thermally treated in NH₃ at 750 °C for 30 min before the growth. To initiate epi-growth, thin GaN buffer layer was grown at 550 °C for 5 min. Then, the growth temperature was raised to 700 °C, and 450 nm thick Mg-doped GaN was grown with V/III ratio of 175. The flow rate of GaCl₃ and NH₃ was kept at 50 sccm (sccm denotes cubic centimeters per minute at STP) and 500 sccm, respectively. The flow rate of Cp₂Mg was varied from 5 to 30 sccm, according to the molar flow range 0.1 to 0.6 μmol/min. To activate dopants, post-growth annealing was performed under N₂ at 750 °C for 30 min.

The film thickness was measured by cross-sectional scanning electron microscopy (SEM) using a JEOL JSM-6335F SEM. The microstructure of the film was investigated by double crystal X-ray diffraction (DCXRD) using a Philips MRD X'Pert system. DCXRD was performed with Cu *K*α radiation (40kV and 40mA) to obtain rocking curve of on-axis GaN-(0002) operating. Carrier concentration, mobility, and resistivity of the film were measured by room temperature Hall measurements (van der Pauw method) using Lakeshore 7507. Hall measurement was performed with the sweeping of magnetic field in the range of 10 mG to 10

kG. The optical properties of Mg-doped GaN films were characterized by room temperature photoluminescence (PL) measurement.

6.3 Results and Discussion

6.3.1 Film Microstructure

DCXRD was used to investigate the structure properties of Mg-doped GaN layer. It is known that full width half maximum (FWHM) of the on-axis (0002) rocking curve is related to the screw and mixed-type dislocations [144]. Figure 6-1 shows the FWHM of on-axis rocking curve as a function of Cp₂Mg flow rate for 450 nm Mg-doped GaN film.

The FWHM of undoped 450 nm GaN is 157 arcsec. In general, the FWHM increases as the incorporation of Mg increases. The increase of FWHM is not obvious when the Cp₂Mg flow rate is below 15 sccm. However, the FWHM dramatically increases with the incorporation of Mg when the Cp₂Mg flow rate is above 20 sccm. As mentioned above, the increase of FWHM indicates the increase of the dislocation density. Thus, it is revealed that the dislocation density of Mg-doped GaN film increases with Mg incorporation. The dislocation of Mg-doped GaN is believed to result from the difference of atomic size between Ga and Mg, where the atomic radius of Ga and Mg are 136 and 145 pm, respectively [145].

6.3.2 Film Resistivity

For the film resistivity, film thickness measured from SEM was employed in electrical measurements using van der Pauw method. The ohmic contacts were fabricated using In-Zn alloy, which were annealed at 500 °C for 1 min under N₂ in order to decrease contact resistance of the interface. Resistivities of Mg-doped GaN as a function of Mg incorporation are shown in Fig. 6-2.

The resistivity of undoped GaN film was 890 μΩ-cm. As shown in Fig. 6-2, the resistivity of Mg-doped GaN film increases with the Mg incorporation even though there is a slight

decrease at the Cp_2Mg flow rate of 10 sccm. The high resistivity of highly Mg doped GaN can be explained by H-passivation. It is known that Mg acceptors are passivated by H atoms which generated from decomposed NH_3 and Cp_2Mg during growth [146-148]. Post-annealing was performed to activate Mg acceptors by cracking Mg-H complex. However, the employed annealing condition was not enough to activate Mg acceptor completely. Also, there was another reason of high resistivity which is self-compensation by deep donor. This will be discussed in Chapter 6.3.3.

6.3.3 Hole Properties

Hole concentration and mobility were measured by room temperature Hall measurement using In-Zn alloy electrode. Figure 6-3 shows the hole mobility of Mg-doped GaN film as a function of Mg incorporation.

The hole mobility of undoped GaN was $510 \text{ cm}^3 \text{ V}^{-1} \text{ s}^{-1}$. There was slight increase of the hole mobility up to $1340 \text{ cm}^3 \text{ V}^{-1} \text{ s}^{-1}$ when Cp_2Mg flow rate was 5 sccm. Then, the hole concentration decreases as Cp_2Mg flow rate increases, and dropped down to $4.75 \text{ cm}^3 \text{ V}^{-1} \text{ s}^{-1}$ when Cp_2Mg flow rate was 30 sccm. As shown, Mg-doped GaN has the lower hole mobility than undoped GaN, and gets much lower as increase of Mg doping level. The low-hole mobility in the Mg-doped GaN is not only attributed to the scattering by the neutral or ionized Mg impurities and native defects, but also to the inter-band scattering between heavy-hole and light-hole bands [141]. The mobility limitation effect by these scatterings becomes more severe as Mg incorporation increases since Mg impurities, defects, and heavy-light holes increase with Mg incorporation.

Figure 6-4 shows the hole concentration of Mg-doped GaN film as a function of Mg incorporation. Undoped GaN film showed *n*-type conduction, and the background carrier concentration was $5.1 \times 10^{16} \text{ cm}^{-3}$. The GaN film showed *p*-type conduction with the addition of

Cp₂Mg. The hole concentration increases with Mg incorporation when Cp₂Mg flow rate is below 15 sccm. The maximum hole concentration is $3.2 \times 10^{17} \text{ cm}^{-3}$ at 15 sccm of Cp₂Mg flow rate. When Cp₂Mg flow rate is above 15 sccm, the hole concentration begins to decrease with Mg incorporation, and showed the minimum value of $5.6 \times 10^{16} \text{ cm}^{-3}$ at 30 sccm of Cp₂Mg flow rate.

The resulting low hole concentration at high Mg incorporation indicates the existence of self-compensation caused by the association of Mg_{Ga} acceptor and the nearest-neighbor N vacancy at high Mg doping level. According to the defect energy diagram and first-principle calculation, one of the most dominating defects in highly doped *p*-GaN is N vacancy, V_N [149]. N vacancy exists as V_N³⁺ charge state instead of V_N¹⁺ due to a lower energy of formation and large relaxation by neighboring Ga atoms (moving outward by ~15% of bond length) [150]. This V_N³⁺ is mobile, and tends to associate with oppositely charged Mg_{Ga} acceptors. The association of V_N³⁺ and Mg_{Ga}¹⁻ forms a nearest-neighbor complex, (V_N-Mg_{Ga})²⁺, which is energetically favored than (V_N-Mg_{Ga})⁰ [149]. This (V_N-Mg_{Ga})²⁺ complex acts as compensating donor for Mg_{Ga} acceptor, and the concentrations of V_N³⁺ and (V_N-Mg_{Ga})²⁺ increase at high Mg incorporation. Thus, there is more self-compensation of Mg_{Ga} acceptor by (V_N-Mg_{Ga})²⁺ donor at high Mg incorporation, and this results in low hole concentration at high Mg incorporation. This self-compensation effect is well established for the high gap II-VI compounds [151]. In Ag doped ZnS, the Ag_{Zn} acceptors associate with S vacancies, forming V_S-Ag_{Zn} donor centers. This V_S-Ag_{Zn} donor compensates Ag_{Zn} acceptor, and limits the hole concentration at high Ag incorporation.

6.3.4 Optical Properties

As mentioned, the hole concentration decreases at high Mg incorporation due to the self-compensation of Mg_{Ga} acceptor by (V_N-Mg_{Ga})²⁺ complex donor. To confirm this self-

compensation at high Mg incorporation, PL was performed on samples after carrier activation. PL spectra were calibrated to the excitation peak location. Figure 6-5 shows the room temperature PL spectra of Mg doped GaN films at different levels of Mg incorporation.

For undoped GaN, the near band gap edge emission at 3.41 eV (364 nm) is dominant peak. With the increase of Mg incorporation, emission at 3.12 eV (398 nm) gradually becomes the dominant peak while the emission at 3.41 eV decreases. The peak intensity of the emission at 3.12 eV increases with Mg incorporation, and shows the highest value at 15 sccm of Cp₂Mg flow rate. At higher Mg incorporation, the dominant peak becomes the emission at 2.83 eV (438 nm).

The peak positions for various Mg incorporation levels are attributed to different types of donor-acceptor (D-A) pair recombination. The ionization energy of Mg_{Ga}¹⁻ acceptor is known to be in the range of 0.22 – 0.25 eV [7]. And, the ionization energy of the V_N³⁺ donor, which naturally exists in GaN film, is ~0.03 eV [8]. When Mg is fairly doped in GaN, D-A recombination by Mg_{Ga}¹⁻ acceptor and V_N³⁺ donor or conduction band becomes dominant, leading to E_g shift by 0.22 to 0.28 eV. This E_g shift results in the emission peak in the range 3.13 to 3.19 eV, which is very close to the position of the dominant emission peak at 3.12 eV when Cp₂Mg flow rate is in the range 5 to 15 sccm in Fig. 6-5. Thus, it is stated that D-A recombination by Mg_{Ga} acceptor and V_N donor or conduction band is responsible for the emission at 3.12 eV (398 nm). And, Mg_{Ga} acceptor level is highest when Cp₂Mg flow rate is 15 sccm.

As mentioned previously, (V_N-Mg_{Ga})²⁺ compensating donor tends to be formed by the association of Mg_{Ga} acceptor and the nearest-neighbor V_N in highly Mg-doped GaN. The ionization energy of (V_N-Mg_{Ga})²⁺ donor is reported to be in the range 0.3 to 0.4 eV [152]. And, the ionization energy of Mg_{Ga} acceptor is in the range 0.22 to 0.25 eV. Thus, D-A recombination

by Mg_{Ga} acceptor and $(\text{V}_{\text{N}}-\text{Mg}_{\text{Ga}})^{2+}$ donor leads to E_{g} shift by 0.52 to 0.65 eV. This E_{g} shift results in the emission peak in the range 2.76 to 2.89 eV, which is same as the peak position of dominant emission peak at 2.83 eV for highly Mg-doped GaN in Fig. 6-5. Thus, the emission at 2.83 eV for highly Mg-doped GaN film is attributed to D-A recombination by self-compensation of Mg_{Ga} acceptor with $(\text{V}_{\text{N}}-\text{Mg}_{\text{Ga}})^{2+}$ donor. And, the self-compensation becomes more severe as the increase of Mg incorporation.

In summary, PL spectra exhibit two different types of D-A recombination which are responsible for two different emission peaks (2.83 and 3.12 eV). D-A recombination by Mg_{Ga} acceptor and V_{N} donor or conduction band corresponds to the emission of 3.12 eV. And, D-A recombination by the self-compensation of Mg_{Ga} acceptor with $(\text{V}_{\text{N}}-\text{Mg}_{\text{Ga}})^{2+}$ donor corresponds to the emission of 2.83 eV. The evolution of 3.12 eV emission peaks demonstrates that Mg_{Ga} acceptor level is highest at 15 sccm of Cp_2Mg flow rate. This is well supported by the result of Hall measurement, which shows the highest hole concentration at 15 sccm of Cp_2Mg flow rate. In addition, the appearance of a self-compensation emission peak (2.83 eV) at very high Mg incorporation confirms the formation of $(\text{V}_{\text{N}}-\text{Mg}_{\text{Ga}})^{2+}$ donor in highly Mg-doped GaN. Also, the evolution of self-compensation emission peaks exhibits the more compensation of Mg acceptor in highly Mg-doped GaN. This confirms the result of Hall measurement, which shows the decrease of hole concentration at very high Mg incorporation. Results from PL measurements such as emission types and positions are in good agreements with results from Mg-doped GaN using TMG and Cp_2Mg [140, 145, 153].

6.4 Conclusions

p-type GaN was grown by low pressure HVPE system. GaCl_3 , NH_3 , and Cp_2Mg were employed as Ga, N, and Mg source, respectively. Structural, electrical, and optical properties were investigated with the variation of Mg incorporation. The defect density of Mg-doped GaN

film increased with Mg incorporation due to the large difference of the atomic size between Ga and Mg. Also, the resistivity increased with Mg incorporation due to H-passivation and self-compensation. Scattering effect decreased the while the hole mobility decreased. A maximum hole concentration was $3.2 \times 10^{17} \text{ cm}^{-3}$ at 15 sccm of Cp_2Mg flow rate. The hole concentration decreased in highly Mg-doped GaN due to self-compensation of Mg acceptor. From the results of the room temperature PL, the emission peak at 2.83 eV in highly doped GaN confirmed the self-compensation of Mg acceptor. Also, the evolution of 3.12 eV emission peaks supported the optimum condition for highest hole concentration, which is at 15 sccm of Cp_2Mg flow rate.

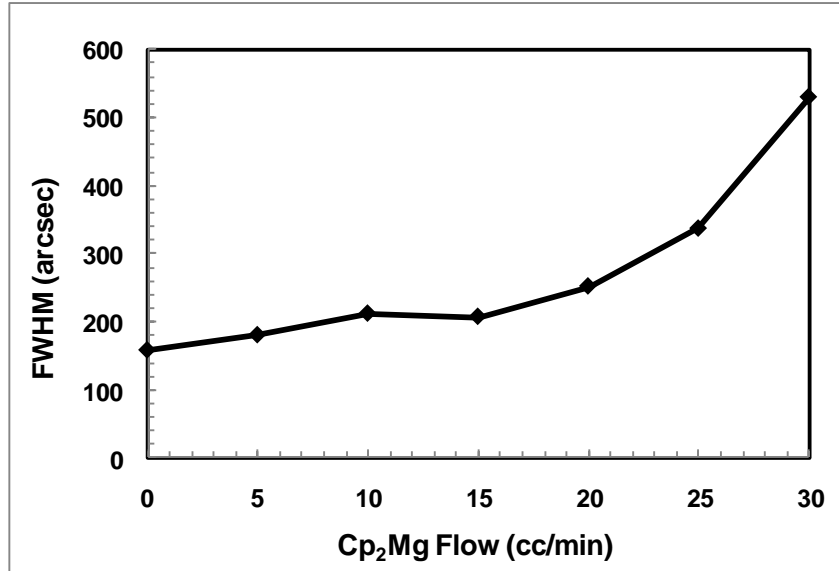


Figure 6-1. Crystallinity of Mg-doped GaN films as a function of Mg incorporation.

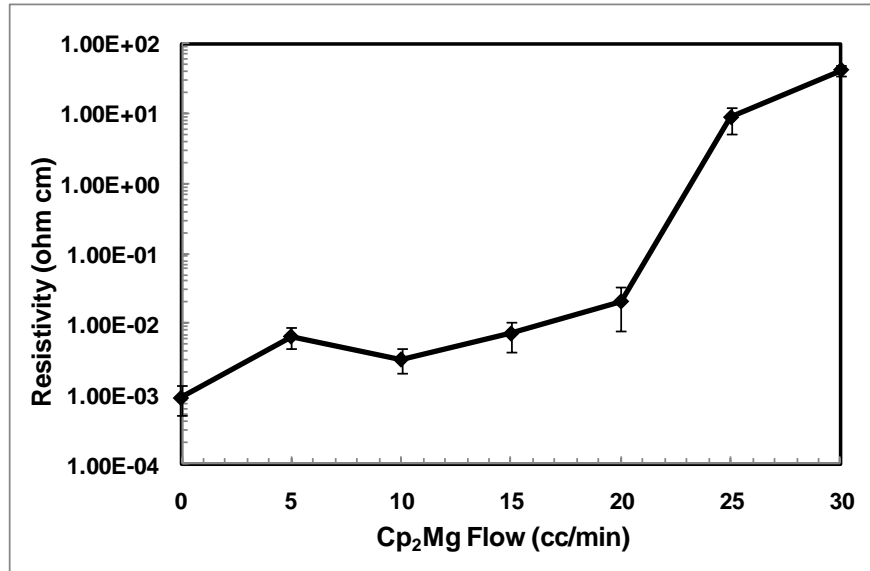


Figure 6-2. Resistivities of Mg-doped GaN films as a function of Mg incorporation.

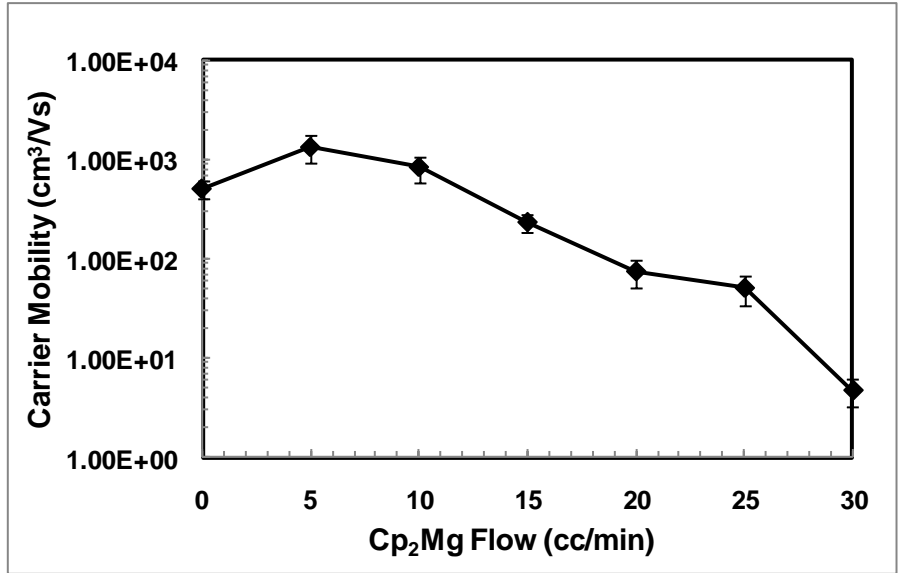


Figure 6-3. Hole mobilities of Mg-doped GaN films as a function of Mg incorporation.

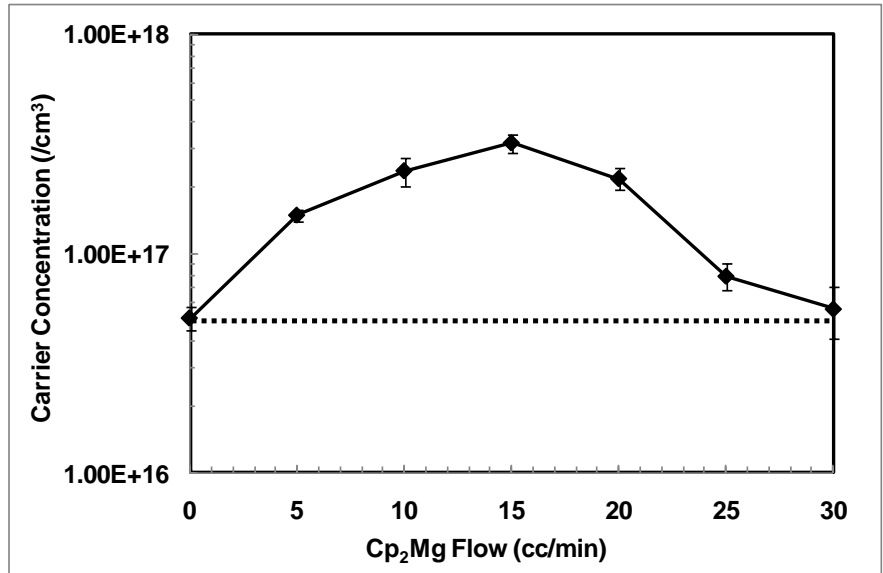


Figure 6-4. Hole concentrations of Mg-doped GaN films as a function of Mg incorporation.

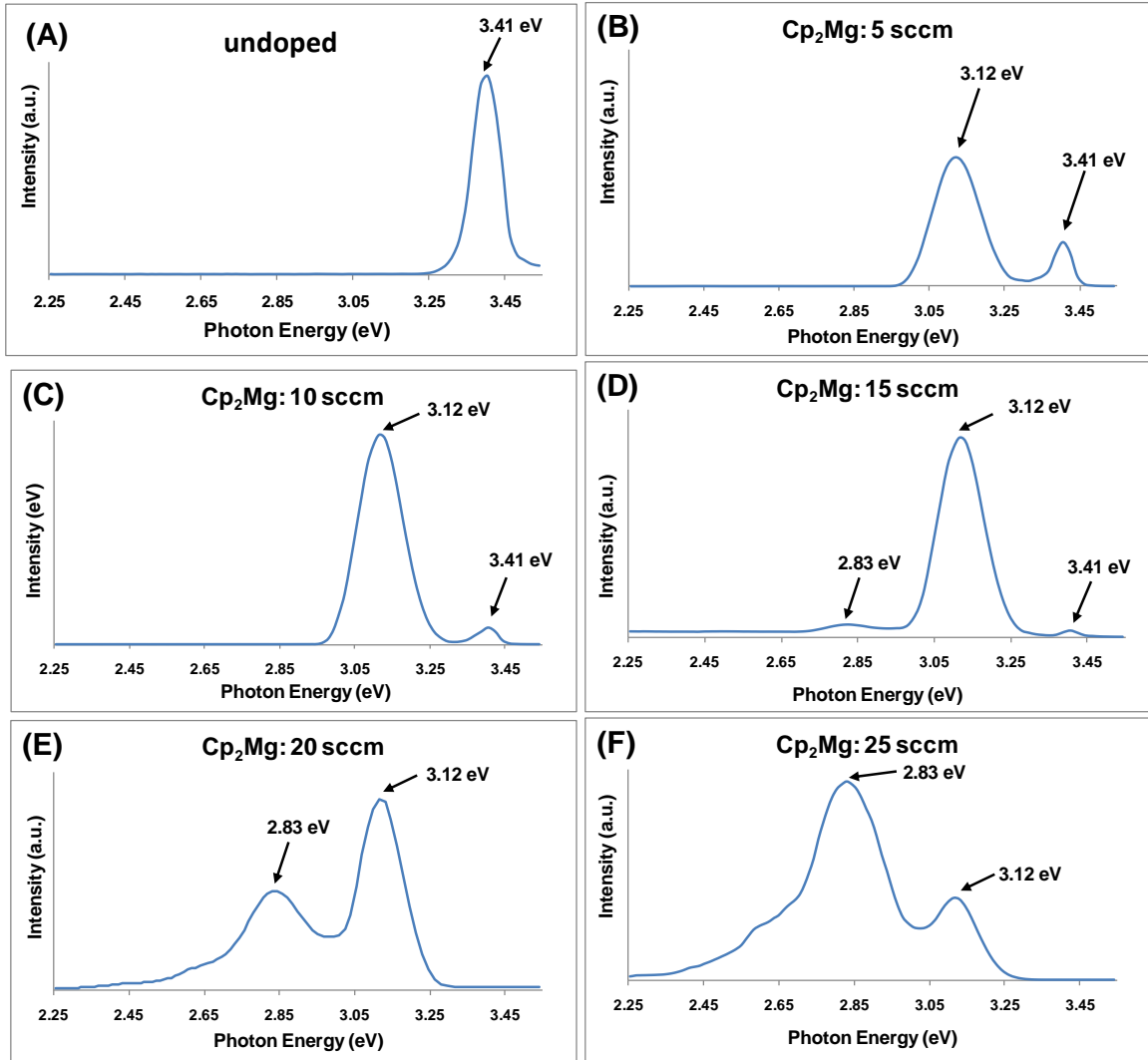


Figure 6-5. PL spectra of Mg-doped GaN films as a function of Mg incorporation. A) undoped, B) Cp_2Mg : 5 sccm, C) Cp_2Mg : 10 sccm, D) Cp_2Mg : 15 sccm, E) Cp_2Mg : 20 sccm, and F) Cp_2Mg : 25 sccm.

CHAPTER 7
EFFECT OF AIR EXPOSURE ON Cu DIFFUSION BARRIER PROPERTIES OF TaN THIN
FILMS GROWN BY ATOMIC LAYER DEPOSITION

7.1 Introduction

As device size decreases on integrated circuit (ICs), aluminum and SiO₂ based interconnect metallization is being replaced with Cu and low- κ dielectrics. Low resistivity of Cu and low dielectric constant of low- κ materials enable faster electric signal by minimizing RC (Resistance & Capacitance) time delay. Cu also has excellent resistance to electromigration, which is common problem of aluminum based metallization. [111, 154] However, Cu diffuses into Si and SiO₂ very rapidly ($D_{Cu} \sim 2 \times 10^{-5} \text{ cm}^2/\text{s}$ at 500 °C), and causes many problems in device performance such as increase in contact resistance, barrier height change, leakage in $p-n$ junction, and destruction of electric connections. [155, 156] Therefore, an appropriate Cu diffusion barrier is required between Cu and its underlying layer to block interdiffusion of Cu.

Among various transition metals and their nitrides, Ta/TaN is known as optimal Cu diffusion barrier due to its highest thermal stability and good adhesion with Cu. Currently, a bi-layer structure of Ta/TaN deposited by physical vapor deposition (PVD) is being employed in commercial applications. However, PVD has an inherent limitation in the deposition of sub-100 nm nodes and high aspect ratio structures because of directional nature of depositing flux and high sticking probability. [117] Accordingly, atomic layer deposition (ALD) is receiving extensive attention on the deposition of Cu diffusion barrier due to its unique features such as excellent conformality on high aspect ratio structured and uniformity over large areas. [157] In ALD, the gaseous precursors are alternately supplied to the substrate, and reactor is purged with an inert gas between precursor pulses. Under properly chosen growth conditions, the film growth proceeds via self-saturation surface reactions. This self-saturation reaction enables the

film thickness to be controlled easily, and the deposited films have excellent conformality and large area uniformity.

There have been reports on TaN-ALD using halide sources (TaCl_5 , TaBr_5) and NH_3 . The films were mostly polycrystalline Ta_3N_5 phase, which has too many grain boundaries, in other word, fastest diffusion pathways for Cu. High resistivity ($> 10^4 \mu\Omega\text{-cm}$) was also an issue for diffusion barrier. [16, 17] As an alternate approach, metalorganic (MO) sources such as *pentakis(dimethylamido) tantalum* (PDMAT) [18] and *tert-butylimido-tris(diethylamido) tantalum* (TBTDET) [19, 20] had been used as a precursor for TaN-ALD. A fcc-NaCl type nanocrystalline structure of TaN was obtained by using PDMAT as Ta source. [18] Thermal ALD TaN films deposited with TBTDET showed lower density and higher resistivity than plasma-enhanced (PE) ALD TaN. Low resistivity of PE-ALD TaN was somewhat attributed to formation of Ta-C bonds. [17]

It is well known that there are several factors such as impurities, thickness, stress, and defects that affect the properties of diffusion barriers. [21-24] Generally, O, C, and H are the main impurities in ultrathin films deposited by ALD because they are prepared using metalorganic precursors. These impurities are known to change the structures and properties of TaN thin films [17, 25, 117]. There is a report on the oxygen effect on the performance of nitride barrier in the case of oxygen stuffing process for TiN barrier. [27]

In this study, TaN thin films were deposited by the ALD method from TBTDET and NH_3 . In contrast to previous studies on ALD-TaN using TBTDET and NH_3 [19, 20], the process temperature window, which is an essential ALD feature for precise thickness control, was examined from 150 to 400 °C. As a barrier candidate, it is necessary to investigate thermal behavior of TaN films and corresponding stack of Cu/TaN/Si. Therefore, the barrier

performance of TaN thin films was examined with the stack of Cu/TaN/Si, which was prepared by ALD of TaN followed by CVD of Cu. To understand the effect of air exposure on the thermal stability of diffusion barrier, Cu/TaN/Si stacks were prepared with and without an oxide interfacial layer between Cu and TaN. Both stacks were annealed at the same temperature, and compared using different thermal stability tests.

7.2 Experimental Details

ALD of TaN was performed on standard *p*-type Si(100) substrate in a custom-built cold-wall vertical ALD reactor. TBTDET (prepared by Dr. McElwee-White group) and NH₃ were used as precursors. TBTDET contained in a bubbler was heated to 85 °C and pulsed into the reactor by a carrier gas of N₂ with the aid of a solenoid valve. NH₃ (99.9999 %, Matheson Tri-Gas) was introduced intermittently into the reactor using pneumatically actuated valve. Pure N₂ (99.999 %, Airgas) was used as the purging gas, and sweeps TBTDET and NH₃ lines as well as the reactor during the purge step. TaN films were deposited from 200 to 400 °C with a typical growth pressure of 1 torr. One ALD cycle consists of four stages: TBTDET supply (step 1), N₂ purge (step 2), NH₃ supply (step 3) and N₂ purge (step4). The gas flow sequence was as follows: TBTDET supply for 6 to 12 s with 50 sccm, N₂ purge for 30 s with 500 sccm, NH₃ supply for 10 s with 200 sccm, and N₂ purge for 30 sec with 500 sccm.

To investigate the diffusion barrier performance of TaN films for Cu metallization, a Cu layer of 100 nm thickness was deposited onto the ALD-TaN layer by chemical vapor deposition (CVD) using (tmvs)Cu^I(hfac) as a single source precursor, where tmvs = trimethylvinylsilane and hfac = hexafluoroacetylacetonate. (tmvs)Cu^I(hfac) in the bubbler was heated to 45 °C, and delivered to the reactor with the flow rate of 50 sccm by the carrier gas of N₂. H₂ was used as the ambient gas, and supplied into the reactor with the flow rate of 300 sccm. The growth temperature was set to 200 °C. To investigate the effect of exposure of the TaN barrier film to

air before deposition of the Cu layer in the stacks, the TaN/Si samples were either directly transferred to the Cu-CVD chamber under vacuum or first exposed to room temperature air before loading into the chamber. The stack of Cu 100 nm/non air-exposed TaN/Si will be designated as in-situ group (IN). In comparison, the stack of Cu 100 nm/air-exposed TaN/Si will be designated as ex-situ group (EX). Both of EX and IN sets of Cu/TaN/Si stacks were then annealed in the Cu-CVD chamber at elevated temperatures for 30 min as a diffusion barrier test. Annealing was under N₂ atmosphere in order to prevent Cu from oxidation. After annealing, the quality of diffusion barrier was evaluated by checking Cu_xSi formation using XRD, four point probe, and the etch-pit test. In the etch-pit test, Cu was first chemically etched away by diluted HNO₃ solution with HNO₃:H₂O=1:20. TaN was etched by mixture of NH₄OH, H₂O₂, and H₂O with a ratio of 1:1:4. Then, the Si surface was etched with the Seeco etch solution (a mixture of 0.15 M K₂Cr₂O₇ and HF with a ratio of 1:2 for 5 s. After etching, the appearance of inverse pyramidal shaped etch-pits was observed by scanning electron microscope (SEM).

To measure the thickness of the film for the growth rate, X-ray reflectometry (XRR) was used by Philips MRD X'Pert system. To identify the film microstructure, X-ray diffraction (XRD) was performed in a Philips APD 3720, operating with Cu K α radiation (40kV and 20mA). To measure sheet resistance of annealed samples, 4-point probe by Alessi Industries four-point probe was used. To observe the appearance of etch pit, SEM was used by JEOL JSM-6335F. To observe the change of interfacial layer of Cu/TaN/Si stack through annealing, transmission electron microscope (TEM) was used by JEOL TEM 2010F, equipped with an X-ray energy dispersive spectrometer (EDS). For TEM specimen preparation, focused ion beam (FIB) was used by FEI Strata DB 235.

7.3 Results and Discussion

7.3.1 ALD of TaN Thin Films

7.3.1.1 Film Growth

The effect of the exposure time on the deposition rate of TaN thin films was examined with varying TBTDET exposure time. The TaN film thickness was measured by XRR. The exposure time of TBTDET was changed from 6 to 12 s with fixed NH₃ exposure time of 10 s and purge time of 10 s. Figure 7-1 A shows the growth rate in one ALD cycle as a function of exposure time of TBTDET at $T_{\text{growth}} = 250$ °C. Figure 7-1 A suggests that the growth rate increases with the exposure time of TBTDET, and remains constant at 0.26 nm/cycle from 4 to 11 s of exposure time, indicating it reached the surface saturation region, which is one of the unique features in ALD. The growth rate increased upto 0.35 nm/cycle above 11 s of exposure time, which indicates the CVD-like region. The deposition rate in saturation region was 0.26 nm/cycle, which is 53.6% of lattice constant (0.49 nm) of *h*-TaN phase. The reason of sub-monolayer deposition per cycle in ALD as been considered to the incomplete saturation coverage of metal-containing precursor due to the steric hindrance of adsorbed metal precursors. [117]

The thickness of each ALD-TaN was measured as a function of growth temperature to verify the process temperature window. All depositions were performed at the self-saturation growth conditions obtained from TBTDET exposure time results above. TBTDET (9 s, 20 sccm), N₂ purge (10 s, 200 sccm), and NH₃ (10 s, 20 sccm) exposure time and flow rate were fixed with changing the growth temperature varied from 200 to 400 °C for 80 cycles. Figure 7-1 B shows the thickness as a function of growth temperature. The film thickness increased with increasing growth temperature below 200 °C. The precursor adsorption on to the surface active site and the reaction between adsorbed precursor and surface species are thermally activated processes. Therefore, the surface saturation is kinetically limited to the thermal energy, which

leads to higher deposition rate at higher temperature. The film thickness remained constant (20 +/- 1 nm) from 200 to 300 °C, suggesting the ALD process temperature window. When the growth temperature is high enough to give sufficient thermal energy for the precursor adsorption and surface reactions, the growth rate remains constant as growth temperature goes up. Above 300 °C, the film thickness further increased with increasing growth temperature, indicating the disturbance of self-limiting growth. This behavior can be explained by the thermal decomposition of TBTDET, causing a CVD-like process. Thermal decomposition of TBTDET has been reported to occur above 300 °C [20].

7.3.1.2 Barrier Tests

To verify the minimum thickness of ALD-TaN that could block the diffusion of Cu, ALD-TaN layers of 0.7 to 10 nm were tested. The test structures were formed by depositing the various thicknesses of TaN barrier films on Si substrate and covering them with a Cu layer of 100 nm thickness grown by sputter system. The samples were then thermally annealed under N₂ at 500 °C for 30 min. XRD measurement was used to identify the formation of Cu_xSi from annealed samples, which reveals the failure of diffusion barrier. As shown in Fig. 7-2 A, barriers of less than 1.6 nm thickness showed the diffraction peak of Cu_xSi, suggesting that the diffusion barrier failed. Other films thicker than 3.8 nm showed the peaks assigned to TaN and Cu, but not Cu_xSi peaks.

To confirm the minimum barrier thickness obtained from XRD, cross sectional TEM was used on an annealed stack of Cu/3.8 nm TaN/Si. As shown in Fig. 7-2B, there is no diffusion of Cu through TaN and Si after annealing with 3.8 nm thickness of ALD-TaN barrier. Both Cu/TaN and TaN/Si interface can be clearly observed without any intermixing between layers, which indicates that a 3.8 nm barrier film blocks the Cu diffusion.

The etch-pit test was used to determine the formation of Cu_xSi on the Si surface more sensitively. As shown in Fig. 7-3, etch-pits are observed on the Si surface with 1.6 nm thickness barrier as a result of barrier failure. On the other hand, 3.8 nm thickness barrier exhibits no etch-pit, indicating the critical thickness of ALD-TaN barrier is between 1.6 and 3.8 nm.

7.3.2 *in-situ* (IN) Set vs. *ex-situ* (EX) Set

7.3.2.1 Microstructure of IN and EX Sets

The microstructures of as-grown Cu/non air-exposed TaN/Si (IN) and Cu/air-exposed TaN/Si (EX) samples were compared from cross-sectional TEM images. As shown in Fig. 7-4 B, there is an interlayer with thickness of about 0.5 to 1 nm between Cu and TaN for EX sample. There is, however, no interlayer found at the interface of Cu/TaN for IN sample (Fig. 7-4 A). The interlayer at the Cu/TaN interface for EX is believed to be TaO_xN_y , which is formed by surface oxidation of TaN through air exposure before loading into the chamber. There is a previous report that TaO_xN_y forms as a result of the surface oxidation of TaN [158].

7.3.2.2 Barrier Tests

To compare the barrier properties of IN and EX sets, the test structures have the same thickness of TaN (4 nm) and Cu (100 nm). Cu/TaN/Si structures were thermally annealed under N_2 at elevated temperature from 400 to 650 °C for 30 min. XRD measurements, sheet resistance measurements, and etch-pit tests were performed on the annealed samples to determine barrier failure temperatures of TaN diffusion barrier for IN and EX sets.

XRD measurements were used to identify the formation of Cu_xSi on the Si surface due to barrier failure. The TaN barrier with IN set is observed to fail at 630 °C (Fig. 7-5 A), while the EX set fails at 650 °C (Fig. 7-5 B). The formation of Cu_xSi is determined when new reflections appear in the XRD pattern near 44.00 to 46.00° 2θ . As the annealing temperature is increased, Cu XRD peak intensities generally increase due to the recrystallization of Cu upon annealing.

Cu peak intensities decrease as Cu_xSi peaks appear due to the consumption of Cu in the formation of silicide [159]. In case of the IN set, the Ta_5Si_3 peak starts to appear at $42.03^\circ 2\theta$ (JCPDS 06-0594) when Cu_xSi peaks are observed.

According to the sheet resistance measurement, barriers for the IN and EX sets were stable up to 600°C (Fig. 7-6). Up to annealing at 550°C , the sheet resistances of IN and EX sets decreased gradually as a result of the grain growth of Cu. This Cu grain growth is shown by the sharpening of Cu peaks in XRD patterns as the annealing temperature is elevated (Fig. 7-5). The EX set generally shows the higher sheet resistance up to 550°C because of the TaO_xN_y interlayer. After annealing at 615°C , the sheet resistance of the IN set increases more than one order of magnitude. The sheet resistance of the EX set, however, increases markedly after annealing at 630°C . From this result, the barrier failure temperatures are determined as 615°C for IN set and 630°C for EX set, respectively. The increase of sheet resistance for barrier failure can be explained by the intermixing of Cu and Si through the barrier, and formation of more highly resistive Cu_xSi .

From XRD and sheet resistance measurements, the change in the sheet resistances is likely to be detectable for lower annealing temperature than the Cu_xSi peak detection in XRD. The sheet resistance measurements were done by 4-point probe, which needs smaller volume of Cu_xSi compound than XRD measurement to detect the failure. In order to determine the formation of Cu_xSi on Si substrate more sensitively, the etch-pit test was used. In the etch-pit test, defects caused by the formation of Cu_xSi on Si substrate are shown as inverse-pyramidal shape etch-pit after etching by Secco etchant. As shown in Fig. 7-7, the first etch-pits were observed after annealing at 600°C for IN set (Fig. 7-7B), and 630°C for EX set (Fig. 7-7I), respectively. As the annealing temperature goes up, the number of etch-pits per unit area

increases. Barrier failure temperatures from etch-pit tests were lower than those from XRD and sheet resistance measurements. Better sensitivity of the etch-pit test for barrier failure temperature determination has been previously reported [160, 161].

Barrier failure temperatures for IN and EX sets are shown in Table 7-1 with different barrier test methods. Etch-pit test is found to be the most sensitive barrier test, while XRD measurement is the least sensitive. EX set shows a higher barrier failure temperature than IN set over every barrier test method. The TaO_xN_y interfacial layer formed by air exposure of TaN appears to have a beneficial role in preventing Cu diffusion. To understand the beneficial role of TaO_xN_y interfacial layer, the failure mechanism of TaN barrier was investigated. It was approximated that the barrier thickness is associated to the average diffusion length at the temperature when the barrier fails. Barrier failure temperatures for different barrier thickness stacks of IN and EX sets were shown in Fig. 7-8A. The barrier failure temperatures were determined by 4-point probe measurement. In this study, thermal annealing was performed by ramping the annealing temperature at a rate of 1 °C/s. The activation energy (E_a) for diffusion was determined by plotting $\ln(L^2/T^2)$ over $1/kT$ for each barrier thickness [162]. Figure 7-8B shows the plot of $\ln(L^2/T^2)$ and $1/kT$ from L and T data of Fig. 7-8A. From the slope of the plot, E_a of diffusion for each barrier was obtained as 1.08 +/- 0.05 and 1.26 +/- 0.02 eV for the IN and EX sets, respectively. The activation energy for both the IN and EX sets are close to previously reported values of E_a for Cu diffusion along grain boundaries of TaN (1.3 eV) [162, 163]. Thus, TaN diffusion barrier failure is mainly due to the diffusion of Cu along grain boundaries of TaN, which are generated by the recrystallization of TaN. The difference of E_a for IN and EX, however, is 0.2 eV. And, the barrier failure temperature of IN is lower than EX up to 30 °C as shown in Table 7-1. The difference can be explained by Ta_5Si_3 formation in failure sample of

IN. As shown in Figs. 7-5A and B, barrier failure sample of IN shows the Ta_5Si_3 peak, while no Ta_5Si_3 peak is detected in the EX sample. Ta_5Si_3 has been previously reported to be found in ternary phase of Si-Ta-N because TaN is thermodynamically unstable with respect to Si at 900 K from ternary phase diagram at 900 K [164]. Thus, Ta_5Si_3 in failure IN sample is formed by interfacial reaction of TaN and Si. Ta_5Si_3 has a bigger grain size than TaN, which gives faster diffusion pathway to Cu along grain boundaries. It is concluded that barrier failure for IN is due to the diffusion of Cu along grain boundaries of TaN and Ta_5Si_3 formed by interfacial reaction of TaN and Si. The barrier failure for the EX sample is due to diffusion of Cu along grain boundaries of TaN only. Grain boundaries of TaN and Ta_5Si_3 for IN sample provide faster diffusion pathways than that of TaN only for EX sample. Thus, IN sample shows lower failure temperature than EX sample.

7.4 Conclusions

TaN films were grown by thermal ALD using TBTDET and NH_3 . ALD characteristics such as process windows were shown, and the critical thickness of TaN barrier was determined as 3.8 nm from XRD and TEM measurements. The effect of air exposure on Cu barrier properties of TaN film was investigated by comparison of air exposed TaN to vacuum transferred TaN with stacks of Cu/TaN/Si. XRD, sheet resistance measurements, and the etch-pit test were used to determine barrier failure temperatures of air exposed and vacuum transferred Cu/TaN/Si stacks. It was found that air exposed TaN has higher barrier failure temperature consistent with a faster diffusion pathway of grain boundaries of TaN and Ta_5Si_3 in vacuum transferred stacks. TaO_xN_y interfacial layer appears to have a beneficial role in preventing Cu transport by suppressing the formation of Ta_5Si_3 .

Table 7-1. Barrier failure temperatures determined by different barrier testing methods for Cu/TaN/Si stacks of vacuum transferred and air exposed TaN.

Cu/TaN/Si	T_{failure} by XRD (°C)	T_{failure} by R_s (°C)	T_{failure} by etch-pit (°C)
Vacuum transferred TaN	630	615	600
Air exposed TaN	650	630	630

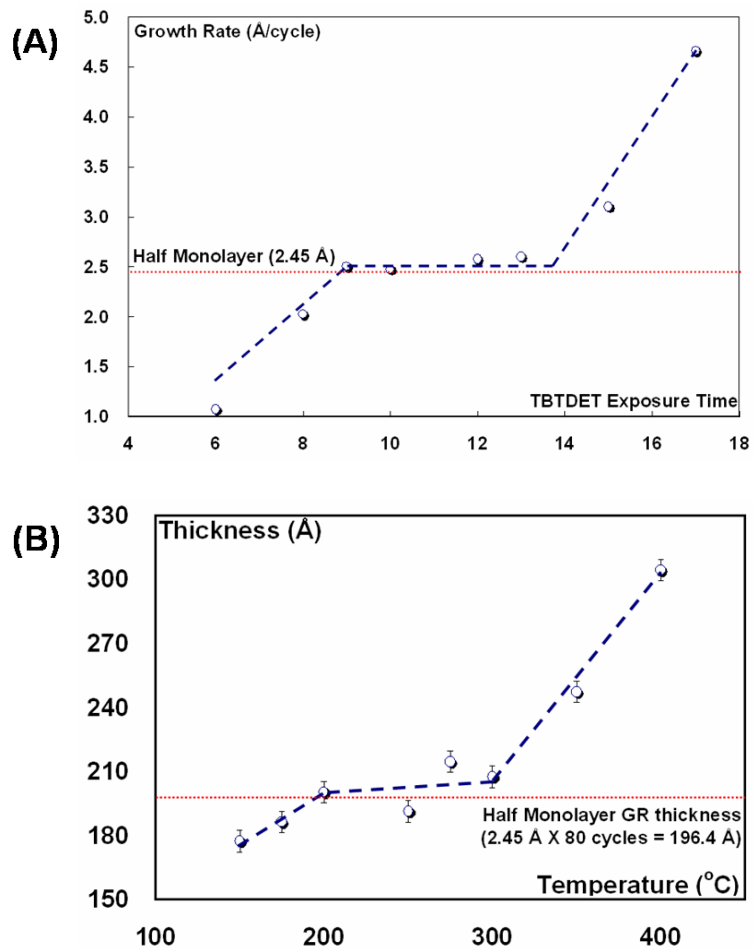


Figure 7-1 A) Growth rate of ALD-TaN as a function of TBTDET exposure time. Film was deposited at 250 °C, and 10 s of purge and NH₃ exposure time. B) Thickness of ALD-TaN films as a function of growth temperature. Film was deposited with 9 s of TBTDET exposure time and 10 s of purge and NH₃ exposure time. Taken from Ref [165].

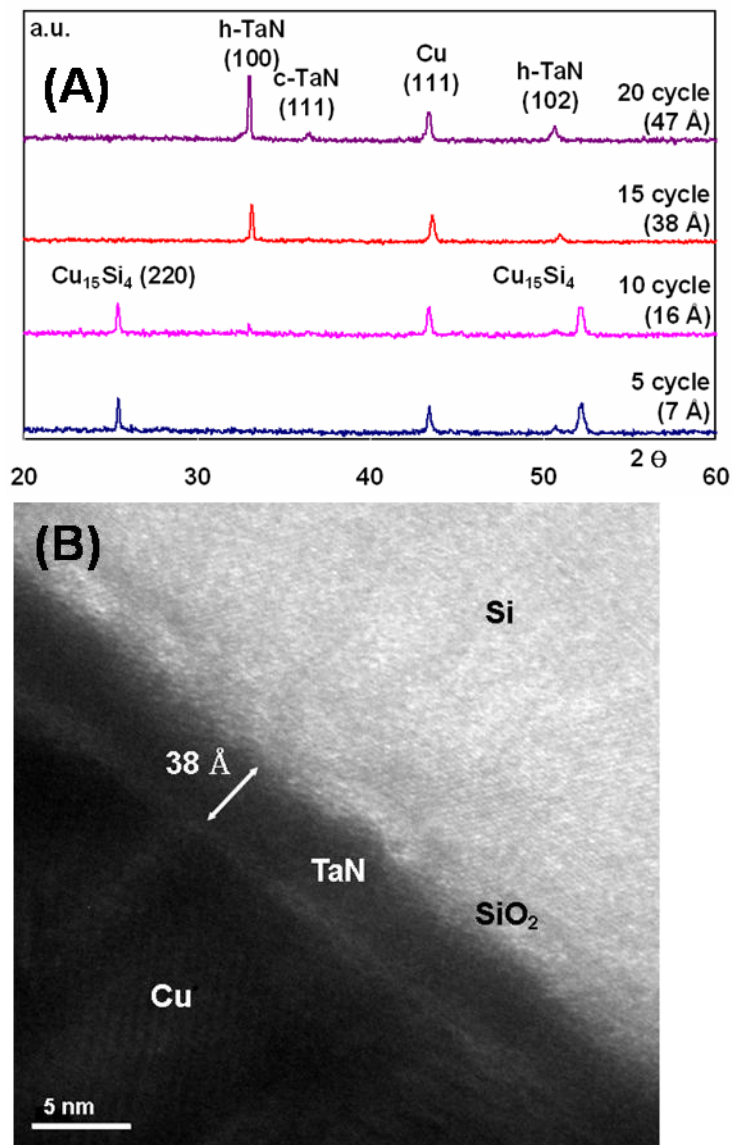


Figure 7-2. A) XRD patterns of Cu/TaN/Si annealed at 500 °C for 30 min. B) Cross-sectional TEM image of Cu/TaN/Si structure. TaN was grown by ALD for 15 cycles at 9 s of TBTDET exposure time at 300 °C. Taken from Ref [165].

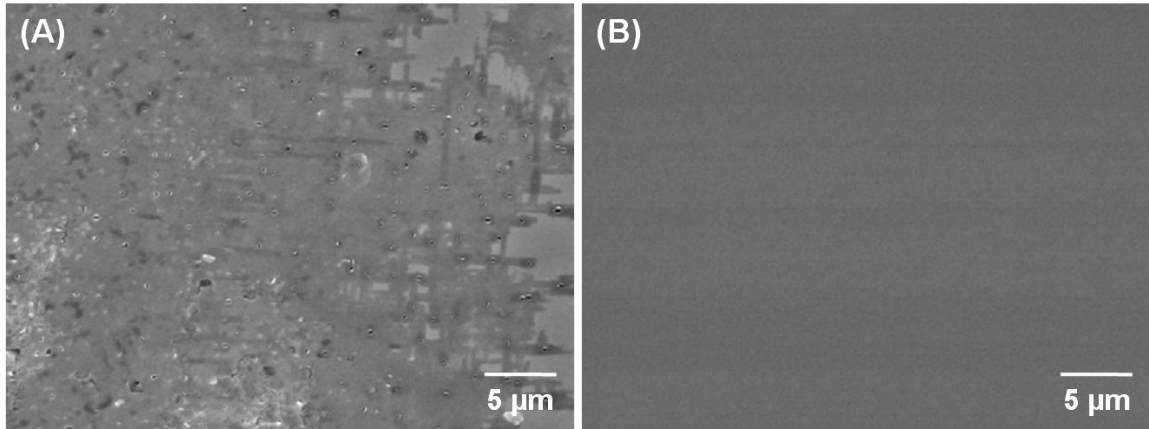


Figure 7-3. SEM images of Si surface after annealing Cu/TaN/Si at 500 °C for 30 min followed by the removal of Cu and TaN, and Secco etching for A) 10 cycles (16 Å) TaN film. B) 15 cycles (38 Å) TaN film. Taken from Ref [165].

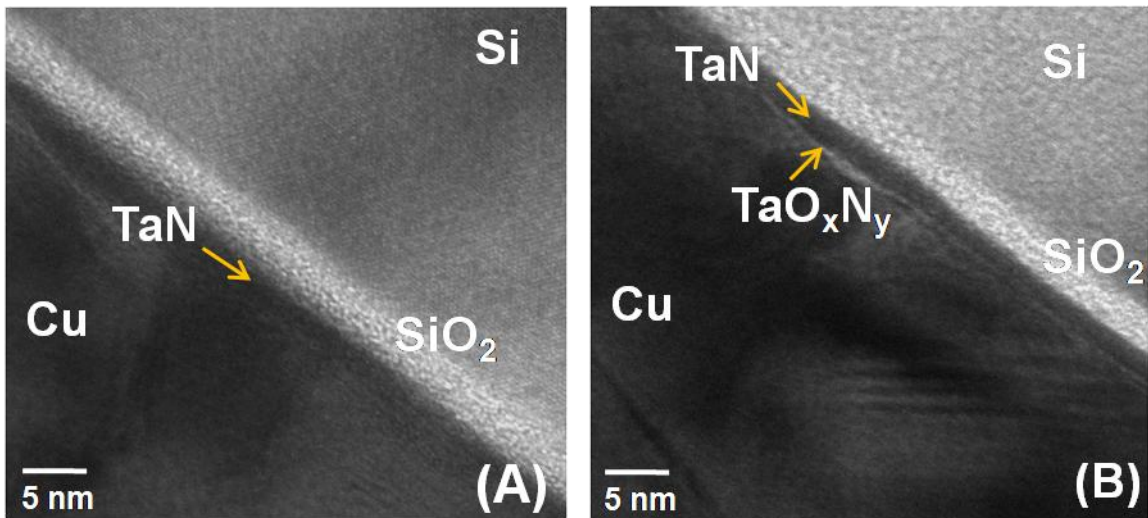


Figure 7-4. Cross-sectional TEM image of as-grown Cu/TaN/Si structure of A) vacuum transferred TaN. B) air exposed TaN.

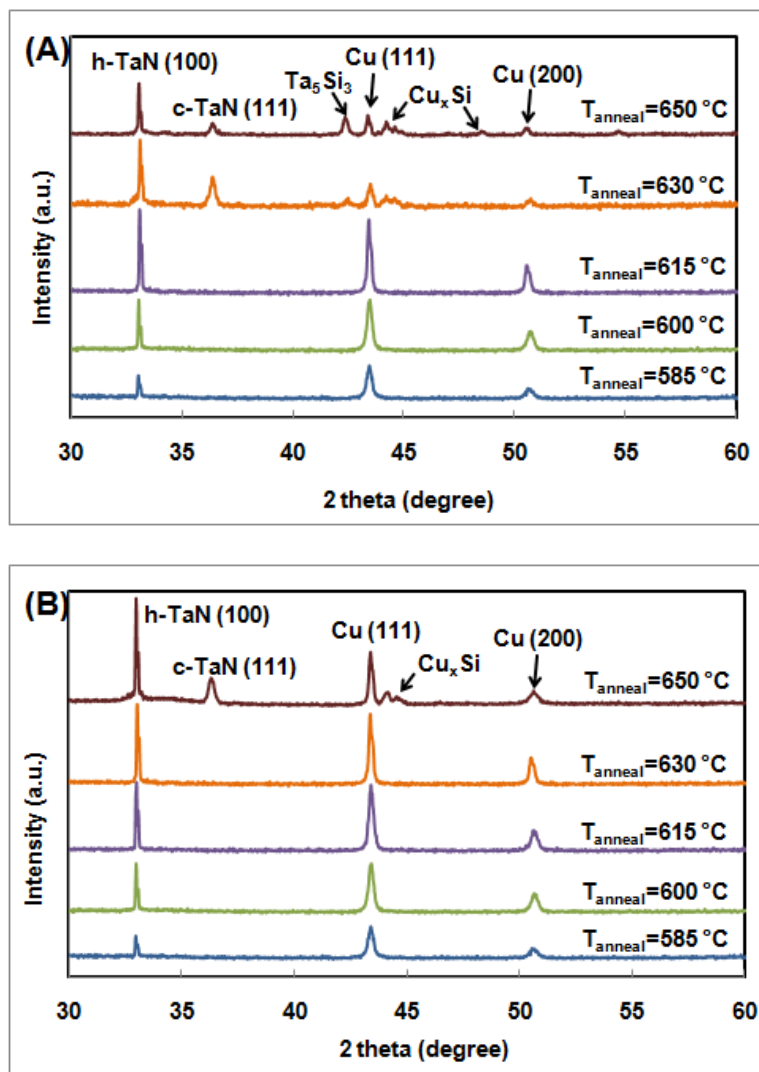


Figure 7-5. XRD patterns of annealed Cu/TaN/Si structure of A) vacuum transferred TaN. B) air exposed TaN at elevated annealing temperatures for 30 min.

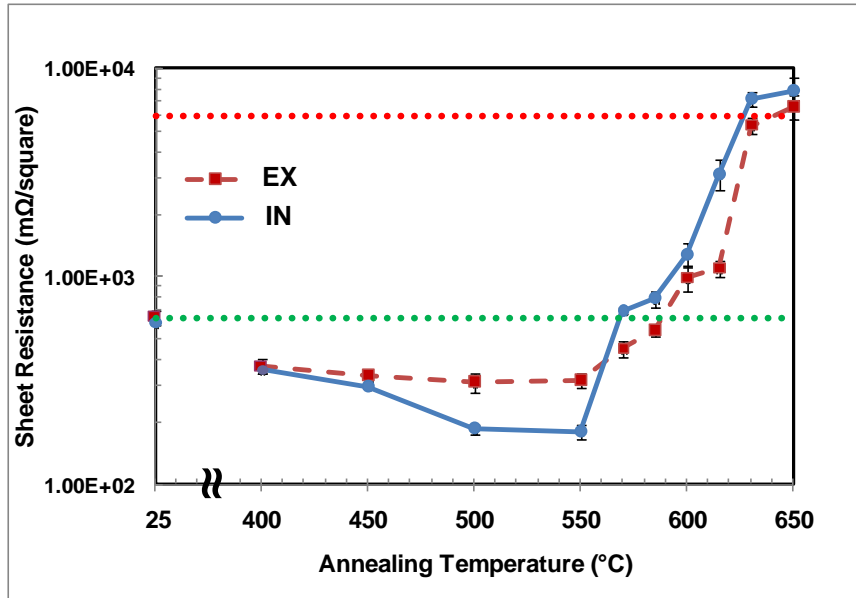


Figure 7-6. Sheet resistances of the Cu/TaN/Si structures for vacuum transferred and air exposed TaN as a function of the annealing temperature.

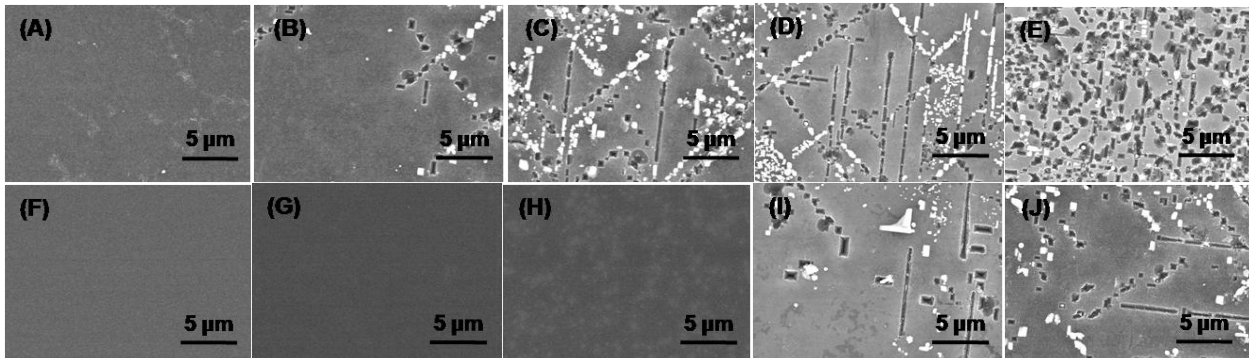


Figure 7-7. SEM image of etch-pits observed on Si surface of Cu/TaN/Si for vacuum transferred TaN at annealing temperature of A) 585 °C, B) 600 °C, C) 615 °C, D) 630 °C, and E) 650 °C. Si surface of Cu/TaN/Si for air exposed TaN at annealing temperature of F) 585 °C, G) 600 °C, H) 615 °C, I) 630 °C, and J) 650 °C.

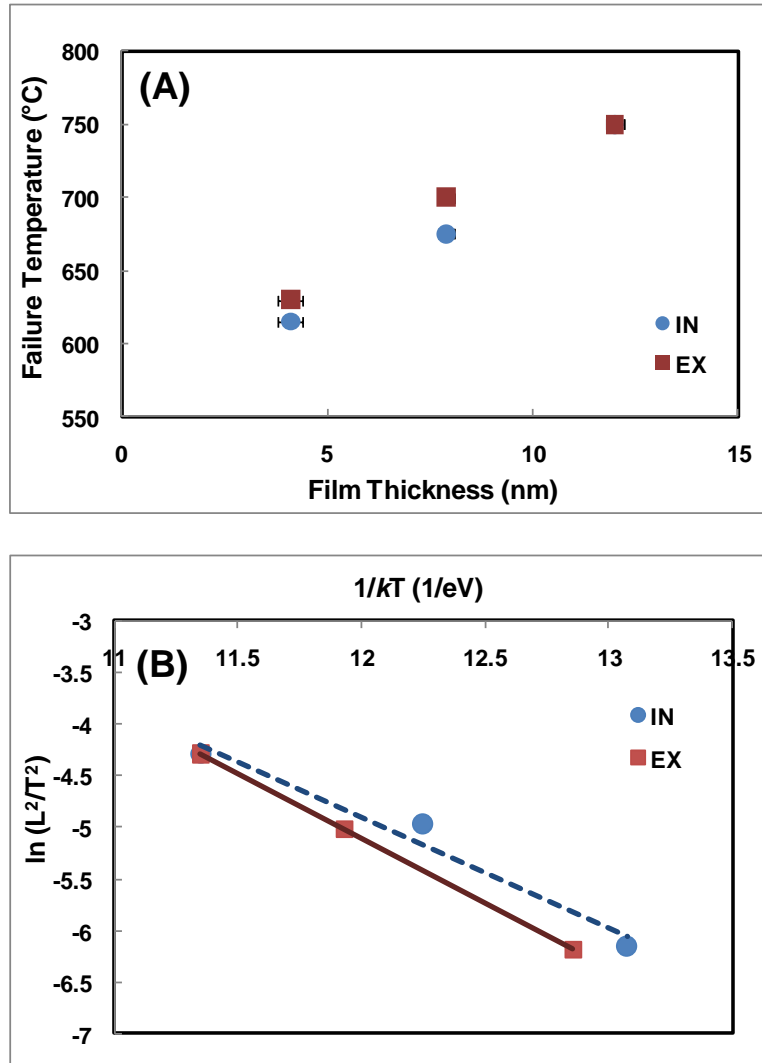


Figure 7-8. A) Barrier failure temperatures as a function of TaN barrier thickness. B) Plot of $\ln(L^2/T^2)$ vs $1/kT$ for Cu/TaN/Si stacks of vacuum transferred and air exposed TaN.

CHAPTER 8 FUTURE WORK AND SUGGESTIONS

8.1 Concerns of ALD-GaN for Device Application

This work demonstrated the growth of GaN on Si with ALD for the first time. ALD characteristics such as self-saturation window and temperature window were revealed. Film properties such as microstructure, surface morphology, and Cl incorporation were also investigated. As a pioneering research on GaN ALD on Si, this work covers many possible issues in the application to optoelectronic devices. The temperature window makes the deposition process much more controllable. The lack of Cl incorporation under ALD process window solves one of the most detrimental drawbacks of halide-ALD. However, more device-related issues such as optical and electrical properties were not considered here.

To be employed in LED or laser diodes, the PL emission wavelength and intensity needs to be considered. Also, carrier properties such as concentration and mobility need to be studied using Hall measurements. In addition, the crystallinity of the film needs to be improved. As shown previously, the ALD-GaN on Si showed two growth orientations which are not preferred for device application. Introducing buffer layers or sapphire substrate could result in better crystallinity.

8.2 ALD Doping of GaN

For optoelectronic device applications, *p*-type doping of GaN was performed in this work. The most commonly used *p*-type dopant, Mg, was employed for HVPE of GaN. The optimized growth condition for obtaining the highest hole concentration, which was $3.2 \times 10^{17} \text{ cm}^{-3}$ at 15 sccm of Cp_2Mg flow rate. PL spectra showed the emission peak at 3.12 eV with high intensity. The electrical and optical properties of Mg-doped GaN in this work seem to be practical for LED

application. However, HVPE of *p*-GaN is not the most suitable for the application to novel design LED which is proposed in this work.

As mentioned in the introduction chapter, *p*-GaN was deposited on *n*-GaN nanorod, and filled the space between nanorods in a novel design LED structure. For better performance of this LED, *p*-GaN needs to be deposited on high aspect ratio *n*-GaN nanorods with good conformality and step coverage. It is known that ALD is a superior deposition for excellent conformality, step coverage, and uniformity. Therefore, *p*-type doping of GaN using ALD method needs to be developed for better performance of nanorod based LED.

The biggest difference between HVPE and ALD doping is the flow sequence of precursors. For HVPE, both GaCl₃ and Cp₂Mg were supplied to the growth zone with NH₃. In ALD, the co-flow of GaCl₃ and Cp₂Mg needs to be supplied to the growth zone separating from NH₃ with a purge step in between. For the better doping level controllability, GaCl₃ and Cp₂Mg can be supplied to the growth zone through separate exposure steps. Various sequences for the exposure of GaCl₃, Cp₂Mg, and NH₃ can be tested to obtain optimum doping level or optical property. Also, the control of the Cp₂Mg exposure step would make ALD doping extendable to the delta-doping of GaN which is a promising doping methods to achieve MQW GaN.

8.3 Device Fabrication of Nanorod-based LED

As mentioned above, improvements in the optical, electrical, and structural quality of ALD-GaN are required to achieve nanorod-based LED structures. Also, ALD doping of GaN needs to be developed for the better performance of the LEDs. Even if these materials and processing requirements were satisfied, there is still a roadblock to achieve the proposed LED structure, which is the device fabrication issue. The basic unit of nanorod-based LED can be fabricated by the deposition processes such as nanorod growth and *p*-GaN deposition. However, there are more device components to be fabricated.

First of all, the insulating oxide needs to be deposited on the surface space in between nanorods. If there is an electrical connection between the *n*-GaN nanorods, the device could not convert the electric gain to light emission. In order to prevent this failure, each *n*-GaN nanorod needs to be electrically insulated by insulating oxide. Thus, a proper deposition process and material for this insulating oxide are required to be developed.

Secondly, the top side of each nanorod needs to expose the interface between *p*-GaN and *n*-GaN nanorod or active layer, if necessary. After the deposition of *p*-GaN, the top side of each nanorod becomes *p*-GaN ended. The emission light, however, is coming from the interface of *p*-*n* GaN. Thus, it is necessary to expose the interface of *p*-*n* GaN to the top side of nanorod. The most promising fabrication technique for this process is CMP. To prevent the collapse of the vertically aligned nanorods, the space between nanorods needs to be filled by *p*-GaN.

In addition, *p*- and *n*-contacts need to be fabricated on *p*- and *n*-GaN sides, respectively. Particularly, the *p*-contact has to be fabricated on the limited area of *p*-GaN to maximize the light emitting surface. The transparent top surface also needs to be fabricated with proper material and process.

8.4 Control of TaO_xN_y for Better Diffusion Barrier Properties

In this work, the effect of air exposure to ALD-TaN diffusion barrier properties was studied. The air exposed TaN exhibited the formation of TaO_xN_y in the interface of TaN and Cu. And, it was revealed by various barrier tests that TaO_xN_y interfacial layer showed a beneficial effect on the thermal stability of TaN diffusion barrier. On the other hand, TaO_xN_y contributed to the increase of electrical resistance. In this work, TaO_xN_y is formed by the exposure of TaN to ambient air. If the thickness and composition ratio of TaO_xN_y are controlled by introducing separate O source into current ALD process, the optimum thickness and composition ratio could be found to achieve the best thermal stability with minimum electrical resistance increase effect.

Then, TaO_xN_y could be employed as the next promising diffusion barrier material for Cu metallization.

LIST OF REFERENCES

- [1] S. J. Rosner, E. C. Carr, M. J. Ludowise, G. Girolami, H. I. Erikson, *Appl. Phys. Lett.* 70 (1997) 420-422.
- [2] J. H. You, H. T. Johnson, *J. Appl. Phys.* 101 (2007) 023516-6.
- [3] Y. C. Shen, G. O. Mueller, S. Watanabe, N. F. Gardner, A. Munkholm, M. R. Krames, *Appl. Phys. Lett.* 91 (2007) 141101-3.
- [4] G. Bai, S. Wittenbrock, V. Ochoa, R. Villasol, C. Chiang, T. Marieb, D. Gardner, C. Mu, D. Fraser, M. Bohr, in Materials Research Society Symposium Proceedings, Vol. 403, 1996, p. 501-506.
- [5] J. Xie, X. Ni, Q. Fan, R. Shimada, U. Ozgur, H. Morkoc, *Appl. Phys. Lett.* 93 (2008) 121107-3.
- [6] R. Leutenecker, B. Froschle, U. CaoMinh, P. Ramm, *Thin Solid Films* 270 (1995) 621-626.
- [7] O. Ambacher, *J. Phys. D: Appl. Phys.* 31 (1998) 2653-2710.
- [8] C. G. Van de Walle, J. Neugebauer, *J. Appl. Phys.* 95 (2004) 3851-3879.
- [9] Interconnect, International Technology Roadmap for Semiconductors (<http://www.itrs.net>), 2007.
- [10] S. M. Rossnagel, J. Hopwood, *Appl. Phys. Lett.* 63 (1993) 3285-3287.
- [11] J. Hillman, J. Hautala, S. Caliendo, in Proceedings of Advanced Metallization Conference, Vol. 313, San Diego, CA, 2000.
- [12] X. Chen, G. G. Peterson, C. Goldberg, G. Nuesca, H. L. Frisch, A. E. Kaloyeros, B. Arkles, J. Sullivan, *J. Mater. Res.* 14 (1999) 2043-2052.
- [13] A. Sherman, *J. Electrochem. Soc.* 137 (1990) 1892-1897.
- [14] N. Yokoyama, K. Hinode, Y. Homma, *J. Electrochem. Soc.* 138 (1991) 190-195.
- [15] P. Kapur, J. P. McVittie, K. C. Saraswat, *IEEE Transactions on Electron Devices* 49 (2002) 590-597.
- [16] L. Hiltunen, M. Leskela, M. Makela, L. Niinisto, E. Nykanen, P. Soininen, *Thin Solid Films* 166 (1988) 149.
- [17] T. Aaltonen, P. Alen, M. Ritala, M. Leskela, *Chem. Vapor Depos.* 9 (2003) 45-49.
- [18] Y. Y. Wu, A. Kohn, M. Eizenberg, *J. Appl. Phys.* 95 (2004) 6167.

- [19] J. Park, H. Park, S. Kang, *J. Electrochemical Soc.* 149 (2002) C28.
- [20] O. van der Straten, Y. Zhu, K. Dunn, E. T. Eisenbraun, A. E. Kaloyeros, *J. Mater. Res.* 19 (2004) 447-453.
- [21] L. Clevengern, A. Mutscheller, J. Harper, C. Cabral Jr, K. Bark, *J. Appl. Phys.* 72 (1992) 4918.
- [22] L. Clevengern, N. Bojarczuk, K. Holloway, J. Harper, C. Cabral Jr., R. Schad, F. Cardone, L. Stolt, *J. Appl. Phys.* 73 (1993) 300.
- [23] J. Kwak, H. Baik, J. Kim, S. Lee, *Appl. Phys. Lett.* 71 (1997) 2451.
- [24] M. Wang, Y. Lin, M. Chen, *J. Electrochem. Soc.* 145 (1998) 2538.
- [25] M. Juppo, M. Ritala, M. Leskela, *J. Electrochem. Soc.* 147 (2000) 3377-3381.
- [26] H. Kim, *J. Vac. Sci. Technol. B* 21 (2003) 2232-2261.
- [27] H. Chang, L. Chang, F. Chen, J. Kai, E. Tzou, J. Fu, Z. Xu, J. Egermeier, F. Chen, *Acta Mater.* 46 (1998) 2431.
- [28] W. C. Johnson, J. B. Parsons, *J. Phys. Chem.* 36 (1932) 2588-2594.
- [29] R. Juza, H. Hahn, *Anorg. Allg. Chem.* 239 (1938) 282-287.
- [30] H. G. Grimmeiss, H. Koelmans, *Z. Naturforsch.* 14 (1959) 264.
- [31] H. P. Maruska, J. J. Tietjen, *Appl. Phys. Lett.* 15 (1969) 327-329.
- [32] S. Yoshida, S. Misawa, S. Gonda, *Appl. Phys. Lett.* 42 (1983) 427-429.
- [33] H. Amano, N. Sawaki, I. Akasaki, Y. Toyoda, *Appl. Phys. Lett.* 48 (1986) 353-355.
- [34] H. Amano, M. Kito, K. Hiramatsu, I. Akasaki, *Jpn. J. Appl. Phys.* 28 (1989) L2112.
- [35] S. Nakamura, T. Mukai, M. Senoh, N. Iwasa, *Jpn. J. Appl. Phys.* 31 (1991) L139.
- [36] W. Götz, N. M. Johnson, J. Walker, D. P. Bour, H. Amano, I. Akasaki, *Appl. Phys. Lett.* 67 (1995) 2666-2668.
- [37] F. Wang, C. F. Lyons, K. B. Nguyen, S. A. Bell, H. J. Levinson, C. Y. Yang, *Us Patent* 6200907, 2001
- [38] Y. Kato, S. Kitamura, K. Hiramatsu, N. Sawaki, *J. Cryst. Growth* 144 (1994) 133-140.
- [39] S. Nakamura, T. Mukai, M. Senoh, *Appl. Phys. Lett.* 64 (1994) 1687-1689.

- [40] S. Nakamura, M. Senoh, N. Iwasa, S.-i. Nagahama, *Appl. Phys. Lett.* 67 (1995) 1868-1870.
- [41] S. Nakamura, M. Senoh, N. Iwasa, S.-i. Nagahama, T. Yamada, T. Mukai, *Jpn. J. Appl. Phys.* 34 (1995) L1332.
- [42] S. Nakamura, M. Seno, S.-i. Nagahama, N. Iwasa, T. Yamada, T. Matsushita, H. Kiyoku, Y. Sugimoto, *Jpn. J. Appl. Phys.* 35 (1996) L217.
- [43] Y. Shimooka, T. Iijima, S. Nakamura, K. Suguro, 36 (1997) 1589-1592.
- [44] S. Nakamura, M. Senoh, S.-i. Nagahama, N. Iwasa, T. Yamada, T. Matsushita, H. Kiyoku, Y. Sugimoto, T. Kozaki, H. Umamoto, M. Sano, K. Chocho, *Appl. Phys. Lett.* 72 (1998) 211-213.
- [45] J. Pankove, E. Miller, J. Berkeyheiser, *RCA Rev.* 32 (1971) 383.
- [46] H. P. Maruska, D. A. Stevenson, J. I. Pankove, *Appl. Phys. Lett.* 22 (1973) 303-305.
- [47] J. I. Pankove, M. A. Lampert, *Phys. Rev. Lett.* 33 (1974) 361.
- [48] J. Pankove, *RCA Rev.* 34 (1973) 336.
- [49] H. Amano, M. Kito, K. Hiramatsu, I. Akasaki, *Jpn. J. Appl. Phys.* 28 (1989).
- [50] S. Nakamura, T. Mukai, M. Senoh, *Jpn. J. Appl. Phys.* 30 (1991) L1998.
- [51] S. Nakamura, T. Mukai, M. Senoh, *Jpn. J. Appl. Phys.* 32 (1993) L16.
- [52] S. Nakamura, *J. Vac. Sci. Technol. A* 13 (1995) 705-710.
- [53] M. G. Craford, in IEEE Circuits Devices, Vol. 8, 1992, p. 25-29.
- [54] M. Meyer, in Semicond. Comp., Vol. 2, 1996, p. 32.
- [55] in Industry News, PennWell Corporation, Tulsa, OK, 2009.
- [56] M. A. Khan, R. A. Skogman, J. M. Van Hove, D. T. Olson, J. N. Kuznia, *Appl. Phys. Lett.* 60 (1992) 1366-1368.
- [57] N. H. Karam, T. Parodos, P. Colter, D. McNulty, W. Rowland, J. Schetzina, N. El-Masry, S. M. Bedair, *Appl. Phys. Lett.* 67 (1995) 94-96.
- [58] A. Koukitu, J. N. Kuznia, T. Taki, H. Seki, *Jpn. J. Appl. Phys.* 38 (1999) 4980.
- [59] H. Tsuchiya, M. Akamatsu, M. Ishida, F. Hasegawa, *Jpn. J. Appl. Phys.* 35 (1996) L748.
- [60] N. Koide, H. Kato, M. Sassa, S. Yamasaki, K. Manabe, M. Hashimoto, H. Amano, K. Hiramatsu, I. Akasaki, *J. Cryst. Growth* 115 (1991) 639-642.

- [61] S. Nakayama, T. Mukai, M. Senoh, *Jpn. J. Appl. Phys.* 31 (1992) 2883.
- [62] W. Götz, N. M. Johnson, C. Chen, H. Liu, C. Kuo, W. Imler, *Appl. Phys. Lett.* 68 (1996) 3144-3146.
- [63] L. B. Rowland, K. Doverspike, *Appl. Phys. Lett.* 66 (1995) 1495.
- [64] B. C. Chung, M. Gershenson, *J. Appl. Phys.* 72 (1992) 651-659.
- [65] H. Sato, T. Minami, E. Yamada, M. Ishii, S. Takata, *J. Appl. Phys.* 75 (1994) 1405-1409.
- [66] J. C. Zolper, R. G. Wilson, *Appl. Phys. Lett.* 68 (1996) 1945.
- [67] A. Edwards, M. Rao, B. Molnar, A. Wickenden, O. W. Holland, P. H. Chi, *J. Elec. Mat.* 26 (1997) 334.
- [68] W. Götz, N. M. Johnson, J. Walker, D. P. Bour, R. A. Street, *Appl. Phys. Lett.* 68 (1996) 667-669.
- [69] M. S. Brandt, N. M. Johnson, R. J. Molnar, R. Singh, T. D. Moustakas, *Appl. Phys. Lett.* 64 (1994) 2264-2266.
- [70] J. Neugebauer, C. G. Van de Walle, *Phys. Rev. Lett.* 75 (1995) 4452.
- [71] J. M. Myoung, K. H. Shim, C. Kim, O. Gluschenkov, K. Kim, S. Kim, D. A. Turnbull, S. G. Bishop, *Appl. Phys. Lett.* 69 (1996) 2722-2724.
- [72] P. Bergman, G. Ying, B. Monemar, P. O. Holtz, *J. Appl. Phys.* 61 (1987) 4589-4592.
- [73] J. Neugebauer, C. G. Van de Walle, *J. Appl. Phys.* 85 (1999) 3003.
- [74] O. Brandt, H. Yang, H. Kostial, K. H. Ploog, *Appl. Phys. Lett.* 69 (1996) 2707-2709.
- [75] J. C. Zolper, R. G. Wilson, S. J. Pearton, R. A. Stall, *Appl. Phys. Lett.* 68 (1996) 1945-1947.
- [76] *Semiconductors. Physics of Group IV Elements and III-V Compounds*, Landolt-Börnstein; O. Madelung, Ed.; Springer: Berlin, 1982; Vol. 17.
- [77] S. P. Murarka, I. V. Verner, R. J. Gutmann, *Cooper-Fundamental Mechanisms for Microelectronic Applications*; John Wiley and Sons: New York, NY, 2000.
- [78] R. I. M. Dang, N. Shigyo, *IEEE Electron Devices Lett.* EDL-2 (1981) 196.
- [79] S. P. Jeng, R. H. Havemann, M. C. Chang, *Mat. Res. Soc. Symp. Proc.* 337 (1994) 24.
- [80] V. G. Oklobdzija, *IBM J. Res. Dev.* 47 (2003) 567.

- [81] A. Scorzoni, I. De Munari, M. Impronta, R. Balboni, N. Kelaidis, http://www.diei.unipg.it/RICERCA/www_em.htm, 1998.
- [82] M. Sakimoto, T. Fujii, H. Yamaguchi, K. Eguchi, in Proceedings of IEEE Reliability Physics Symposium, Las Vegas, NV, 1995, p. 333.
- [83] A. A. Istratov, H. Hedemann, M. Seibt, O. F. Vyvenko, W. Schroter, T. Heiser, C. Flink, H. Hieslmair, E. R. Weber, *J. Electrochem. Soc.* 145 (1998) 3889-3898.
- [84] C. Flink, H. Feick, S. A. McHugo, W. Seifert, H. Hieslmair, T. Heiser, A. A. Istratov, E. R. Weber, *Phys. Rev. Lett.* 85 (2000) 4900.
- [85] A. E. Kaloyeros, X. Chen, T. Stark, K. Kumar, S.-C. Seo, G. G. Peterson, H. L. Frisch, B. Arkles, J. Sullivan, *J. Electrochem. Soc.* 146 (1999) 170-176.
- [86] S.-L. Cho, K.-B. Kim, S.-H. Min, H.-K. Shin, S.-D. Kim, *J. Electrochem. Soc.* 146 (1999) 3724-3730.
- [87] R. Fix, R. G. Gordon, D. M. Hoffman, *Chem. Mater.* 5 (1993) 614-619.
- [88] M. H. Tsai, S. C. Sun, H. T. Chiu, C. E. Tsai, S. H. Chuang, *Appl. Phys. Lett.* 67 (1995) 1128-1130.
- [89] L. Hiltunen, M. Leskelä, M. Mäkelä, L. Niinistö, E. Nykänen, P. Soininen, *Thin Solid Films* 166 (1988) 149-154.
- [90] M. Ritala, P. Kalsi, D. Riihela, K. Kukli, M. Leskela, J. Jokinen, *Chem. Mater.* 11 (1999) 1712-1718.
- [91] H. Kim, A. J. Kellock, S. M. Rosnagel, *J. Appl. Phys.* 92 (2002) 7080-7085.
- [92] E. Eisenbraun, O. van der Straten, Y. Zhu, K. Dovidenko, A. E. Kaloyeros, in IEEE International Interconnect Technology Conference, Burlingame, CA, 2001, p. 207.
- [93] K. I. Choi, B. H. Kim, S. W. Lee, J. M. Lee, in Interconnect Technology Conference, 2003. Proceedings of the IEEE 2003 International, Burlingame, CA, 2003, p. 129.
- [94] J.-S. Park, H.-S. Park, S.-W. Kang, *J. Electrochem. Soc.* 149 (2002) C28-C32.
- [95] Y. Y. Wu, A. Kohn, M. Eizenberg, *J. Appl. Phys.* 95 (2004) 6167-6174.
- [96] A. Furuya, H. Tsuda, S. Ogawa, *J. Vac. Sci. Technol. B* 23 (2005) 979-983.
- [97] A. Furuya, N. Ohtsuka, N. Ohashi, S. Kondo, S. Ogawa, *J. Vac. Sci. Technol. A* 24 (2006) 103-105.
- [98] W. J. Maeng, S.-J. Park, H. Kim, *J. Vac. Sci. Technol. B* 24 (2006) 2276-2281.

- [99] H. Kim, C. Detavenier, O. van der Straten, S. M. Rossnagel, A. J. Kellock, D. G. Park, J. Appl. Phys. 98 (2005) 014308-8.
- [100] S. Subbanna, P. Agnello, E. Crabbe, R. Schulz, S. Wu, K. Tallman, M. J. Saccamango, S. Greco, V. McGahay, A. J. Allen, B. Chen, T. Cotler, E. Eld, J. Lasky, H. Ng, A. Ray, J. Snare, L. Su, D. Sunderland, J. Sun, B. Davari, in IEEE International Electron Devices Conference, San Francisco, CA, 1996, p. 275.
- [101] C. K. Hu, K. Y. Lee, C. Uzoh, K. Chan, S. M. rossnagel, in Proceedings of Materials Research Society Symposium, San Francisco, CA, 1998, p. 507.
- [102] R. W. Hertzberg, Deformation and Fracture Mechanics of Engineering Materials; 3rd ed.; Wiley & Sons: New York, 1989.
- [103] F. W. Young, J. V. Cathcart, A. T. Gwathmey, Atca Metal. 4 (1956) 145.
- [104] C.-A. Chang, J. Appl. Phys. 67 (1990) 566-569.
- [105] P. S. Ho, Thin Solid Films 96 (1982) 301-316.
- [106] S. Kirkaldy, D. J. Young, Diffusion in the Condensated State; Institute of Metal: London, 1987.
- [107] D. Gupta, in Encyclopedia of Applied Physics, Vol. 5, John Wiley & Sons, 1993, p. 75.
- [108] K. C. Park, K. B. Kim, I. Raaijmakers, K. Ngan, J. Appl. Phys. 80 (1996) 5674-5681.
- [109] M. Stavrev, D. Fischer, F. Praessler, C. Wenzel, K. Drescher, J. Vac. Sci. Technol. A 17 (1999) 993-1001.
- [110] N. A. Gjostein, Diffusion in Metals; Am. Soc. Met.: Westerville, OH, 1973.
- [111] A. E. Kaloyeros, E. Eisenbraun, Ann. Rev. Mat. Sci. 30 (2000) 363-385.
- [112] R. Rosenberg, D. C. Edelstein, C.-K. Hu, K. P. Rodbell, Annu. Rev. Mater. Sci. 30 (2000) 229-262.
- [113] S. Strite, H. Morkoc, J. Vac. Sci. Technol. B 10 (1992) 1237-1266.
- [114] T. C. Shen, G. B. Gao, H. Morkoc, J. Vac. Sci. Technol. B 10 (1992) 2113-2132.
- [115] N. Yoshimoto, T. Matsuoka, T. Sasaki, A. Katsui, Appl. Phys. Lett. 59 (1991) 2251-2253.
- [116] B. T. McDermott, K. G. Reid, N. A. El-Masry, S. M. Bedair, W. M. Duncan, X. Yin, F. H. Pollak, Appl. Phys. Lett. 56 (1990) 1172-1174.
- [117] H. Kim, J. Vac. Sci. Technol. B 21 (2003) 2231-2261.

- [118] Y. Tsai, J. Gong, T. Lin, H. Lin, Y. Chen, K. Lin, *Appl. Surf. Sci.* 252 (2006) 3454.
- [119] A. Koukitu, Y. Kumagai, T. Taki, H. Seki, *Jpn. J. Appl. Phys.* 38 (1999) 4980-4982.
- [120] R. Puurunen, *J. Appl. Phys.* 97 (2005) 121301.
- [121] J. Lim, H. Park, S. Kang, *J. Appl. Phys.* 88 (2000) 6327.
- [122] S.-b. Kang, H.-s. Lim, Y.-s. Chae, I.-s. Jeon, G.-h. Choi, US Patent 6287965, 2001
- [123] G. Beyer, A. Satta, J. Schuhmacher, K. Maex, W. Besling, O. Kilpela, H. Sprey, G. Tempel, 64 (2002) 233-245.
- [124] M. L. Green, M. Ho, B. Busch, G. D. Wilk, T. Sorsch, *J. Appl. Phys.* 92 (2002) 7168.
- [125] G. Stringfellow, *Organometallic Vapor-Phase Epitaxy*; Second ed.; Academic Press: London, 1999.
- [126] R. Pantel, G. Auvert, G. Mascarin, *Microelectron. Eng.* 37-8 (1997) 49-57.
- [127] A. Kovacs, C. Esterhuysen, G. Frenking, 11 (2005) 1813-1825.
- [128] D. King, X. Du, A. Cavanagh, A. Weimer, *Nanotechnology* 19 (2008) 445401.
- [129] J. Uhm, H. Jeon, *Jpn. J. Appl. Phys., Part 1* 40 (2001) 4657-4660.
- [130] S. Krukowski, P. Kempisty, P. Strak, *J. Cryst. Growth* 310 (2008) 1391.
- [131] S. Nakamura, Y. Harada, M. Seno, *Appl. Phys. Lett.* 58 (1991) 2021-2023.
- [132] R. C. Powell, N. E. Lee, *Appl. Phys. Lett.* 60 (1992) 2505.
- [133] M. Ritala, M. Leskel, In *Handbook of Thin Film Materials*; Nalwa, H. S., Ed.; Academic Press: San Diego, 2001; Vol. 1, p 2.
- [134] O. H. Kim, D. Kim, T. Anderson, *J. Vac. Sci. Technol. A* 27 (2009) 923-928.
- [135] M. J. Frisch, G. W. Trucks, H. B. Schlegel, G. E. Scuseria, M. A. Robb, J. R. Cheeseman, J. J. A. Montgomery, T. Vreven, K. N. Kudin, J. C. Burant, J. M. Millam, S. S. Iyengar, J. Tomasi, V. Barone, B. Mennucci, M. Cossi, G. Scalmani, N. Rega, G. A. Petersson, H. Nakatsuji, M. Hada, M. Ehara, K. Toyota, R. Fukuda, J. Hasegawa, M. Ishida, T. Nakajima, Y. Honda, O. Kitao, H. Nakai, M. Klene, X. Li, J. E. Knox, H. P. Hratchian, J. B. Cross, V. Bakken, C. Adamo, J. Jaramillo, R. Gomperts, R. E. Stratmann, O. Yazyev, A. J. Austin, R. Cammi, C. Pomelli, J. W. Ochterski, P. Y. Ayala, K. Morokuma, G. A. Voth, P. Salvador, J. J. Dannenberg, V. G. Zakrzewski, S. Dapprich, A. D. Daniels, M. C. Strain, O. Farkas, D. K. Malick, A. D. Rabuck, K. Raghavachari, J. B. Foresman, J. V. Ortiz, Q. Cui, A. G. Baboul, S. Clifford, J. Cioslowski, B. B. Stefanov, G. Liu, A. Liashenko, P. Piskorz, I. Komaromi, R. L. Martin, D. J. Fox, T. Keith, M. A. Al-Laham,

- C. Y. Peng, A. Nanayakkara, M. Challacombe, P. M. W. Gill, B. Johnson, W. Chen, M. W. Wong, C. Gonzalez, J. A. Pople *Gaussian 03, Revision B.04*, (2004)
- [136] A. D. Becke, *J. Chem. Phys.* 98 (1993) 1372-1377.
- [137] P. J. Stephens, F. J. Devlin, C. F. Chabalowski, M. J. Frisch, *J. Phys. Chem.* 98 (1994) 11623-11627.
- [138] A. Heyman, C. B. Musgrave, *J. Phys. Chem. B* 108 (2004) 5718-5725.
- [139] P. Kozodoy, S. Keller, S. P. DenBaars, U. K. Mishra, *J. Cryst. Growth* 195 (1998) 265-269.
- [140] H. Tokunaga, I. Waki, A. Yamaguchi, N. Akutsu, K. Matsumoto, *J. Cryst. Growth* 189-190 (1998) 519-522.
- [141] K. S. Kim, G. M. Yang, H. J. Lee, *Solid State Electron.* 43 (1999) 1807-1812.
- [142] B. Schineller, A. Guttzeit, P. H. Lim, M. Schwampera, K. Heime, O. Schön, M. Heuken, *J. Cryst. Growth* 195 (1998) 274-279.
- [143] A. Usikov, O. Kovalenkov, V. Soukhoveev, V. Ivantsov, A. Syrkin, V. Dmitriev, A. Yu. Nikiforov, S. G. Sundaresan, S. J. Jelialzkov, A. V. Davydov, *Phys. Status Solidi C* 5 (2008) 1829-1831.
- [144] B. Heying, X. H. Wu, S. Keller, Y. Li, D. Kapolnek, B. P. Keller, S. P. DenBaars, J. S. Speck, *Appl. Phys. Lett.* 68 (1996) 643-645.
- [145] C.-R. Lee, J.-Y. Leem, S.-K. Noh, S.-E. Park, J.-I. Lee, C.-S. Kim, S.-J. Son, K.-Y. Leem, *J. Cryst. Growth* 193 (1998) 300-304.
- [146] S. Fischer, C. Wetzel, E. E. Haller, B. K. Meyer, *Appl. Phys. Lett.* 67 (1995) 1298-1300.
- [147] S. J. Pearton, J. W. Lee, C. Yuan, *Appl. Phys. Lett.* 68 (1996) 2690-2692.
- [148] D. J. Chadi, *Appl. Phys. Lett.* 71 (1997) 2970-2971.
- [149] I. Rogozin, A. Georgobiani, M. Kotlyarevsky, *Inorg. Mater.* 44 (2008) 1208-1213.
- [150] S. Limpijumnong, C. G. Van de Walle, *Phys. Rev. B* 69 (2004) 035207.
- [151] J. W. Allen, *Semicon. Sci. Technol.* 10 (1995) 1049-1064.
- [152] U. Kaufmann, M. Kunzer, M. Maier, H. Obloh, A. Ramakrishnan, B. Santic, P. Schlotter, *Appl. Phys. Lett.* 72 (1998) 1326-1328.
- [153] Y. Qi, C. Musante, K. Lau, L. Smith, R. Odedra, R. Kanjolia, *J. Electron. Mater.* 30 (2001) 1382-1386.

- [154] E. Kolawa, P. J. Pokela, J. S. Reid, J. S. Chen, M. A. Nicolet, *Appl. Surf. Sci.* 53 (1991) 373-376.
- [155] A. A. Istratov, C. Flink, H. Hieslmair, E. R. Weber, T. Heiser, 81 (1998) 1243-1246.
- [156] M. Wittmer, *Appl. Phys. Lett.* 36 (1980) 456-458.
- [157] T. Suntola, 216 (1992) 84-89.
- [158] A. Ibidunni, R. Masaitis, R. Opila, A. Davenport, H. Isaacs, J. Taylor, *Surf. Interface Anal.* 20 (1993) 559.
- [159] D. J. Kim, Y. B. Jung, M. B. Lee, Y. H. Lee, J. H. Lee, J. H. Lee, *Thin Solid Films* 372 (2000) 276.
- [160] K. C. Park, K. B. Kim, *J. Electrochem. Soc.* 142 (1995) 3109.
- [161] J. H. Koo, J. W. Lee, T. H. Doh, Y. D. Kim, Y. D. Kim, H. T. Jeon, *J. Vac. Sci. Technol. A* 19 (2001) 2831.
- [162] H. Kim, C. Lavoie, M. Copel, V. Narayanan, D.-G. Park, S. M. Rossnagel, *J. Appl. Phys.* 95 (2004) 5848.
- [163] T. Oku, E. Kawakami, M. Uekubo, K. Takahiro, S. Yamaguchi, M. Murakami, *Appl. Surf. Sci.* 99 (1996) 265-272.
- [164] K. H. Min, K. C. Chun, K. B. Kim, *J. Vac. Sci. Technol. B* 14 (1996) 3263-3269.
- [165] K.-C. Kim, in Department of Chemical Engineering, University of Florida, Gainesville, FL, 2006.

BIOGRAPHICAL SKETCH

Oh Hyun Kim was born in Daejon, South Korea in 1978. He is son of Ukdong Kim and Kyoungja Ko, and brother of Ansoon Kim and Sookheun Kim. He received Bachelor of Science degree from Seoul National University, South Korea in 2004. During his undergraduate program, he completed military service in U.S. Army as aircraft fuel specialist between 1999 and 2001. In 2004, he joined the PhD program in Chemical Engineering Department at University of Florida. Upon graduation, he plans to work for Intel Corporation in Portland, Oregon as a senior process engineer; his main role is to develop the next generation epitaxial process for strained silicon/germanium.